Mechanical Engineering Advances 2025, 3(2), 2838.
https://doi.org/10.59400/mea2838

Article

Innovative semi-analytical approaches to micropolar MHD fluid flow between stretching disks under radiant heat flux

Ali Ahmadi Azar

Department of Mechanical Engineering, NT.C., Islamic Azad University, Tehran, Iran; aliahmadiazar.mech@gmail.com, a.ahmadi.azar@iau-tnb.ac.ir

CITATION

Ahmadi Azar A. Innovative semi-analytical approaches to micropolar MHD fluid flow between stretching disks under radiant heat flux. Mechanical Engineering Advances. 2025; 3(2): 2838. https://doi.org/10.59400/mea2838

ARTICLE INFO

Received: 24 February 2025
Accepted: 11 April 2025
Available online: 26 June 2025

Abstract: This study investigates the viscous, incompressible, laminar, time-independent micropolar MHD fluid flow between two stretching disks under radiant heat flux, with applications in industrial systems like turbines and nuclear reactors. Using suitable similarity transformations, the nonlinear constitutive equations are reduced to coupled ODEs and solved through two novel semi-analytical approaches: the Hybrid Analytical-Numerical method (HAN method), which constructs analytical solutions from numerical data, and the modified Akbari-Ganji Method (modified AGM) that operates independently of numerical solutions. Results demonstrate that stretching Reynolds number, magnetic parameter, and three micropolar parameters significantly affect all five dimensionless quantities (axial/radial velocity, microrotation, temperature, and concentration), while Eckert number variations cause a 16.5% maximum temperature increase when doubled from 1 to 2. A 429% temperature surge occurs as the Prandtl number rises from 3 to 22, whereas the Schmidt number (0.1–1.5) only modifies the concentration profile shape without changing extrema. The radiation parameter (0–8) alters temperature distribution between disks without affecting maxima/minima. Three validation methods confirm solution accuracy: graphical verification, comparison with existing analytical results, and cross-method consistency between HAN and modified AGM outputs. The study's innovative dual-method approach coupled with 3D contour visualizations provides unprecedented semi-analytical solutions for this classical problem, offering both theoretical advancement and practical industrial insights.

Keywords: MHD flow; semi-analytical methods; stretchable disks; modified AGM; HAN-method

1. Introduction

Integrating heat and mass transfer with fluid flow analysis is essential in many engineering and scientific processes, prompting extensive research into stretching disk models. Magnetohydrodynamics (MHD) is a practical fluid model for understanding the flow of electrically conductive fluids in magnetic fields [1]. It is fundamental in physics, particularly in studying low-frequency, large-scale magnetic behavior in plasma and liquid metals, with applications in geophysics, astrophysics, and engineering. Non-Newtonian fluids, such as micropolar fluids that include two velocity variables not found in the Navier-Stokes equations, are also widely researched for their industrial applications [2]. While mathematical models can describe natural phenomena, their nonlinear equations lack exact analytical solutions, necessitating numerical and semi-analytical methods for approximate solutions. This study is significant mathematically as it introduces two new methods for the semi-analytical solution of nonlinear ODEs, demonstrating their application. Eringen's micropolar fluid theory, proposed and later refined in the 1960s, has been extensively studied [3–

6]. Turkyilmazoglu investigated the time-independent, incompressible, and viscous fluid flow due to the rotation of a permeable disk with uniform suction/injection capability [7–9]. Other researchers, including Sahoo, Srivastava, and Iqbal, have examined the fluid dynamics and heat transfer in non-Newtonian and MHD fluids in various configurations, often using similarity transformations to convert the constitutive equations into ordinary differential equations (ODEs) for numerical or analytical solutions [10–18]. This body of work highlights the complicated nature of fluid dynamics and the ongoing efforts to develop robust mathematical models for practical applications. Tabassum and Mustafa [19] explored the flow of non-Newtonian Reiner-Rivlin fluid caused by the rotation of an impermeable swirling disk. They simplified the governing PDEs and analyzed them numerically. Yao and Lian [20] studied the Von Kármán rotational flow problem arising from the rotation of an infinitely large disc, converting the constitutive equations into a set of ODEs using similarity transformations. Sahoo and Shevchuk [21] examined the flow and heat transfer in a rotating non-Newtonian Reiner-Rivlin fluid caused by a constantly stretching disk. Yao and Lian [22] also investigated Von Kármán rotational viscous flow due to disk rotation in a porous medium, solving the equations using the HAM method after converting them to ODEs and validating their results against similar studies. Zangooee et al. [23] focused on heat and mass transfer in nanofluid MHD flow due to the stretching and rotation of two disks, using AGM to solve the simplified equations. Das and Sarkar [24] analyzed non-Newtonian Reiner-Rivlin fluid flow between two swirling stretchable circular sheets and solved the equations analytically after converting them to ODEs. Naqvi et al. [25] investigated time-independent, incompressible nanofluid flow due to the rotation of an impermeable disk at a constant angular velocity. Usman et al. [26] studied heat transfer and fluid dynamics of a wavy surface plate with temperature variations, rotating in a uniform flow. Various similar analytical studies have been conducted [27–37]. Khan [38] examined a two-dimensional MHD problem through a porous channel, simplifying the governing PDEs with similarity variables and solving them analytically. Ahmad et al. [39] investigated polymer fluid effects on a stretchable disk in a magnetic field using the FENEP model. Khan et al. [40] studied non-Newtonian micropolar fluid flow, simplifying the equations with dimensionless variables and analyzing them numerically. Khan [41] examined linear viscoelastic fluid flow on a shrinking/stretching plane, simplifying the PDEs with dimensionless variables and analyzing them using HPM. Anusha et al. [42] analyzed heat and mass transfer in a time-independent, slow, viscoelastic 2D flow caused by a porous widening/shrinking slip, simplifying the PDEs and analyzing them analytically. Ghadikolaei et al. [43] studied 3D nanofluid flow through a swirling channel with thermal radiation, simplifying the PDEs and solving them numerically. Ghasemi et al. [44] examined non-Newtonian MHD third-grade blood flow in porous arteries, simplifying the equations and analyzing them using both analytical and numerical methods. Fakour et al. [45] investigated non-turbulent micropolar fluid flow in a 2D permeable channel, converting the equations into ODEs using similarity transformations and solving them analytically and numerically. Rashad et al. [46] studied the magnetohydrodynamic (MHD) flow and heat transfer of a Casson-Carreau hybrid nanofluid (Al_2O_3-Cu/water) in a Darcy-Forchheimer porous medium under thermal radiation, magnetic field, heat

sink/source, and slip conditions. Using non-similar transformations, they converted the governing equations into a solvable form and obtained numerical solutions. Their results showed that thermal radiation and blowing/suction parameters enhanced heat transfer, while the skin friction coefficient responded similarly to radiation but oppositely to suction/injection effects. In another study, Rashad et al. [47] investigated the flow of a Jeffrey hybrid nanofluid over a moving porous surface under the influence of a magnetic field, heat sink/source, yield stress, and chemical reaction. Using similarity transformations, they converted the governing partial differential equations into nonlinear ordinary differential equations, which were then solved numerically using the RKF45 method with shooting technique. Their analysis focused on key physical parameters affecting heat flux, temperature distribution, flow velocity, and surface friction. The results demonstrated that increased permeability, yield stress, heat generation, and magnetic field strength enhanced temperature distribution while reducing heat transfer efficiency. Conversely, chemical reaction and heat source parameters improved mass transport. This study provides valuable insights for thermal engineering applications. Abdelhafez et al. [48] investigated the enhancement of convective heat transfer in industrial applications using magnetohydrodynamic Maxwell nanofluid flow through a porous medium over a convectively heated stretching cylinder. The study incorporated higher-order chemical reactions and employed the optimal homotopy analysis method to solve the governing ordinary differential equations. Through graphical analysis, the authors examined the effects of key parameters on velocity, temperature, and concentration profiles. Their results demonstrated that heat transfer rates improved with increasing Biot number and chemical reaction order, while higher values of reaction parameter, magnetic field strength, permeability, and Eckert number reduced heat transfer efficiency. Mass transfer increased with Joule heating, chemical reaction rate, and Biot number but decreased with stronger magnetic fields, greater permeability, and higher-order chemical reactions. The findings were validated against previous studies and provide valuable insights for applications involving fluid transport in cylindrical tanks, particularly in water, oil, and gas systems. Turkyilmazoglu [49] conducted a two-fold study to (1) compare the behavior of a stretching jet under quadratic air resistance with classical frictionless jet formation, and (2) validate similarity flows for stretching thin bodies under boundary layer approximations. The research extended electrohydrodynamic jet theory—typically applied to electrospinning and jet printing—by incorporating air resistance effects in both the cone and final regimes before substrate deposition. Analysis of the nonlinear governing equations revealed that near the nozzle, viscous and electrical forces rapidly thin the jet, with air resistance enhancing this effect and improving alignment with experimental observations. The jet exhibited exponential thinning, accelerated by inversely quadratic liquid particle speeds, confirming similarity flow over exponentially stretching sheets. In the final regime, frictionless jets decayed algebraically, while air resistance caused exponential decay to a limiting speed—yielding square-root-dependent similarity flow for free jets and Sakiadis-type flow for resisted cases. The study uniquely integrated electrostatic forces (Coulombic effects) with quadratic drag, supported by experimental glycerol jet data. Numerical simulations further validated the asymptotic jet behavior under combined electrostatic pull and electric currents from bulk/surface charge transport,

offering insights beyond conventional jet hydrodynamics. In another study, Turkyilmazoglu [50] investigated unsteady heat and fluid flow phenomena over stretching/shrinking surfaces through rigorous mathematical modeling. The study developed two distinct approaches: (1) a conventional model yielding trivial steady-state solutions, and (2) a novel formulation that successfully captured physically meaningful steady-state solutions documented in existing literature. Key contributions include deriving new similarity solutions for temperature fields in the conventional model and establishing that uniform wall temperature conditions optimize heat transfer rates. While the proposed model permits similarity solutions for specific cases, they noted that general conditions may require non-similar solution approaches. The analysis provides valuable insights for stagnation-point flows and non-Newtonian viscoelastic fluids, while identifying important directions for future research in this domain. Enamul and Ontela [51] investigated heat transfer and entropy generation in a hybrid nanofluid flow between rotating porous disks, focusing on applications like cooling systems and energy storage. They analyzed a $TiO_2/CoFe_2O_4$-engine oil nanofluid, incorporating Hall currents, viscous dissipation, and convective effects. Using similarity transformations and homotopy analysis, they solved the governing equations and found that temperature profiles improved with higher Brinkman numbers and Biot numbers, while skin friction decreased with increased TiO_2 concentration, porosity, and magnetic fields. Their results demonstrated enhanced heat transfer rates with larger nanoparticle shape factors and magnetic parameters, providing valuable insights for optimizing thermal management in MHD systems and nanofluid-cooled devices. Hussain et al. [52] developed a novel numerical model to analyze heat, mass, and microorganism transfer in nanofluid flow over a rotating stretched disk. They combined bioconvection of motile microorganisms with thermal transport equations to enhance system efficiency in cooling applications. The researchers incorporated internal heat generation and nanoparticle diffusion effects into modified momentum equations and solved them using shooting method with Runge-Kutta technique. Their analysis revealed that increasing unsteadiness (S) accelerated thermal energy dissipation, while bioconvection significantly altered velocity and temperature profiles by thinning microorganism layers. The study demonstrated how these mechanisms could optimize thermal management in aerospace systems experiencing extreme frictional heating. Key achievements included establishing the first bioconvection-nanofluid model for rotating disks and quantifying microorganism-enhanced heat transfer efficiency for practical engineering applications. Lone et al. [53] investigated MHD Casson hybrid nanofluid flow between two rotating stretchable circular plates with variable porous spacing, employing the Cattaneo-Christov heat flux model to analyze thermal performance. They computationally solved the governing equations using the bvp4c method, examining magnetic field, thermal radiation, and non-uniform heat source/sink effects. Their results showed that axial velocity decreased near the lower disk ($0 \leq \xi < 0.4$) but increased near the upper disk ($0.4 < \xi \leq 1.0$) with higher magnetic factors, while radial velocity exhibited interval-specific variations. They demonstrated that increased porous spacing enhanced axial/tangential velocities and that thermal distribution improved with radial/magnetic factors and Biot number but declined with thermal relaxation time. The study provided validated insights for optimizing heat

transfer in rotating plate systems through comparative analysis. Mandal et al. [54] examined entropy generation in MHD hybrid nanofluid (Ag-MgO) flow over a permeable rotating disk with variable fluid properties, incorporating time-dependent stretching, velocity/temperature slip effects, and nonlinear thermal radiation. They transformed the governing equations using similarity variables and solved them numerically via shooting technique with 4th-order Runge-Kutta-Fehlberg method. The team discovered that disk rotation accelerated fluid motion while magnetic fields, thermal radiation, and temperature-dependent viscosity significantly influenced heat transfer rates, skin friction, and entropy production (quantified by Bejan number). Their analysis revealed optimal parameter combinations for minimizing entropy generation and enhancing system efficiency. Key achievements included: (1) developing a comprehensive model for entropy-optimized nanofluid flows, (2) quantifying rotational and magnetic effects on thermal performance, and (3) providing design insights for energy-efficient thermal systems in sustainable engineering applications. Naveed Khan et al. [55] studied the boundary layer flow of a hybrid Ag-MgO/water nanofluid containing gyrotactic microorganisms over a rotating porous disk, incorporating double diffusion theory, Joule heating, and chemical reactions. They modeled multiple slip boundary conditions and transformed the governing equations into nonlinear ODEs using similarity transformations, which were solved numerically via the BVP4C MATLAB solver. Their results demonstrated that increasing nanoparticle volume fraction enhanced both velocity and temperature fields, while higher porosity parameters and inertia coefficients reduced velocity distribution. The team validated their findings through comparative analysis with previous studies. Key achievements included: (1) developing a comprehensive bio-nanofluid model with slip effects, (2) quantifying how nanoparticle concentration and porous media interactively affect flow dynamics, and (3) providing optimized parameters for microbial-enhanced thermal systems in rotating machinery applications. Rauf et al. [56] investigated the steady-state flow of a viscous fluid over a variable-thickness rotating disk with stretching effects, incorporating a horizontal magnetic field to regulate flow dynamics and thermal energy in high-temperature applications. They analyzed thermal radiation and melting heat transfer, employing similarity transformations to convert governing equations into dimensionless form, which were solved numerically using the RKF-45 method. Their results demonstrated that melting reduced fluid resistance near the surface, increasing flow velocity while decreasing temperature gradients due to latent heat absorption. The study revealed that the horizontal magnetic field stabilized radial flow at angles (α_1) between 0-30°, and the dimensionless radius enhanced thermal transport from the disk surface. Key achievements included: (1) developing a magnetohydrodynamic model for variable-thickness rotating surfaces, (2) quantifying how melting and magnetic fields synergistically affect flow/thermal profiles, and (3) providing design insights for thermal management in turbines and phase-change material systems. Senbagaraja and De [57] analyzed the three-dimensional electro-osmotic flow of EMHD tangent hyperbolic nanofluid over a stretching rotating porous disk, incorporating thermal radiation, variable thermal conductivity, chemical reactions, and Stefan blowing effects. They transformed the governing partial differential equations into ordinary differential equations using similarity variables and solved them numerically via fifth-

order Runge-Kutta-Fehlberg with shooting method. Through response surface methodology, they identified an optimal heat transfer rate of 6.46 for high magnetic/thermal radiation parameters with low electric field, while sensitivity analysis showed thermal radiation had 91.44% relative sensitivity at medium levels. Their study uniquely addressed previously unexplored assumptions with advanced boundary conditions. Key achievements included: (1) developing the first comprehensive EMHD nanofluid model with Stefan blowing, (2) optimizing heat transfer parameters through statistical analysis, and (3) demonstrating applications in biomedical, industrial, and microfluidic systems like drug delivery and electronics cooling. Sultana et al. [58] investigated the magnetohydrodynamic (MHD) forced convective flow of copper-, alumina-, and titania-based nanofluids induced by eccentric rotations of an unsteady stretching porous disk and surrounding fluid. They considered incompressible, viscous, electrically conductive fluid with Joule heating and viscous dissipation effects. The team obtained exact solutions for velocity fields and numerical solutions for temperature profiles using the Crank-Nicolson method. Their analysis revealed that increasing nanoparticle volume fraction reduced velocity while thickening the boundary layer, and higher unsteady parameters enhanced velocity but weakened temperature profiles. Key achievements included: (1) developing exact/numerical solutions for eccentric rotating nanofluid systems, (2) quantifying how porosity (S), magnetic (M^2), and unsteady parameters (C) govern flow-thermal behavior, and (3) demonstrating suction's cooling effect for thermal management in rotating machinery applications. Turkyilmazoglu and Pop [59] examined the flow and heat transfer characteristics of a Bingham viscoplastic fluid subjected to combined axial rotation and radial stretching of a circular disk. They extended existing Bingham fluid models using von Kármán similarity transformations, solving the resulting nonlinear ODE system to analyze momentum and thermal fields. The study identified three key dimensionless parameters (swirling number, Bingham number, modified Reynolds number) governing the flow, revealing that radial stretching required significantly higher yield stresses than rotation alone to exhibit non-Newtonian effects. At high Bingham numbers, they observed a two-layer structure with an unyielded plug region and yielded shear layer near the wall. Key achievements included: (1) developing the first comprehensive model for Bingham fluids under combined stretching-rotation, (2) quantifying how wall movement enhances non-Newtonian behavior, and (3) characterizing the von Kármán pump mechanism in viscoplastic flows with practical implications for industrial processing systems. Usman et al. [60] investigated the flow and heat transfer characteristics of a ternary hybrid nanofluid (THNF) containing Cu, Al_2O_3, and MWCNTs over a rotating stretching disk under magnetic field effects. They transformed the governing equations into nonlinear ODEs and solved them numerically using MAPLE 2022, analyzing dimensionless velocity, temperature, concentration profiles, and performance metrics. Their results demonstrated that THNFs outperformed single and binary nanofluids, achieving a 10–15% enhancement in Nusselt number and an 8–12% reduction in skin friction under moderate magnetic fields. The study revealed that transitioning from pseudoplastic to dilatant behavior decreased tangential/radial velocities and surface temperature. Key achievements included: (1) developing the first THNF model for rotating stretching disks, (2) quantifying synergistic nanoparticle effects on thermal

performance, and (3) proving THNF superiority for applications like electronics cooling and lubrication systems. Zada et al. [61] explored entropy generation and heat transfer in an unsteady flow of variable magnetic hybrid nanofluid (SWCNT/MWCNT in water-ethylene glycol) between parallel rotating disks. They developed innovative hybrid nanofluid models and employed the Buongiorno two-phase approach to analyze Brownian motion and thermophoresis effects. The team solved the governing equations using both Homotopy Analysis Method (HAM) and bvp4c numerical techniques, achieving novel results never before compared with other methods. Their analysis revealed how disk rotation and nanoparticle characteristics influenced temperature/concentration distributions in the heat transfer system. Key achievements included: (1) creating the first comprehensive model for magnetic hybrid nanofluids in rotating disk systems, (2) quantifying entropy generation mechanisms in SWCNT/MWCNT suspensions, and (3) establishing benchmark data for thermal optimization in glycol-based nanofluid applications. Ahmadi Azar [62] conducted a rigorous investigation of Von Kármán's viscous swirling flow problem generated by a rotating disk, employing an innovative Hybrid Analytical and Numerical method (HAN method) methodology. The research addressed this classical nonlinear problem through a novel semi-analytical approach that synergistically combines numerical computation with analytical formulation. The HAN method demonstrated exceptional capability in solving complex nonlinear differential equations by utilizing numerical solutions to determine unknown coefficients in analytical polynomial expressions, thereby overcoming the limitations of traditional boundary condition constraints. The study achieved breakthrough precision in quantifying critical hydrodynamic parameters, including boundary layer characteristics, wall shear stress distributions, torque requirements, and mechanical power consumption. Key scientific contributions encompass: (1) development of a robust computational-analytical framework for nonlinear fluid dynamics problems, (2) establishment of new benchmark solutions for rotating disk flows with unprecedented accuracy, and (3) demonstration of advanced mathematical techniques to extract novel physical insights from fundamental fluid mechanics systems. This work significantly advances both theoretical and applied aspects of rotating flow analysis while providing a transformative methodology for complex nonlinear problems in continuum mechanics.

Due to the inherent complexity of natural phenomena, which frequently lack exact analytical solutions because of nonlinearities, numerical and semi-analytical approaches play a pivotal role. The Hybrid Analytical and Numerical Method (HAN method), bridges analytical and numerical techniques by deriving analytical expressions from numerical solutions, offering greater flexibility than traditional semi-analytical methods. This approach was first applied to model heat and mass transfer in a viscous, incompressible, laminar axisymmetric flow of a micropolar fluid subjected to a magnetic field between two stretchable disks. To further validate the HAN method's reliability, the article cites subsequent studies [63–66] where it has been successfully utilized to solve analogous governing equations. In a recent application [63], the HAN method was employed as a semi-analytical tool to examine the steady forced motion of a non-Newtonian MHD Reiner-Rivlin viscoelastic fluid confined between two plates under a magnetic field. The governing partial differential equations (PDEs) were converted into ordinary differential equations (ODEs) via Von

Kármán similarity transformations, which the HAN method then solved analytically alongside their boundary conditions. The results were cross-verified against solutions from the Homotopy Perturbation Method (HPM) and the numerical Runge-Kutta approach, with additional quantitative insights derived from the HAN solutions. Another investigation [64] explored the steady, laminar, incompressible, two-dimensional flow of a micropolar fluid between two disks—one porous and the other non-porous—neglecting body forces and couples. Using Von-Kármán similarity variables, the governing PDEs were reduced to ODEs, which were then solved semi-analytically via the Modified Akbari-Ganji Method (Modified AGM) and the HAN method, marking a novel application of these techniques. The study analyzed the influence of slip coefficients, Reynolds numbers, and micropolar parameters (e.g., vortex viscosity, spin gradient viscosity, and microinertia density) on velocity and microrotation profiles. The solutions were validated against existing literature, with both methods yielding nearly identical results, reinforcing their accuracy. Further research [65] applied the HAN method to nonlinear coupled ODEs to assess how structural variations—such as stretching rate and disk spacing—affected key physical parameters. Findings indicated that higher stretching rates increased temperature and Nusselt number, while greater disk separation reduced microrotation and wall couple stress. By redefining parameters like the magnetic field strength, Eckert number, stretching Reynolds number, and micropolar coefficients, the study quantified their impact, with results corroborated by prior research. In another study [66], the HAN method provided exact solutions for Von Kármán swirling flow induced by a rotating disk with uniform suction. Three scenarios were examined: opposing and aligned swirling flow at infinity, suction without swirling, and combined swirling and suction. Key observations included a peak skin friction coefficient when the fluid's angular velocity at infinity decreased relative to the disk's rotation, while increased fluid rotation reduced it. Higher suction enhanced the skin friction coefficient, particularly on porous disks, and in the absence of both swirling and suction, pressure distribution depended solely on axial distance. These results underscored the HAN method's efficacy in resolving intricate fluid dynamics problems. Beyond swirling flow analyses [67–72], the HAN method's applicability extends to a broader range of fluid mechanics challenges, demonstrating its versatility and robustness. The modified Akbari-Ganji method (AGM) is also valuable for solving nonlinear differential equations. Using these two methods, it is possible to obtain analytical solutions for nonlinear problems where exact solutions are challenging. Approximate analytical solutions of nonlinear differential equations can be effective. Numerous studies [73–78] have employed various methods to solve differential equations, examine parameter effects on dimensionless variables, and present results through graphs and 3D contours.

This article investigates heat and mass transfer in a viscous, incompressible, axially symmetric, and time-independent micropolar fluid confined between two stretchable disks, assuming a negligible magnetic Reynolds number and no polarization voltage. By employing similarity transformations, the governing partial differential equations (PDEs) are converted into a set of nonlinear ordinary differential equations (ODEs). Two innovative semi-analytical methods, the Hybrid Analytical and Numerical (HAN) method and the modified Akbari-Ganji method (modified

AGM), are utilized to solve these equations. The HAN method is a flexible approach that integrates numerical solutions to construct analytical methods, making it highly adaptable as it is not limited to specific numerical techniques, while the modified AGM operates independently of numerical solutions, proving useful when numerical solutions are unavailable or when validating the HAN method. Both methods, first introduced by A. Ahmadi Azar, have demonstrated significant success in addressing nonlinear differential equations, adding innovation and novelty to this study. Moreover, similarity solutions, where PDEs are transformed into ODEs using similarity variables such as von Karman transformations, simplify the complexity of three-dimensional and time-independent fluid flow and heat transfer equations, making them easier to solve. The study addresses key questions that motivated this research, such as (1) how to achieve analytical solutions using numerical solutions without semi-analytical methods (answered by the HAN method explained in Sections 3.1 and 3.2); (2) how to construct analytical solutions independent of numerical solutions (addressed by the modified AGM discussed in Sections 3.3 and 3.4); (3) how to simplify complicated three-dimensional equations governing fluid flow and heat transfer (accomplished using von Karman similarity variables detailed in Section 2); and (4) whether the methods are applicable to specific parameter ranges or limited to particular cases (confirmed through diagrams shown in Section 3.5 and elaborated on in Section 4). These aspects, combined with the study's exploration of key parameters such as radiation, magnetic field, Eckert number, Reynolds number, Schmidt number, and Prandtl number on micro-rotation profiles, velocity, concentration, and temperature profiles, highlight the significance of this research and its differentiation from other similarity solution studies.

2. Governing equations

This article investigates the nonlinear problem of heat and mass transfer of a viscous, time-independent, non-compressible, and axisymmetric micropolar fluid flow among stretchy disks. As demonstrated in **Figure 1**, the disks are placed in $z = l$ and $z = -l$ (l is a positive real number: $l \in \mathbb{R}^+ = [0, +\infty)$) in a circular cylindrical coordinate system (r, θ, z), where $0 \leq r < \infty$, $0 \leq r \leq 2\pi$, $-\infty \leq z < +\infty$. The model examines an electrically conductive micropolar fluid, with a crosswise magnetic field applied at a right angle to the boundaries. The governing equations (GEs) in this work are represented using the cylindrical coordinate system. The magnetic Reynolds number was considered to be insignificant, according to McChesney [79]. Consequently, it was demonstrated that the difference between the imposed and induced magnetic fields is negligible. Furthermore, the fact that no polarization voltage is applied should be taken into account. The following vectorial forms of the continuity, momentum, and microrotation are as follows [4]:

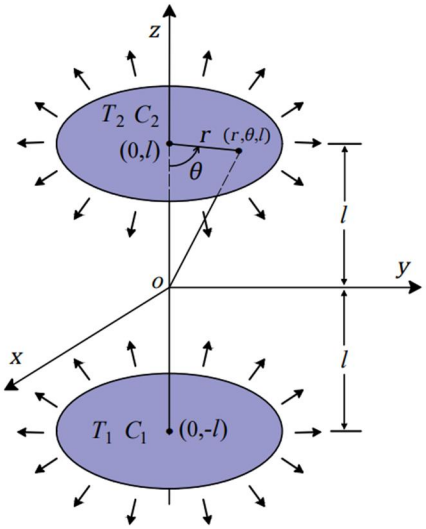

Figure 1. Geometry of the problem.

Continuity equation:

$$\boldsymbol{\nabla}(\mathbf{V}) = \mathbf{0}\,. \tag{1}$$

Momentum equation:

$$(\mu + \kappa)\nabla^2\mathbf{V} + \kappa\boldsymbol{\nabla} \times \mathbf{N} - \boldsymbol{\nabla}p + \mathbf{J} \times \mathbf{B} = \rho\dot{\mathbf{V}}\,. \tag{2}$$

Microrotation equation:

$$(\alpha_1 + \alpha_2 + \alpha_3)\boldsymbol{\nabla}(\boldsymbol{\nabla}\mathbf{N}) - \alpha_3(\boldsymbol{\nabla} \times \boldsymbol{\nabla} \times \mathbf{N}) + \kappa\boldsymbol{\nabla} \times \mathbf{V} - 2\kappa\mathbf{N} = \rho j\dot{\mathbf{N}}\,. \tag{3}$$

The fluid velocity vector is denoted by $\mathbf{V}$, the fluid dynamic viscosity is denoted by μ, the fluid microrotation is denoted by $\mathbf{N}$, the fluid vortex viscosity is denoted by κ, the fluid pressure distribution is denoted by p, the fluid density is denoted by ρ, the density vector of the fluid is denoted by $\mathbf{J}$, the micro inertia per unit mass is denoted by j, the sum of induced and imposed magnetic field is denoted by $\mathbf{B}$, and the gyro-viscosity coefficients are denoted by α_1, α_2, and α_3, respectively. In Equations (1)–(3), $\boldsymbol{\nabla}$ is the gradient operator, $\boldsymbol{\nabla}\times$ is the curl operator and $\dot{} = \mathrm{d}/\mathrm{d}t$ is the operator of the total derivative with respect to the time t.

According to the studies of Agarwal [1] and Jalili et al. [2], the equations of density, energy, and concentration are represented in vector form and for a general state as follows:

Density equation:

$$\mathbf{J} = \sigma_{el}(\mathbf{V} \times \mathbf{B})\,. \tag{4}$$

Energy equation:

$$\rho c_{\mathrm{p}}\frac{\mathrm{D}T}{\mathrm{D}t} = k\nabla^2 T + q_{\mathrm{rh}} + \mu\Phi\,. \tag{5}$$

Concentration equation:

$$\frac{\mathrm{D}C}{\mathrm{D}t} = D_{\mathrm{e}}\nabla^2(C) + \dot{m}'''\,. \tag{6}$$

The electrical conductivity of the fluid is denoted by σ_{el}, the viscous dissipation

function is denoted by Φ, the fluid temperature distribution is denoted by T, the fluid specific heat capacity at constant pressure is denoted by c_{p}, the fluid thermal conductivity is denoted by k, the radiant heat flux is denoted by q_{rh}, the concentration of the fluid is denoted by C, the diffusion coefficient of the fluid is denoted by D_{e}, the operator of the total derivative with respect to the time is denoted by $\mathrm{D}/\mathrm{D}t := \mathrm{d}/\mathrm{d}t$ and $\dot{m}'''$ is related to reactive flows. In addition, Agarwal [1] and Jalili et al. [2] considered the relationship between α_1, α_2, α_3, μ, and κ parameters in Equation (7) as follows:

$$2\mu + \kappa \geq 0, \quad \kappa \geq 0, \quad 3\alpha_1 + \alpha_2 + \alpha_3 \geq 0, \quad \alpha_3 \geq |\alpha_2|\,. \tag{7}$$

According to Agarwal [1] and Jalili et al. [2], the velocity and microrotation vector fields in the component's forms are assumed in Equation (8) as follows:

$$\mathbf{V} = u\hat{\mathbf{e}}_1 + w\hat{\mathbf{e}}_3, \quad \mathbf{N} = N_2\hat{\mathbf{e}}_2\,, \tag{8}$$

where the components u, w and N_2 are functions of the variables r, z of the circular cylindrical coordinate system (r, θ, z) and $\hat{\mathbf{e}}_1$, $\hat{\mathbf{e}}_2$, $\hat{\mathbf{e}}_3$ are respectively the unit vectors along the r, θ, z axes.

According to Devi and Devi [80], the radioactive heat flux q_{rh} is show in Equation (5) like this:

$$q_{\mathrm{rh}} = -\frac{4\sigma}{3k_a}\frac{\partial(T^4)}{\partial z}, \tag{9}$$

where the constant of Stefan-Boltzmann is denoted by σ, and also the average absorption coefficient is denoted by k_a. The following are the boundary conditions associated with the physical principles underlying the problem as described in Equations (1)–(6) [1,2]:

$$\begin{cases} u = rS, \ \ w = 0, \ \ N_2 = 0, \ \ T = T_1, \ \ C = C_1, \ \ \text{when } z = -l, \\ u = rS, \ \ w = 0, \ \ N_2 = 0, \ \ T = T_2, \ \ C = C_2, \ \ \text{when } z = l\,. \end{cases} \tag{10}$$

The parameter related to the stretching of the two disks is denoted by S, the temperature of the lower disk is shown by T_1 and the temperature of the top disk is denoted by T_2. The concentration of the lower disk is denoted via C_1 and the top disk is denoted by the C_2. The Equations (1)–(6) will be reduced into a simpler form by the following dimensionless variable [1,2]:

$$\begin{gathered} u = -\frac{rS}{2}f'(\xi), \quad w = Slf(\xi), \quad N_2 = -\frac{rS}{2l^2}g(\xi), \\ \theta(\xi) = \frac{T - T_2}{T_1 - T_2}, \quad \phi(\xi) = \frac{C - C_2}{C_1 - C_2}, \quad \xi = \frac{z}{l}. \end{gathered} \tag{11}$$

where $\theta(\xi)$ is the dimensionless temperature of the fluid, $\phi(\xi)$ is the dimensionless concentration of the fluid, $f(\xi)$ is the dimensionless axial velocity of the fluid, $f'(\xi)$ is the dimensionless radial velocity of the fluid, $g(\xi)$ is the dimensionless microrotation distribution of the fluid. By applying the dimensionless variables given in Equation (11), the partial differential equations listed in Equations (1)–(6) can be transformed into the following system of nonlinear ordinary differential equations [1,2]:

$$F \coloneqq (1+\lambda_1)f^{(4)} - \lambda_1 g'' - R_0 f f''' - R_0 M_n^2 f'' = 0\,, \tag{12}$$

$$G \coloneqq \lambda_3 g'' + \lambda_1(f'' - 2g) + R_0\lambda_2\left(\frac{1}{2}f'\mathrm{g} - fg'\right) = 0\,, \tag{13}$$

$$\Theta \coloneqq \left(1+\frac{4}{3}N_r\right)\theta'' + \frac{1}{4}P_r E_c (f'')^2 - R_0 P_r f\theta' = 0\,, \tag{14}$$

$$\Phi \coloneqq \phi'' + R_0 S_c f\phi' = 0\,. \tag{15}$$

The dimensionless stretching Reynolds number is denoted by $R_0 = \rho S l^2/\mu$, the dimensionless parameter of magnetic field is denoted by $M_\mathrm{n} \coloneqq (\sigma_\mathrm{el} B_\mathrm{os}^2/\rho S)^{1/2}$, the dimensionless parameter of vortex viscosity is denoted by $\lambda_1 = \kappa/\mu$, the dimensionless parameter of micro-inertial density is denoted by $\lambda_2 = j/l^2$, the dimensionless parameter of spin gradient viscosity is denoted by $\lambda_3 = \alpha_3/\mu l^2$, the dimensionless Prandtl number is denoted by $P_\mathrm{r} = \mu c_\mathrm{p}/k$, the dimensionless parameter of radiation is denoted by $N_\mathrm{r} = 4\sigma T_2^3/k_\mathrm{a} k$, the dimensionless Eckert number is denoted by $E_\mathrm{c} = r^2 S^2/(T_1 - T_2)c_\mathrm{p}$, the dimensionless Schmidt number is denoted by $Sc = \nu/D_\mathrm{e}$, and the strength of the magnetic field is denoted by B_os.

The dimensionless variables presented in Equation (11) also modify the boundary conditions described in Equation (10), transforming them into the simpler form shown below [1,2]:

$$\begin{cases} f(-1) = 0,\ \ f'(-1) = -2,\ \ g(-1) = 0,\ \ \theta(-1) = 1,\ \ \phi(-1) = 1, \\ f(1) = 0,\ \ f'(1) = -2,\ \ g(1) = 0,\ \ \theta(1) = 0,\ \ \phi(1) = 0\,. \end{cases} \tag{16}$$

In conclusion, once Equations (12)–(15) are resolved together with the boundary conditions given in Equation (16), the Nusselt number which is denoted by N_u, the skin friction coefficient which is denoted by C_f, and wall couple stress which is denoted by C_g can be determined for both the top and bottom disks in the following manner [1,2]:

$$C_\mathrm{f} = -\frac{(1+\lambda_1)f''(\pm 1)}{2R_\mathrm{e}},\quad C_\mathrm{g} = \frac{\lambda_3}{2R_\mathrm{e}}\mathrm{g}'(\pm 1),\ \ N_\mathrm{u} = -\theta'(\pm 1)\,. \tag{17}$$

In Equation (17), the local Reynolds number is denoted by $R_\mathrm{e} = \rho S l r/\mu$, the stretching parameter of the disks is denoted by S, the distance from the r-axis is denoted by l, the dynamic viscosity of the fluid is denoted by μ, and r is an arbitrary value for the radius of the disk.

3. Methodology

3.1. Description of the HAN method

The Hybrid Analytical and Numerical method (HAN method), first introduced by A. Ahmadi Azar, is an innovative semi-analytical technique specifically designed to address complicated systems of nonlinear differential equations. This method uniquely combines numerical and analytical approaches, making it highly versatile and flexible. The process begins with obtaining a precise numerical solution, which

serves as the foundation for constructing an analytical framework. Unlike traditional methods, the HAN method is not limited to specific numerical techniques; it requires only an accurate numerical solution, allowing for broader applicability across diverse problems. This adaptability is one of its greatest strengths, as it enables the effective handling of highly nonlinear equations. By integrating numerical data into the development of an analytical solution, the HAN method bridges the gap between purely numerical and purely analytical approaches, offering a powerful tool for solving challenging mathematical problems in engineering, physics, and other applied sciences. Since its introduction, the HAN method has been successfully employed in numerous studies, demonstrating its capability to solve a wide range of nonlinear ordinary differential equations and solidifying its value in advancing research across various fields. Another strength of this method is that a power series with a much smaller number of terms than other semi-analytical solutions can be considered as an approximate analytical solution for the given nonlinear differential equation. To describe the HAN method, let us consider a non-linear differential equation of order m (= 2, 3, ...) as follows:

$$\Gamma\left(u(\xi), u'(\xi), u''(\xi), \ldots, u^{(m)}(\xi)\right) = 0, \tag{18}$$

where $0 \le \xi \le b$ is an independent real variable, $u(\xi)$ a real-valued continuous function of the variable ξ, Γ a known function of the variables ξ, $u(\xi)$, and its derivatives of $u(\xi)$ with respect to ξ, i.e., $u^{(i)}(\xi) = \mathrm{d}^i u/\mathrm{d}\xi^i$ $(i = 1, \cdots, m)$ and $b \in \mathbb{R}^+ = (0, +\infty)$ a given positive real number. Suppose that $2m$ boundary conditions (BCs) of the Equation (18) at the boundary points $\{\xi = 0, \xi = b\}$ on the interval $[0, b]$ are as follows:

$$\begin{cases} u(\xi) = \Phi_{00}, \quad u'(\xi) = \Phi_{10}, \ \ \ldots, \ \ u^{(m-1)}(\xi) = \Phi_{(m-1)0}, \ \text{when } \xi = 0\,, \\ u(\xi) = \Phi_{0b}, \quad u'(\xi) = \Phi_{1b}, \ \ \ldots, \ \ u^{(m-1)}(\xi) = \Phi_{(m-1)b}, \ \text{when } \xi = b\,. \end{cases} \tag{19}$$

where Φ_{00}, $\cdots$, $\Phi_{(m-1)0}$, Φ_{0b}, $\cdots$, $\Phi_{(m-1)b}$ are known real numbers: $\Phi_{ij} \in \mathbb{R} = (-\infty, +\infty), i = 0,1, \cdots, m-1; j = 0, b$. In fact, the Equation (18) with $2m$ boundary conditions in Equation (19) is a boundary value problem (BVP). The existence and uniqueness of the solutions to this problem is an important theorem in the theory of differential equations. This theorem, known as "Picard's existence theorem is due to C-É. Picard (1856–1941). Let us suppose that the BVP, Equation (18), with its BCs in Equation (19), has a solution, and this is unique. This section aims to see how to solve analytically the m-order nonlinear Equation (18) with its BCs in Equation (19) by the HAN method. For this purpose, let's consider an approximate solution for the Equation (18) as a polynomial of degree n (= 0, 1, $\cdots$) in terms of the variable ξ:

$$u(\xi) = P_n(\xi) := \sum_{i=0}^{n} a_i \xi^i\,, \tag{20}$$

where $n + 1$ coefficients a_0, a_1, …, a_n in the polynomial solution in Equation (20) are unknown real numbers: $a_i \in \mathbb{R} = (-\infty, +\infty), i = 0, 1, \cdots, n$. To find these unknowns, one needs $n + 1$ algebraic equations, such that these equations form a system of $n + 1$ equations for $n + 1$ unknowns. By solving this set of algebraic

equations simultaneously, one can find the unknowns a_0, a_1, ⋯, a_n. Now, by substituting the power series of Equation (20) into the BCs of Equation (19) at the boundary points $\{\xi = 0, \xi = b\}$, yield the following algebraic equations for the unknowns a_0, a_1, ⋯, a_n:

$$\begin{aligned}
&u(0) = a_0 := \Phi_{00},\\
&u'(0) = a_1 := \Phi_{10},\\
&\quad\vdots\\
&u^{(m-1)}(0) = a_{m-1} := \Phi_{(m-1)0},\\
&u(b) = \sum_{i=0}^{n} a_i b^i := \Phi_{0b},\\
&u'(b) = \sum_{i=1}^{n} i a_i b^{i-1} := \Phi_{1b},\\
&\quad\vdots\\
&u^{(m-1)}(b) = \sum_{i=m-1}^{n} i(i-1)(i-2)\cdots\big(i-(m-2)\big) a_i b^{i-(m-1)} := \Phi_{(m-1)b},
\end{aligned} \tag{21}$$

where

$$\Phi_{ij} := u^{(i)}(j) = \frac{\partial u^i}{\partial \xi^i}(\xi = j), \quad i = 0,1,\cdots,m-1; j = 0, b, \tag{22}$$

are $2m$ real numbers: $\Phi_{ij} \in \mathbb{R} = (-\infty, +\infty)$.

By using a numerical solution method (it is not limited to a specific method and can be any numerical method) for the Equation (18), it is possible to find $2m$ real numbers of Φ_{ij}s that appeared in the system of algebraic equations in Equation (21). By determining these numbers, Equation (21) will be a system of algebraic equations for the unknowns a_0, a_1, ..., a_n. in this way, $2m$ number of $2n+1$ algebraic equations needed to find the coefficients a_0, a_1, ..., a_n are provided. If we choose the number of terms in polynomial $P_n(\xi)$ sufficiently large, then this polynomial will be the solution of Equation (18) with high accuracy. So, for the polynomial solution of Equation (20) to be the solution of Equation (18) with high accuracy, we choose n as a large natural number. Then, $n+1$ is a large number, and consequently $n+1 > 2m$. This inequality shows that the number of the constructed algebraic equations from the BCs, $2m$, is less than the number of unknowns. Then, one needs $n+1-2m := k$ algebraic equations. By adding these equations to Equation (21), therefore, one has a system of $n+1$ equations for $n+1$ unknowns. In constructing $n+1-2m$ algebraic equations, we need the numerical solution of the Equation (18). Suppose that we have somehow reached the numerical solution. Using this numerical solution, the required algebraic equations can be made. For this purpose, we choose the distinct points ξ_0, ξ_1, ⋯, ξ_k on the interval $[0, b]$, such that $0 < \xi_1 < \xi_2 < \cdots < \xi_k < b$. Using the numerical solution of Equation (18), the function $u(\xi)$ and its derivatives from the first order to the $(m-1)$-order to the variable ξ at each point $\xi_1, \xi_2, \cdots, \xi_k$ can be determined. We note that the derivative of the l-th order ($l = 1, 2, \cdots, m-1$) of the polynomial solution of Equation (20) to the variable ξ can be expressed by the following formula:

$$u^{(l)}(\xi) = \sum_{i=l}^{n} i(i-1)\cdots\big(i-(l-1)\big)a_i\xi^{i-l}, \quad l = 1,2,\cdots,m-1. \tag{23}$$

By substituting $\xi_1, \xi_2, \cdots, \xi_k$ in Equation (23), one has the following algebraic equations:

$$\begin{aligned}
&\xi_1\colon\ u^{(0)}(\xi_1) = \sum_{i=l}^{n} a_i {\xi_1}^i := \Phi_{01},\\
&\xi_1\colon\ u^{(l)}(\xi_1) = \sum_{i=l}^{n} i(i-1)\cdots\big(i-(l-1)\big)a_i {\xi_1}^{i-l} := \Phi_{l1},\ \ l = 1,2,\cdots\\
&\qquad\vdots\\
&\xi_k\colon\ u^{(0)}(\xi_k) = \sum_{i=l}^{n} a_i {\xi_k}^i := \Phi_{lk},\\
&\xi_k\colon\ (\xi_k) = \sum_{i=l}^{n} i(i-1)\cdots\big(i-(l-1)\big)a_i {\xi_k}^{i-l} := \Phi_{lk},\quad l = 1,2,\cdots,m
\end{aligned} \tag{24}$$

These equations are called the approximate boundary conditions for the Equation (18). Then, by using the numerical solution of the given ODE and by choosing the real numbers $\xi_1, \xi_2, \cdots, \xi_k$ on the interval $[0, b]$, the real numbers Φ_{lk}, $l = 0,1,\cdots,m-1;\ k = 1,\cdots,(n+1)/m-2$, can be provided. For example, to have four numbers ξ_1, ξ_2, ξ_3, ξ_4 on the interval $[0, b]$, and for a second-order ODE, $\Gamma\big(u(\xi), u'(\xi), u''(\xi)\big) = 0$, according to the equation between numbers n, m, k, i.e., $n = m(k+2)-1$, we have $n = 11$. In this case, $k = 4$, $m = 2$, and $n = 11$, the finite power series solution to the ODE, $\Gamma\big(u(\xi), u'(\xi), u''(\xi)\big) = 0$ is a polynomial of degree $n = 11$ in terms of the variable ξ as follows:

$$u(\xi) = P_{11}(\xi) := \sum_{i=0}^{11} a_i\xi^i = a_0 + a_1\xi + \cdots + a_{11}\xi^{11}. \tag{25}$$

To find the unknowns a_0, a_1, ⋯, a_{11}, according to the Equations (21) and (23), we have the following system of twelve algebraic equations with twelve unknowns as BCs:

$$\begin{aligned}
\xi_0\colon u^{(0)}(\xi_0) &= \sum_{i=0}^{11} a_i {\xi_0}^i = a_0 := \Phi_{00},\\
\xi_0\colon u^{(l)}(\xi_0) &= \sum_{i=1}^{11} i a_i {\xi_0}^{i-1} = a_1 := \Phi_{l1},\\
\xi_1\colon u^{(0)}(\xi_1) &= \sum_{i=0}^{11} a_i {\xi_1}^i = a_0 + a_1\xi_1^1 + a_2\xi_1^2 + \cdots + a_{11}\xi_1^{11} := \Phi_{01},\\
\xi_1\colon u^{(1)}(\xi_1) &= \sum_{i=1}^{11} i a_i {\xi_1}^{i-1} = a_1 + 2a_2\xi_1 + 3a_3\xi_1^2 + \cdots + 11a_{11}\xi_1^{10} := \Phi_{,01},\\
&\vdots
\end{aligned} \tag{26}$$

$$\xi_5: u^{(0)}(\xi_5) = \sum_{i=0}^{11} a_i {\xi_5}^i = a_0 + a_1\xi_5^1 + a_2\xi_5^2 + \cdots + a_{11}\xi_5^{11} := \Phi_{05},$$
$$\xi_5: u^{(1)}(\xi_5) = \sum_{i=1}^{11} i a_i {\xi_5}^{i-1} = a_1 + 2a_2\xi_5 + 3a_3\xi_5^2 + \cdots + 11a_{11}\xi_5^{10} := \Phi_{15}. \quad (26)$$

where $\xi_0 = 0$ and $\xi_5 = b$. By using a numerical solution method, one can determine the twelve numbers Φ_{ij}, $i = 0{,}1; j = 0, 1, \cdots, 5$. By substituting these determined numbers into the above system of equations (26) and then by solving this system, the unknowns $a_0, a_1, \cdots, a_{11}$ can be obtained simultaneously. In the final stage, putting a_0, a_1, $\cdots$, a_{11} in the polynomial Equation (25), the solution of the ODE, $\Gamma\big(u(\xi), u'(\xi), u''(\xi)\big) = 0$, can be found. This solution is a polynomial of degree $n = 11$ in terms of the variable $0 \le \xi \le b$ with the known coefficients. The HAN-method is a technique for solving a nonlinear differential equation with a numerical solution. By solving a system of equations with $n + 1$ unknowns and $n + 1$ Equation (21) that were made earlier, the coefficients of Equation (20) are determined, and then this obtained polynomial can be considered as the semi-analytical solutions of Equation (18). As mentioned earlier in this section, it should be considered that only a limited part of the Akbari-Ganji-method overlaps with the HAN-method and these two methods are completely different. The former version of the Akbari-Ganji-method is fully described in the study of Pattnaik et al. [81] while modified version of this method is described by many studies [64,68,70,72].

3.2. Application of the HAN-method

To apply the HAN-method for the Equations (12)–(15), first, the following polynomials with unknown constant coefficients should be assumed as the semi-analytical solutions:

$$f(\xi) = \sum_{i=0}^{12} a_i \xi^i = a_0 + a_1\xi^1 + a_2\xi^2 + \cdots + a_{12}\xi^{12}, \quad (27)$$

$$g(\xi) = \sum_{i=0}^{10} b_i \xi^i = b_0 + b_1\xi^1 + b_2\xi^2 + \cdots + b_{10}\xi^{10}, \quad (28)$$

$$\theta(\xi) = \sum_{i=0}^{10} c_i \xi^i = c_0 + c_1\xi^1 + c_2\xi^2 + \cdots + c_{10}\xi^{10}, \quad (29)$$

$$\phi(\xi) = \sum_{i=0}^{10} d_i \xi^i = d_0 + d_1\xi^1 + d_2\xi^2 + \cdots + d_{10}\xi^{10}. \quad (30)$$

In a special case, when in the Equations (12)–(15), the value of parameters $M_{\mathrm{n}} = 1$, $S_{\mathrm{c}} = 0.5$, $R_0 = 20$, $E_{\mathrm{c}} = 0.2$, $N_{\mathrm{r}} = 1$, $P_{\mathrm{r}} = 0.7$, $\lambda_3 = 0.3$, $\lambda_2 = 0.2$, $\lambda_1 = 2$, and by applying the HAN-method, the analytical solutions of the Equations (12)–(15) are obtained. Based on Equations (27)–(30), there are 46 unknowns. So, we need 46 linear algebraic equations in terms of the unknowns of a_is, b_is, c_is, and d_is, to obtain these

unknowns. The BCs in Equation (16) makes only ten equations as follows:

$$\begin{cases} f(\xi)=0,\ \dfrac{\mathrm{d}f(\xi)}{\mathrm{d}\xi}=-2,\ g(\xi)=0,\ \theta(\xi)=1,\ \phi(\xi)=1,\ \text{when } \xi=-1, \\ f(\xi)=0,\ \dfrac{\mathrm{d}f(\xi)}{\mathrm{d}\xi}=-2,\ g(\xi)=0,\ \theta(\xi)=0,\ \phi(\xi)=0,\ \text{when } \xi=1, \end{cases} \tag{31}$$

and the remaining 36 equations should be made through numerical solutions. The results of the numerical solution of the Equations (12)–(15), with the values of parameters $M_{\mathrm{n}}=1$, $S_{\mathrm{c}}=0.5$, $R_0=20$, $E_{\mathrm{c}}=0.2$, $N_{\mathrm{r}}=1$, $P_{\mathrm{r}}=0.7$, $\lambda_3=0.3$, $\lambda_2=0.2$, $\lambda_1=2$ are shown in **Table 1**:

Table 1. Results of numerical solution in Maple software.

ξ	$f(\xi)$	$g(\xi)$	$\theta(\xi)$	$\phi(\xi)$
−1	0	0	1	1
−0.8	−0.246005124491156	0.817889422276519	0.864417323523375	0.967184480779807
−0.6	−0.287412078985710	0.699224476135717	0.747139598839239	0.914803387876689
−0.4	−0.228582538070867	0.436491652089539	0.659933009990955	0.823375085853292
−0.2	−0.123414668423391	0.203695046637467	0.592730707383331	0.680935972701367
0	0	0	0.534632113764447	0.499999999998872
0.2	0.123414668424025	−0.203695046644449	0.476515794697461	0.319064027300319
0.4	0.228582538071048	−0.436491652086817	0.408964493290973	0.176624914147266
0.6	0.287412078985752	−0.699224476135717	0.319284654492353	0.0851966121235713
0.8	0.246005124491164	−0.817889422276190	0.189129334005668	0.0328155192202959
1	0	0	0	0

It is possible to look at the numerical solution results given in **Table 1** as approximate boundary conditions and create new equations from them. Considering that 36 equations need to be constructed, the approximate boundary conditions have been used to construct 36 equations in **Table 1**.

Considering the ten equations that were created by the boundary conditions of the problem and the 36 equations that were created by the approximate boundary conditions, a system of equations with 46 equations and 46 unknowns can be made, and by solving this system of equations, all the unknown coefficients of the Equations (12)–(15) are known. **Table 2** shows all the calculated coefficients.

Table 2. The semi-analytical solutions a_is, b_is and c_is, d_is of the polynomial solutions of Equations (27)–(30) by using Maple software.

i	a_i	b_i	c_i	d_i
0	0	0	0.5346321138	0.5000000000
1	0.6308526290	−0.9932581054	−0.2832663661	−0.9423864576
2	$1.314855659 \times 10^{-11}$	$-1.535799231 \times 10^{-10}$	0.00001313734819	$7.486085590 \times 10^{-11}$
3	−0.3361243916	−0.6268107312	−0.1789459199	0.9819150125
4	$-1.542107247 \times 10^{-10}$	$1.932409400 \times 10^{-9}$	−0.005556420643	$-7.351507187 \times 10^{-10}$
5	−0.2056198917	−0.1486907388	−0.07035631327	−1.008168042

Table 2. (*Continued*).

i	a_i	b_i	c_i	d_i
6	$6.358924750 \times 10^{-10}$	$-7.275123879 \times 10^{-9}$	−0.006849781331	$2.522186822 \times 10^{-9}$
7	−0.08199370720	1.443336356	−0.009636316660	0.6813602413
8	$-1.172739046 \times 10^{-9}$	$1.032999352 \times 10^{-8}$	−0.02330796936	$-3.427124023 \times 10^{-9}$
9	−0.02891848919	0.3254232194	0.04220491593	−0.2127207541
10	$9.889007828 \times 10^{-10}$	$-4.833699114 \times 10^{-9}$	0.001068920224	$1.566355064 \times 10^{-9}$
11	0.02180385067	-	-	-
12	$-3.109920437 \times 10^{-10}$	-	-	-

Therefore, the semi-analytical solutions of the Equations (12)–(15) are the following polynomials with known coefficients (given in **Table 2**):

$$\begin{aligned} f(\xi) = {} & -3.109920437 \times 10^{-10}\xi^{12} + 0.02180385067\xi^{11} + 9.889007828 \times 10^{-10}\xi^{10} \\ & -0.02891848919\xi^{9} - 1.172739046 \times 10^{-9}\xi^{8} - 0.08199370720\xi^{7} \\ & +6.358924750 \times 10^{-10}\xi^{6} - 0.2056198917\xi^{5} - 1.542107247 \times 10^{-10}\xi^{4} \\ & -0.3361243916\xi^{3} + 1.314855659 \times 10^{-11}\xi^{2} + 0.6308526290\xi, \end{aligned} \tag{32}$$

$$\begin{aligned} g(\xi) = {} & -4.833699114 \times 10^{-9}\xi^{10} + 0.3254232194\xi^{9} + 1.032999352 \times 10^{-8}\xi^{8} \\ & +1.443336356\xi^{7} - 7.275123879 \times 10^{-9}\xi^{6} - 0.1486907388\xi^{5} \\ & +1.932409400 \times 10^{-9}\xi^{4} - 0.6268107312\xi^{3} - 1.535799231 \times 10^{-10}\xi^{2} \\ & -0.9932581054\xi, \end{aligned} \tag{33}$$

$$\begin{aligned} \theta(\xi) = {} & 0.001068920224\xi^{10} + 0.04220491593\xi^{9} - 0.02330796936\xi^{8} \\ & -0.009636316660\xi^{7} - 0.006849781331\xi^{6} - 0.07035631327\xi^{5} \\ & -0.005556420643\xi^{4} - 0.1789459199\xi^{3} + 0.00001313734819\xi^{2} \\ & -0.2832663661\xi + 0.5346321138, \end{aligned} \tag{34}$$

$$\begin{aligned} \phi(\xi) = {} & 1.566355064 \times 10^{-9}\xi^{10} - 0.2127207541\xi^{9} - 3.427124023 \times 10^{-9}\xi^{8} \\ & +0.6813602413\xi^{7} + 2.522186822 \times 10^{-9}\xi^{6} - 1.008168042\xi^{5} \\ & -7.351507187 \times 10^{-10}\xi^{4} + 0.9819150125\xi^{3} + 7.486085590 \times 10^{-11}\xi^{2} \\ & -0.9423864576\xi + 0.5000000000, \end{aligned} \tag{35}$$

According to the known coefficients in **Table 2** and by substituting the semi-analytical solutions Equations (32)–(35) in the Equations (12)–(15), the following functions are obtained:

$$\begin{aligned} F(\xi) = {} & -0.72111048\xi - 510.5054373\xi^{9} + 9.208327727 \times 10^{-6}\xi^{10} \\ & +50.68002728\xi^{11} + 7.246234031 \times 10^{-7}\xi^{2} + 23.6729104\xi^{3} \\ & -6.846259567 \times 10^{-6}\xi^{4} - 188.6953981\xi^{5} - 2.553303752 \times 10^{-15}\xi^{21} \\ & +3.132740726 \times 10^{-7}\xi^{20} - 9.413076502\xi^{19} - 1.065495063 \times 10^{-6}\xi^{18} \\ & +18.84036847\xi^{17} + 34.47699268\xi^{15} - 1.134311440 \times 10^{-6}\xi^{14} \\ & +60.28961826\xi^{13} - 1.101479475 \times 10^{-8}, \end{aligned} \tag{36}$$

$$
\begin{aligned}
G(\xi) = {} & -3.955372750 \times 10^{-11} + 0.064479380\xi + 7.387427951\xi^{9} \\
& +1.150987074 \times 10^{-7}\xi^{10} + 8.269281386\xi^{11} - 2.739344998 \times 10^{-8}\xi^{12} \\
& +1.734175481 \times 10^{-7}\xi^{6} - 26.72537277\xi^{7} - 2.176380812 \times 10^{-7}\xi^{8} \\
& +4.451253930 \times 10^{-9}\xi^{2} - 1.987728644\xi^{3} - 5.154374818 \times 10^{-8}\xi^{4} \\
& +13.54304810\xi^{5} - 2.405187146 \times 10^{-17}\xi^{21} + 3.111526954 \times 10^{-9}\xi^{20} \\
& -0.0993367099\xi^{19} - 8.681084360 \times 10^{-9}\xi^{18} - 0.0194282808\xi^{17} \\
& -9.40604969 \times 10^{-9}\xi^{16} + 0.997925442\xi^{15} + 2.10391033 \times 10^{-9}\xi^{14} \\
& +3.251304946\xi^{13},
\end{aligned} \tag{37}
$$

$$
\begin{aligned}
\Theta(\xi) = {} & -0.003452233\xi + 0.00006130762489 - 5.415773831\xi^{9} \\
& -0.4398051432\xi^{10} + 1.058580205\xi^{11} - 0.7311598925\xi^{12} \\
& -1.709032870\xi^{6} + 4.160236008\xi^{7} + 2.899239036\xi^{8} \\
& -0.01345753001\xi^{2} + 0.125044258\xi^{3} + 0.2974912040\xi^{4} \\
& -1.179098979\xi^{5} + 4.653959590 \times 10^{-11}\xi^{21} \\
& -0.003262919118\xi^{20} - 0.1159489481\xi^{19} + 0.2625816501\xi^{18} \\
& +0.1743739899\xi^{17} - 0.4002439803\xi^{16} + 0.5161009724\xi^{15} \\
& -0.6195609969\xi^{14} + 1.037467902\xi^{13},
\end{aligned} \tag{38}
$$

$$
\begin{aligned}
\Phi(\xi) = {} & -0.053579667\xi + 1.497217118 \times 10^{-10} - 19.88694744\xi^{9} \\
& +7.869389009 \times 10^{-8}\xi^{10} - 0.2961980010\xi^{11} + 1.166591089 \times 10^{-7}\xi^{12} \\
& -9.807304522 \times 10^{-8}\xi^{6} + 26.43191200\xi^{7} - 3.87471243 \times 10^{-8}\xi^{8} \\
& -8.001195487 \times 10^{-9}\xi^{2} + 1.58753993\xi^{3} + 5.845206685 \times 10^{-8}\xi^{4} \\
& -11.14677643\xi^{5} - 4.871239625 \times 10^{-17}\xi^{21} + 9.369158776 \times 10^{-9}\xi^{20} \\
& -0.4174318401\xi^{19} - 4.427283003 \times 10^{-8}\xi^{18} + 1.593580042\xi^{17} \\
& +8.367944055 \times 10^{-8}\xi^{16} - 0.9086121950\xi^{15} - 1.418626638 \times 10^{-7}\xi^{14} \\
& +2.125878689\xi^{13}.
\end{aligned} \tag{39}
$$

According to **Figure 2**, by plotting the functions F, G, Θ, and Φ, that is, Equations (36)–(39), it is possible to validate the accuracy of the analytical results solved by the HAN-method:

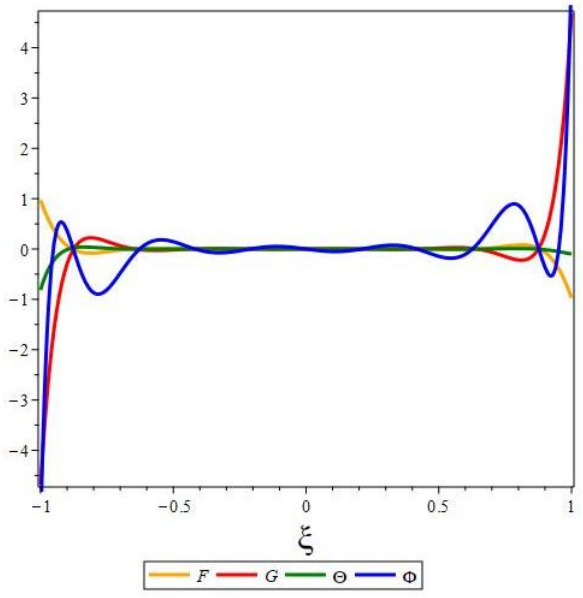

Figure 2. The accuracy of the results by the HAN-method.

3.3. Description of the modified Akbari-Ganji-method

The Akbari-Ganji-method was developed for the analytical solution of nonlinear differential equations. This semi-analytical method has been approximated the governing equations in many problems for which no exact analytical solutions exist. So far, many studies, used this method to solve non-linear and unsolvable mechanical engineering problems. However, due to the need for more accurate solutions, in this study, the Akbari-Ganji method is modified. To explain the main idea of this method, let us consider the general form of the differential equation of order-m as follows:

$$\Xi:\ \Gamma\left(u, u', u'', \ldots, u^{(m)}\right) = 0; \quad u := u(\xi). \tag{40}$$

with the following BCs:

$$\begin{cases} u(\xi) = \Phi_{00}, \ \ u'(\xi) = \Phi_{10}, \cdots, \ \ u^{(m-1)}(\xi) = \Phi_{(m-1)0}, & \text{when } \xi = 0, \\ u(\xi) = \Phi_{0b}, \ \ u'(\xi) = \Phi_{1b}, \cdots, \ \ u^{(m-1)}(\xi) = \Phi_{(m-1)b}, & \text{when } \xi = b. \end{cases} \tag{41}$$

In Equation (41), $\{\xi = 0, \xi = b\}$ are boundary points. To solve Equation (40), the solution can be considered as a polynomial with degree n and constant and unknown coefficients:

$$u(\xi) = \sum_{i=0}^{n} a_i \xi^i = a_0 + a_1\xi^1 + a_2\xi^2 + \cdots + a_n\xi^n\,. \tag{42}$$

In Equation (42), the degree of the polynomial solution is assumed to be greater than the order of the differential equation in Equation (40). There is an $n+1$ constant and unknown coefficient the Equation (42). To determine these coefficients, $n+1$ equations must be made. The boundary conditions of the problem, i.e., Equation (41), can make some of these equations as follows:

$$\begin{aligned} &u(0) = a_0 := \Phi_{00}, \\ &u'(0) = a_1 := \Phi_{10}, \\ &\quad\vdots \\ &u^{(m-1)}(0) = a_{m-1} := \Phi_{(m-1)0}, \\ &u(b) = \sum_{i=0}^{n} a_i b^i := \Phi_{0b}, \\ &u'(b) = \sum_{i=1}^{n} i a_i b^{i-1} := \Phi_{1b}, \\ &\quad\vdots \\ &u^{(m-1)}(b) = \sum_{i=m-1}^{n} i(i-1)\cdots\big(i-(m-2)\big) a_i b^{i-(m-1)} := \Phi_{(m-1)b} \end{aligned} \tag{43}$$

where

$$\Phi_{ij} := u^{(i)}(j) = \frac{\partial u^i}{\partial \xi^i}(\xi = j), \quad i = 0,1,\cdots,m-1;\ j = 0, b \tag{44}$$

there are $2m$ real numbers: $\Phi_{ij} \in \mathbb{R} = (-\infty, +\infty)$. Equations made from the boundary conditions of the problem, as seen in Equation (43) are limited due to the assumption that $n > m$. But to build a system of $n+1$ unknowns and $n+1$ equations, more equations are needed. Therefore, the remaining equations can be

created by replacing the approximate solution Equation (42) in Equation (40) as follows:

$$\Xi: \begin{cases} \Gamma\left(u(0), u'(0), u''(0), \ldots, u^{(m-1)}(0)\right) = 0, \\ \Gamma\left(u(b/2), u'(b/2), u''(b/2), \ldots, u^{(m-1)}(b/2)\right) = 0, \\ \Gamma\left(u(b), u'(b), u''(b), \ldots, u^{(m-1)}(b)\right) = 0, \end{cases} \tag{45}$$

$$\Xi': \begin{cases} \Gamma\left(u'^{(0)}, u''(0), u'''(0), \ldots, u^{(m-1)}(0)\right) = 0, \\ \Gamma\left(u'(b/2), u''(b/2), u'''(b/2), \ldots, u^{(m-1)}(b/2)\right) = 0, \\ \Gamma\left(u'(b), u''(b), u'''(b), \ldots, u^{(m-1)}(b)\right) = 0, \end{cases} \tag{46}$$

$$\Xi'': \begin{cases} \Gamma\left(u''^{(0)}, u'''(0), u''''(0), \ldots, u^{(m-1)}(0)\right) = 0, \\ \Gamma\left(u''(b/2), u'''(b/2), u''''(b/2), \ldots, u^{(m-1)}(b/2)\right) = 0, \\ \Gamma\left(u''(b), u'''(b), u''''(b), \ldots, u^{(m-1)}(b)\right) = 0. \end{cases} \tag{47}$$

Therefore, extracting as many equations as needed from Equations (45)–(47) is possible to make a system of algebraic equations containing $n+1$ unknowns and $n+1$ equations. In another step, by solving this system of algebraic equations, the coefficients $a_1, a_2, \ldots, a_n$ are obtained. By substituting these known coefficients in the polynomial Equation (42), the desired solution of ODE Equation (40) is obtained.

3.4. Application of the modified Akbari-Ganji-method

In this section, the modified Akbari-Ganji-method is explained to solve the equations governing the physics of the problem analytically. First, the following polynomials are approximate solutions for the system of ODEs of Equations (12)–(15), when the values of the parameters $M_{\mathrm{n}} = 1$, $S_{\mathrm{c}} = 0.5$, $R_0 = 20$, $E_{\mathrm{c}} = 0.2$, $N_{\mathrm{r}} = 1$, $P_{\mathrm{r}} = 0.7$, $\lambda_3 = 0.3$, $\lambda_2 = 0.2$, $\lambda_1 = 2$, are considered as follows:

$$f(\xi) = \sum_{i=0}^{13} a_i \xi^i = a_0 + a_1\xi^1 + a_2\xi^2 + \cdots + a_{13}\xi^{13}, \tag{48}$$

$$g(\xi) = \sum_{i=0}^{11} b_i \xi^i = b_0 + b_1\xi^1 + b_2\xi^2 + \cdots + b_{11}\xi^{11}, \tag{49}$$

$$\theta(\xi) = \sum_{i=0}^{11} c_i \xi^i = c_0 + c_1\xi^1 + c_2\xi^2 + \cdots + c_{11}\xi^{11}, \tag{50}$$

$$\phi(\xi) = \sum_{i=0}^{11} d_i \xi^i = d_0 + d_1\xi^1 + d_2\xi^2 + \cdots + d_{11}\xi^{11}. \tag{51}$$

According to the Equations (48)–(51), there are 50 unknown coefficients in the solutions, and to determine these coefficients, 50 equations must be made. The boundary conditions of the problem can only provide 10 of these equations as follows:

$$\begin{cases} f(\xi)=0, \quad \dfrac{\mathrm{d}f(\xi)}{\mathrm{d}\xi}=-2, \quad g(\xi)=0, \ \theta(\xi)=1, \ \phi(\xi)=1, \ \text{when } \xi=-1, \\ f(\xi)=0, \quad \dfrac{\mathrm{d}f(\xi)}{\mathrm{d}\xi}=-2, \quad g(\xi)=0, \quad \theta(\xi)=0, \ \phi(\xi)=0, \ \text{when } \xi=1. \end{cases} \tag{52}$$

Due to the higher degree of polynomials in Equations (48)–(51) compared to the order of differential Equations (12)–(15), the number of constructed equations was not enough, and 40 other equations must be made. The numbers -1, -0.5, 0, 0.5, and 1 form the boundary points set of the problem in the modified Akbari-Ganji-method which is as follows:

$$\text{Boundary Points} = \text{B.P} = \{-1, -0.5, 0, 0.5, 1\}. \tag{53}$$

In the Mirgolbabaee et al. [82] study, the boundary points were only assumed to be -1 and 1 because, in the Akbari-Ganji-method, numbers -0.5 and 0.5 were not assumed. Using boundary points Equation (53) shows the difference between the modified Akbari-Ganji-method in this study. The B.P. Equation (53) can be used in making the other 40 equations as follows.

$$F\big(f(\text{B.P}), g(\text{B.P})\big) \to F\big(f(\text{B.P}), g(\text{B.P})\big) = 0, F'\big(f(\text{B.P}), g(\text{B.P})\big) = 0, \tag{54}$$

$$G\big(f(\text{B.P}), g(\text{B.P})\big) \to G\big(f(\text{B.P}), g(\text{B.P})\big) = 0, G'\big(f(\text{B.P}), g(\text{B.P})\big) = 0, \tag{55}$$

$$\Theta\big(f(\text{B.P}), \theta(\text{B.P})\big) \to \Theta\big(f(\text{B.C}), \theta(\text{B.P})\big) = 0, \Theta'\big(f(\text{B.C}), \theta(\text{B.P})\big) = 0, \tag{56}$$

$$\Phi\big(f(\text{B.P}), \phi(\text{B.P})\big) \to \Phi\big(f(\text{B.P}), \phi(\text{B.P})\big) = 0, \Phi'\big(f(\text{B.P}), \phi(\text{B.P})\big) = 0. \tag{57}$$

By using Equations (54)–(57), the remaining 40 equations can be made. In this way, an algebraic equation system including 50 equations and 50 unknowns is provided. By solving this system of algebraic equations by EES software, the unknown coefficients of polynomial Equations (48)–(51) are known. The results of these calculations are listed in **Table 3**.

Table 3. Coefficients of calculated semi-analytical solutions of $f(\xi)$, $g(\xi)$, $\theta(\xi)$, and $\phi(\xi)$ by using EES software.

i	a_i	b_i	c_i	d_i
0	1.305×10^{-09}	-1.503×10^{-09}	0.538	0.5
1	0.6333	−1.004	−0.2839	−0.9512
2	-2.633×10^{-09}	4.080×10^{-09}	−1.111 × 10−09	6.206×10^{-09}
3	−0.3388	−0.6784	−0.1798	1.004
4	2.744×10^{-10}	1.393×10^{-08}	−0.0176	-1.094×10^{-08}
5	−0.2071	0.4447	−0.06483	−1.084
6	3.158×10^{-09}	-3.530×10^{-08}	0.03249	1.179×10^{-08}
7	−0.07114	−0.7459	−0.03616	0.8653
8	-3.434×10^{-09}	2.523×10^{-08}	−0.07994	-6.729×10^{-09}
9	−0.05654	3.427	0.08456	−0.4226

Table 3. (*Continued*).

i	a_i	b_i	c_i	d_i
10	1.630×10^{-09}	-6.430×10^{-09}	0.0271	1.577×10^{-09}
11	0.04948	−1.444	−0.01995	0.08855
12	-3.006×10^{-10}	-	-	-
13	−0.009136	-	-	-

Therefore, Equations (48)–(51) with known coefficients in **Table 3** are as follows:

$$\begin{aligned} f(\xi) = & -0.0091358675903062\xi^{13} - 3.0059935486316 \times 10^{-10}\xi^{12} \\ & +0.049479419881825\xi^{11} + 1.62959137088580 \times 10^{-9}\xi^{10} \\ & -0.056541511493550\xi^{9} - 3.43395702881180 \times 10^{-9}\xi^{8} \\ & -0.071135119727114\xi^{7} + 3.1584256271901 \times 10^{-9}\xi^{6} \\ & -0.20708488641248\xi^{5} + 2.7441666680975 \times 10^{-10}\xi^{4} \\ & -0.33884071588679\xi^{3} - 2.6326450840098 \times 10^{-9}\xi^{2} \\ & +0.63325868122841\xi + 1.3047692846982 \times 10^{-9}, \end{aligned} \tag{58}$$

$$\begin{aligned} g(\xi) = & -1.44393704751119\xi^{11} - 6.4300521802920 \times 10^{-9}\xi^{10} \\ & +3.42742904550680\xi^{9} + 2.5225974250684 \times 10^{-8}\xi^{8} \\ & -0.74586721719866\xi^{7} - 3.5298912095728 \times 10^{-8}\xi^{6} \\ & +0.44470574614560\xi^{5} + 1.3925998374323 \times 10^{-8}\xi^{4} \\ & -0.67840126764621\xi^{3} + 4.0797621819671 \times 10^{-9}\xi^{2} \\ & -1.00392925929570\xi - 1.5027699008770 \times 10^{-9}, \end{aligned} \tag{59}$$

$$\begin{aligned} \theta(\xi) = & -0.019949979396849\xi^{11} + 0.027102934710942\xi^{10} \\ & +0.084557599513564\xi^{9} - 0.079940426193195\xi^{8} \\ & -0.036155780661524\xi^{7} + 0.032489139997977\xi^{6} \\ & -0.064827401988362\xi^{5} - 0.017604748375972\xi^{4} \\ & -0.17975976695144\xi^{3} - 1.1111337095063 \times 10^{-9}\xi^{2} \\ & -0.28386467051539\xi + 0.53795310097138, \end{aligned} \tag{60}$$

$$\begin{aligned} \phi(\xi) = & \ 0.088550403451787\xi^{11} + 1.5765518305027 \times 10^{-9}\xi^{10} \\ & -0.42261174751715\xi^{9} - 6.7286923236797 \times 10^{-9}\xi^{8} \\ & +0.86531978712817\xi^{7} + 1.1793085932528 \times 10^{-8}\xi^{6} \\ & -1.0839867098965\xi^{5} - 1.0940578922658 \times 10^{-8}\xi^{4} \\ & +1.0039674300140\xi^{3} + 6.2057382125988 \times 10^{-9}\xi^{2} \\ & +0.95123916318038\xi + 0.49999999809390. \end{aligned} \tag{61}$$

By substituting the parameters $M_{\mathrm{n}} = 1$, $S_{\mathrm{c}} = 0.5$, $R_0 = 20$, $E_{\mathrm{c}} = 0.2$, $N_{\mathrm{r}} = 1$, $P_{\mathrm{r}} = 0.7$, $\lambda_3 = 0.3$, $\lambda_2 = 0.2$, $\lambda_1 = 2$and also the semi-analytical solutions Equations (58)–(61) in the system of ODEs Equations (12)–(15), the following functions are obtained:

$$\begin{aligned}F(\xi) = {} & 1.05 \times 10^{-6}\xi + 1.617978297 \times 10^{-7} - 2.864487108\xi^{23} \\ & -1.667514441 \times 10^{-7}\xi^{22} + 24.46426562\xi^{21} + 1.412485108 \times 10^{-6}\xi^{20} \\ & -71.40969308\xi^{19} - 4.665128944 \times 10^{-6}\xi^{18} + 58.56010126\xi^{17} \\ & +7.166823992 \times 10^{-6}\xi^{16} - 14.95208524\xi^{15} - 6.205967542 \times 10^{-6}\xi^{14} \\ & +407.7001385\xi^{11} + 1.023646025 \times 10^{-6}\xi^{12} + 51.12723700\xi^{13} \\ & +968.8314803\xi^{7} - 0.00003564085615\xi^{8} - 1156.866646\xi^{9} \\ & +0.00001283945909\xi^{10} - 0.00002209310958\xi^{4} - 293.9639348\xi^{5} \\ & +0.00004302281442\xi^{6} + 3.144794801 \times 10^{-6}\xi^{2} + 29.3736218\xi^{3},\end{aligned} \tag{62}$$

$$\begin{aligned}G(\xi) = {} & -1 \times 10^{-9}\xi + 1.264656650 \times 10^{-9} - 0.2374491182\xi^{23} \\ & -9.50334838 \times 10^{-9}\xi^{22} + 1.884919064\xi^{21} + 7.594561356 \times 10^{-8}\xi^{20} \\ & -4.510551062\xi^{19} - 2.489325876 \times 10^{-7}\xi^{18} + 0.603871120\xi^{17} \\ & +4.008168260 \times 10^{-7}\xi^{16} - 5.093711742\xi^{15} - 2.899888176 \times 10^{-7}\xi^{14} \\ & +72.91571319\xi^{11} - 1.200514615 \times 10^{-7}\xi^{12} - 0.964474048\xi^{13} \\ & +83.69721252\xi^{7} - 8.268409477 \times 10^{-7}\xi^{8} - 128.0173769\xi^{9} \\ & +5.666696327 \times 10^{-7}\xi^{10} - 3.284691732 \times 10^{-7}\xi^{4} - 22.35297628\xi^{5} \\ & +7.405153775 \times 10^{-7}\xi^{6} + 3.857635990 \times 10^{-8}\xi^{2} + 2.074823229\xi^{3},\end{aligned} \tag{63}$$

$$\begin{aligned}\Theta(\xi) = {} & -1 \times 10^{-18} - 0.02806809701\xi^{23} + 0.1057565962\xi^{22} \\ & +0.2493513560\xi^{21} - 0.8125290153\xi^{20} - 0.7332496408\xi^{19} \\ & +2.125434747\xi^{18} + 0.5177206891\xi^{17} - 1.633310018\xi^{16} \\ & +0.07688241553\xi^{15} + 0.2069212252\xi^{14} + 4.268845670\xi^{11} \\ & -0.9537387143\xi^{12} + 0.9939434047\xi^{13} + 13.06567882\xi^{7} \\ & +13.52749523\xi^{8} - 14.76949872\xi^{9} - 4.223471658\xi^{10} \\ & +3.487965768\xi^{4} - 4.050784611\xi^{5} - 11.48225565\xi^{6} \\ & -0.3482685168\xi^{2} + 0.409178712\xi^{3},\end{aligned} \tag{64}$$

$$\begin{aligned}\Phi(\xi) = {} & -0.08898832371\xi^{23} - 4.368318235 \times 10^{-9}\xi^{22} + 0.8294397323\xi^{21} \\ & +4.002490312 \times 10^{-8}\xi^{20} - 2.986078961\xi^{19} - 1.556512418 \times 10^{-7}\xi^{18} \\ & +4.949909265\xi^{17} + 3.346062434 \times 10^{-7}\xi^{16} - 5.693260463\xi^{15} \\ & -4.799888970 \times 10^{-7}\xi^{14} + 8.194318358\xi^{11} + 4.318955214 \times 10^{-7}\xi^{12} \\ & +4.908856700\xi^{13} + 20.73435521\xi^{7} - 4.531249286 \times 10^{-7}\xi^{8} \\ & -25.25068823\xi^{9} - 8.33815240 \times 10^{-10}\xi^{10} - 1.180119054 \times 10^{-7}\xi^{4} \\ & -25.25068823\xi^{9} - 8.33815240 \times 10^{-10}\xi^{10} - 1.180119054 \times 10^{-7}\xi^{4} \\ & -6.21444740\xi^{5} + 3.938015065 \times 10^{-7}\xi^{6} + 1.16509320 \times 10^{-8}\xi^{2} \\ & +0.61658411\xi^{3}.\end{aligned} \tag{65}$$

According to **Figure 3**, by plotting the functions F, G, Θ, and Φ, that is, Equations (62)–(65), it is possible to validate the accuracy of the analytical results solved by the modified AGM:

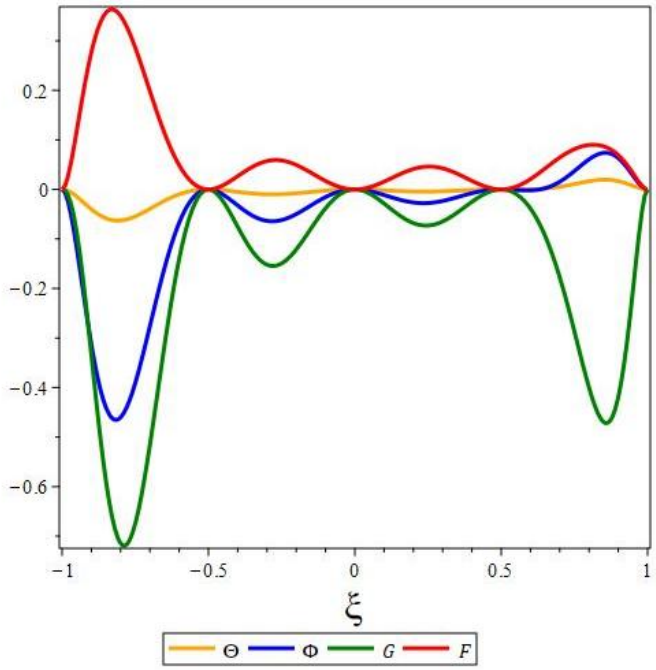

Figure 3. The accuracy of the results by the modified-AGM.

3.5. Validation process

In the validation process, the analytical results were obtained from two applied methods in a special case for Equations (12)–(15) when the values of the parameters $M_{\mathrm{n}} = 1$, $S_{\mathrm{c}} = 0.5$, $R_0 = 20$, $E_{\mathrm{c}} = 0.2$, $N_{\mathrm{r}} = 1$, $P_{\mathrm{r}} = 0.7$, $\lambda_3 = 0.3$, $\lambda_2 = 0.2$, and $\lambda_1 = 2$ have been compared with the results of Agarwal [1]. The comparison of results is shown in tables and graphs. The calculated profiles for axial, radial, microrotation, concentration, and temperature are illustrated in **Figures 4–8** and **Tables 4–9**. The tables and graphs used for validation confirm that the results of this study are accurate when compared to previous research.

Table 4. Comparison of calculated radial velocity when $M_{\mathrm{n}} = 1$, $S_{\mathrm{c}} = 0.5$, $R_0 = 20$, $E_{\mathrm{c}} = 0.2$, $N_{\mathrm{r}} = 1$, $P_{\mathrm{r}} = 0.7$, $\lambda_3 = 0.3$, $\lambda_2 = 0.2$, $\lambda_1 = 2$.

ξ	$f'(\xi)$			
	HAN-method	**Runge-Kutta**	**Modified-AGM**	**Reference [1]**
−1	−2.000000000	−2	−2	−2
−0.8	−0.6039874290	−0.604021502099537	−0.6070542988	−0.605730414
−0.6	0.1048968662	0.104900556292338	0.1043729063	0.0909617336
−0.4	0.4406972324	0.440698332661268	0.4417902710	0.4301777711
−0.2	0.5888353680	0.588833666382915	0.5909080012	0.5949989703
0	0.6308526290	0.630854360417168	0.6332586812	0.6292000000
0.2	0.5888353680	0.588833666383954	0.5909079992	0.5949989703
0.4	0.4406972324	0.440698332660745	0.4417902673	0.4301777711
0.6	0.1048968663	0.104900556292016	0.1043729020	0.0909617336
0.8	−0.6039874290	−0.604021502099592	−0.6070543008	−0.605730414
1	−2	−2	−2	−2

Table 5. Comparison of calculated axial velocity when $M_{\mathrm{n}} = 1$, $S_{\mathrm{c}} = 0.5$, $R_0 = 20$, $E_{\mathrm{c}} = 0.2$, $N_{\mathrm{r}} = 1$, $P_{\mathrm{r}} = 0.7$, $\lambda_3 = 0.3$, $\lambda_2 = 0.2$, $\lambda_1 = 2$.

ξ	$f(\xi)$			
	HAN-method	**Runge-Kutta**	**Modified-AGM**	**Reference [1]**
−1	0	0	0	0
−0.8	−0.2460051244	−0.246005124491156	−0.2465039339	−0.243911560
−0.6	−0.2874120790	−0.287412078985710	−0.2882691344	−0.284291985
−0.4	−0.2285825381	−0.228582538070867	−0.2293677608	−0.225792660
−0.2	−0.1234146684	−0.123414668423392	−0.1238738036	−0.124231180
0	0	0	0	0
0.2	0.1234146684	0.123414668424025	0.1238738060	0.124231180
0.4	0.2285825381	0.228582538071048	0.2293677625	0.225792660
0.6	0.2874120790	0.287412078985752	0.2882691353	0.284291985
0.8	0.2460051245	0.246005124491164	0.2465039341	0.243911560
1	0	0	0	0

Table 6. Comparison of calculated micro-rotation profile when $M_{\mathrm{n}} = 1$, $S_{\mathrm{c}} = 0.5$, $R_0 = 20$, $E_{\mathrm{c}} = 0.2$, $N_{\mathrm{r}} = 1$, $P_{\mathrm{r}} = 0.7$, $\lambda_3 = 0.3$, $\lambda_2 = 0.2$, $\lambda_1 = 2$.

ξ	$g(\xi)$			
	HAN-method	**Runge-Kutta**	**Modified-AGM**	**Reference [1]**
−1	0	0	0	0
−0.8	0.8178894223	0.817889422276519	0.8251948795	0.9384253169
−0.6	0.6992244761	0.699224476135717	0.7058893926	0.7958729497
−0.4	0.4364916521	0.436491652089539	0.4408197093	0.5517536048
−0.2	0.2036950467	0.203695046637467	0.2060785766	0.2011123512
0	0	0	0	0
0.2	−0.2036950467	−0.203695046644449	−0.2060785792	−0.2011123512
0.4	−0.4364916521	−0.436491652086817	−0.4408197105	−0.5517536048
0.6	−0.6992244760	−0.699224476135717	−0.7058893915	−0.7958729497
0.8	−0.8178894222	−0.817889422276190	−0.8251948775	−0.9384253169
1	0	0	0	0

Table 7. Comparison of calculated temperature profile when $M_{\mathrm{n}} = 1$, $S_{\mathrm{c}} = 0.5$, $R_0 = 20$, $E_{\mathrm{c}} = 0.2$, $N_{\mathrm{r}} = 1$, $P_{\mathrm{r}} = 0.7$, $\lambda_3 = 0.3$, $\lambda_2 = 0.2$, $\lambda_1 = 2$.

ξ	$\theta(\xi)$			
	HAN-method	**Runge-Kutta**	**Modified-AGM**	**Reference [1]**
−1	1	1	1	1
−0.8	0.8644173236	0.864417323523375	0.8670757642	0.8445318720
−0.6	0.7471395989	0.747139598839239	0.7504287808	0.7380952670
−0.4	0.6599330100	0.659933009990955	0.6633381810	0.6906250417
−0.2	0.5927307074	0.592730707383331	0.5961589877	0.6677569106

Table 7. (*Continued*).

ξ	(ξ)			
	HAN-method	**Runge-Kutta**	**Modified-AGM**	**Reference [1]**
0	0.5346321138	0.534632113764447	0.5379531010	0.6479362174
0.2	0.4765157947	0.476515794697461	0.4796946339	0.6294637420
0.4	0.4089644934	0.408964493290973	0.4118337130	0.6089844773
0.6	0.3192846545	0.319284654492353	0.3215882740	0.5529253049
0.8	0.1891293340	0.189129334005668	0.1904390477	0.3833875003
1	0	0	0	0

Table 8. Comparison of calculated concentration profile when $M_{\mathrm{n}} = 1$, $S_{\mathrm{c}} = 0.5$, $R_0 = 20$, $E_{\mathrm{c}} = 0.2$, $N_{\mathrm{r}} = 1$, $P_{\mathrm{r}} = 0.7$, $\lambda_3 = 0.3$, $\lambda_2 = 0.2$, $\lambda_1 = 2$.

ξ	$\boldsymbol{\phi}(\xi)$			
	HAN-method	**Runge-Kutta**	**Modified-AGM**	**Reference [1]**
−1	1	1	1	1
−0.8	0.9671844807	0.967184480779807	0.9698056259	0.7950729327
−0.6	0.9148033879	0.914803387876689	0.9178916174	0.6630816895
−0.4	0.8233750858	0.823375085853292	0.8260311037	0.5869060115
−0.2	0.6809359727	0.680935972701367	0.6825521057	0.5367816909
0	0.5000000000	0.499999999998872	0.4999999981	0.4985400090
0.2	0.3190640273	0.319064027300319	0.3174478910	0.4613553214
0.4	0.1766249142	0.176624914147266	0.1739688940	0.4136371083
0.6	0.0851966121	0.085196612123571	0.0821083813	0.3382232049
0.8	0.0328155193	0.032815519220295	0.0301943736	0.2019506869
1	0	0	0	0

Table 9. Comparison of Nusselt number (N_{u}), wall couple stress (C_{g}), and skin friction coefficient (C_{f}) calculated for upper and lower disks when $M_{\mathrm{n}} = 1$, $S_{\mathrm{c}} = 0.5$, $R_0 = 20$, $E_{\mathrm{c}} = 0.2$, $N_{\mathrm{r}} = 1$, $P_{\mathrm{r}} = 0.7$, $\lambda_3 = 0.3$, $\lambda_2 = 0.2$, $\lambda_1 = 2$ with different methods.

	HAN-method	**Runge-Kutta**	**Modified-AGM**
$N_{\mathrm{u}}(+1)$	1.098568314	1.09672856185007	1.102781042
$N_{\mathrm{u}}(-1)$	0.6204230168	0.630651895876009	0.6148246058
$C_{\mathrm{g}}(+1)$	1.412252920	1.335598593	1.339031852
$C_{\mathrm{g}}(-1)$	1.412252922	1.335598593	1.339031858
$C_{\mathrm{f}}(+1)$	13.88488130	13.89622017	13.82379755
$C_{\mathrm{f}}(-1)$	−13.88488130	−13.89622017	−13.82379756

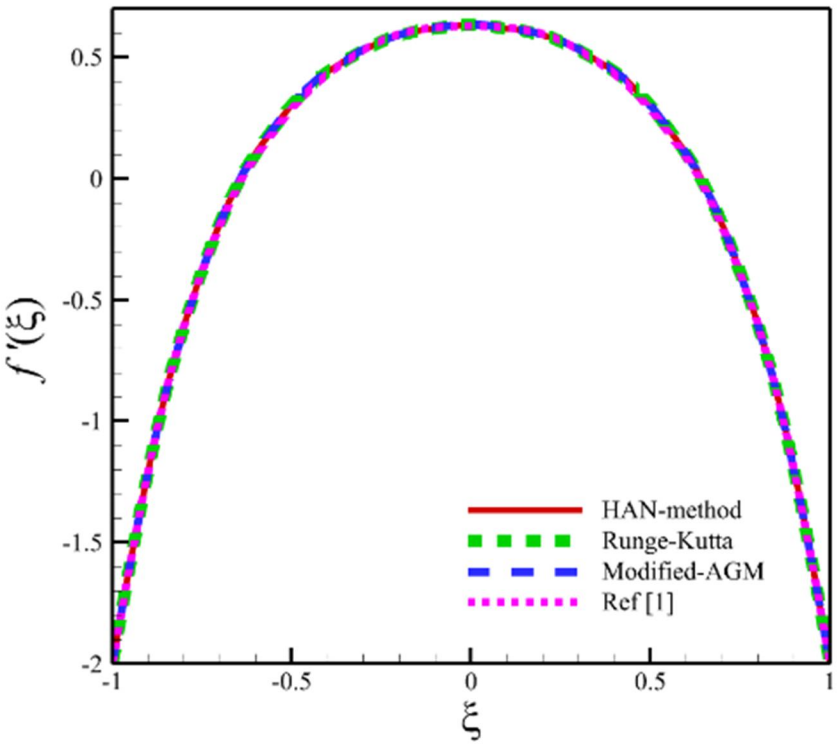

Figure 4. Comparison of calculated radial velocity when $M_{\mathrm{n}} = 1$, $S_{\mathrm{c}} = 0.5$, $R_0 = 20$, $E_{\mathrm{c}} = 0.2$, $N_{\mathrm{r}} = 1$, $P_{\mathrm{r}} = 0.7$, $\lambda_3 = 0.3$, $\lambda_2 = 0.2$, $\lambda_1 = 2$.

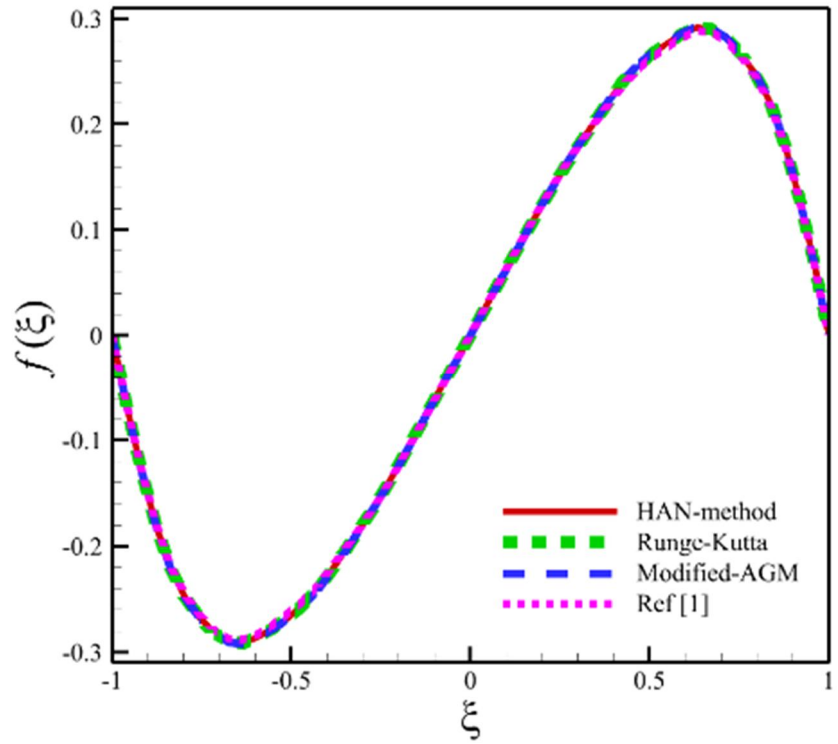

Figure 5. Comparison of calculated axial velocity when $M_n = 1$, $S_{\mathrm{c}} = 0.5$, $R_0 = 20$, $E_{\mathrm{c}} = 0.2$, $N_{\mathrm{r}} = 1$, $P_{\mathrm{r}} = 0.7$, $\lambda_3 = 0.3$, $\lambda_2 = 0.2$, $\lambda_1 = 2$.

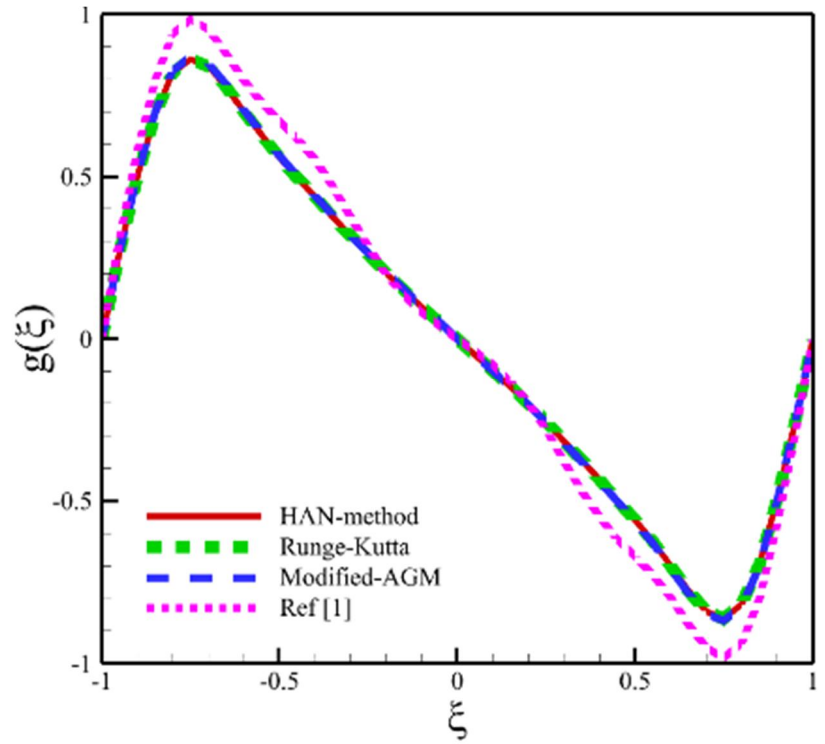

Figure 6. Comparison of calculated micro-rotation profile when $M_{\mathrm{n}} = 1$, $S_{\mathrm{c}} = 0.5$, $R_0 = 20$, $E_{\mathrm{c}} = 0.2$, $N_{\mathrm{r}} = 1$, $P_{\mathrm{r}} = 0.7$, $\lambda_3 = 0.3$, $\lambda_2 = 0.2$, $\lambda_1 = 2$.

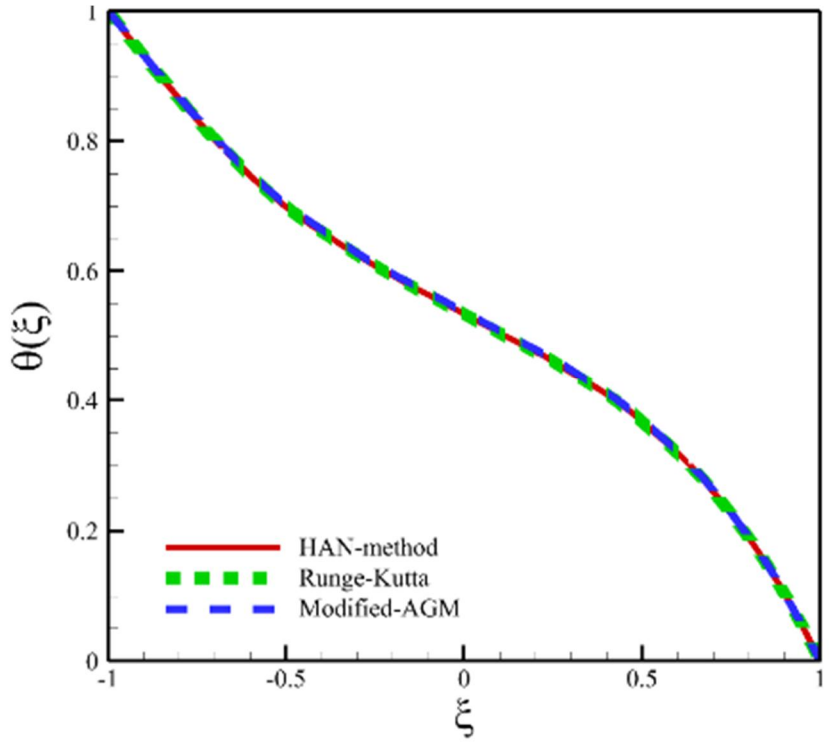

Figure 7. Comparison of calculated temperature profile when $M_{\mathrm{n}} = 1$, $S_{\mathrm{c}} = 0.5$, $R_0 = 20$, $E_{\mathrm{c}} = 0.2$, $N_{\mathrm{r}} = 1$, $P_{\mathrm{r}} = 0.7$, $\lambda_3 = 0.3$, $\lambda_2 = 0.2$, $\lambda_1 = 2$.

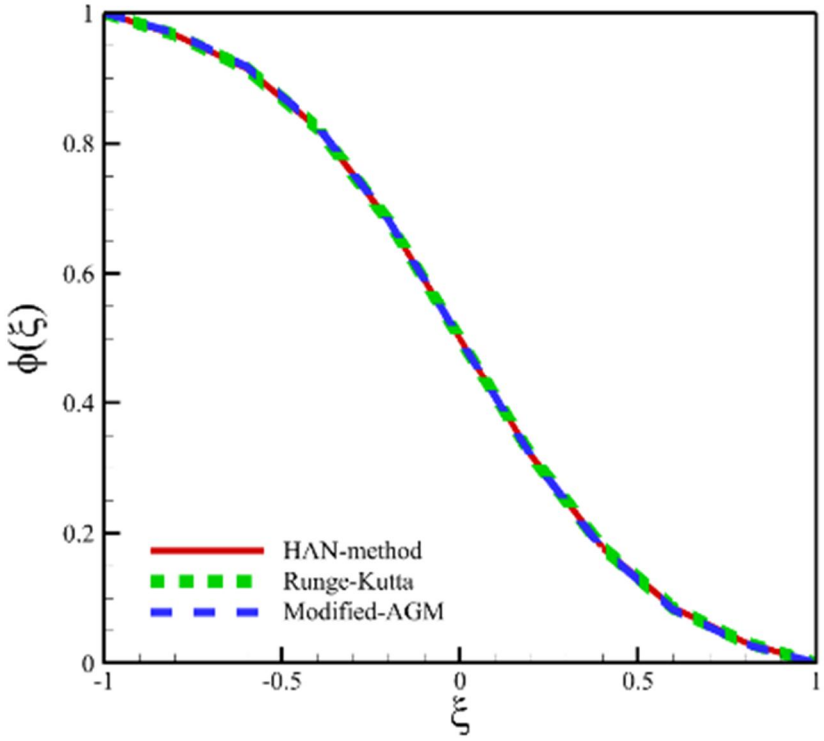

Figure 8. Comparison of calculated concentration profile when $M_{\mathrm{n}} = 1$, $S_{\mathrm{c}} = 0.5$, $R_0 = 20$, $E_{\mathrm{c}} = 0.2$, $N_{\mathrm{r}} = 1$, $P_{\mathrm{r}} = 0.7$, $\lambda_3 = 0.3$, $\lambda_2 = 0.2$, $\lambda_1 = 2$.

4. Results and discussions

After proving the correctness of the results of the two methods used in this research compared to the previous studies, the effect of changes in the physical parameters of Equations (12)–(15) is expressed on the axial, radial, concentration, temperature, and microrotation profiles. The effect of changing each of the parameters has been done separately. So, the effects of changes in parameters such as micropolar parameters, stretching Reynolds number, magnetic parameter, radiation parameter, Prandtl number, Eckert number, and Schmidt number on axial, radial, microrotation, temperature, and concentration profiles have been investigated, respectively.

Now, the results of examining the axial, radial, microrotation, temperature, and concentration contours for Equations (12)–(15) when the micropolar parameters λ_1, λ_2, and λ_3 are changed according to **Table 10**:

Table 10. Micropolar parameters in different cases.

Case number	λ_1	λ_2	λ_3
1	0	0	0
2	2	0.2	0.3
3	4	0.4	0.5
4	6	0.6	0.7
5	8	0.8	0.9
6	10	1.0	1.1

When the micropolar parameters were changed, other parameters were also constant and were equal to the values of $M_{\mathrm{n}} = 1, S_{\mathrm{c}} = 0.5, R_0 = 20, E_{\mathrm{c}} = 0.2, N_{\mathrm{r}} = 1$ and $P_{\mathrm{r}} = 0.7$. According to **Table 10**, the micropolar parameters were investigated in 6 different cases. The changes in these parameters affected all five quantities of axial velocity, radial velocity, microrotation, temperature, and concentration, as well as the 2D and 3D contours obtained from these changes, which are also shown in **Figures 9–18**. According to **Figures 9** and **10**, the axial velocity's maximum positive and negative values occur in case 6 and are equal to 0.367154015354 and −0.367154015355, respectively. The maximum positive axial velocity occurs when the value of ξ is equal to 0.591836734687163912, and the maximum negative value of the axial velocity occurs when the value of ξ is equal to −0.591836734773761197. According to **Figures 9** and **10**, the lowest value of the axial velocity is zero in all the cases in **Table 10** and exactly at three points of the upper disc ($\xi = 1$) lower disc ($\xi = -1$) and occurs between two disks ($\xi = 0$). According to **Figures 11** and **12**, the maximum positive value of the radial velocity occurs in case 6 and has a value of 0.911191371136 and occurs in a place where the value of ξ is equal to −0.0204081632659887449. The maximum negative value of the radial velocity occurs on both disks and in all cases and has the value of -2. The minimum value of radial velocity calculated in all 6 cases is zero. Still, it happens in different places, which means that the place of minimum radial velocity is different in each case. According to **Table 10**, the minimum radial velocity in the first case occurs at $\xi = \pm 0.714783795486643614$, in the second case, at $\xi = \pm 0.640084929206338415$, in the third case, at $\xi = \pm 0.615927887799965768$, in the fourth case, at $\xi = \pm 0.603995651475552564$, in the fifth case, at $\xi = \pm 0.597038661803401371$, and in the sixth case, at $\xi = \pm\, 0.592472823036015117$. According to **Figures 13** and **14**, the maximum positive and negative values of microrotation occur in case 6 and are equal to 1.0699638786 and −1.0699638786, respectively. The maximum positive value of microrotation occurs when the value of ξ is equal to −0.71428571430603871, and the maximum negative value of microrotation occurs when the value of ξ is equal to 0.714285713365754971. According to **Figures 13** and **14**, the lowest amount of microrotation is zero in all the cases in **Table 10** and exactly occurs at three locations of the upper disk ($\xi = 1$), the lower disk ($\xi = -1$) and between two disks ($\xi = 0$). According to **Figures 15–18**, the maximum temperature and concentration equal 1. In all the cases in **Table 10**, they occur when the value of ξ is equal to −1, and the minimum temperature and concentration are equal to −1, and they occur in all the cases in **Table 10** when the value of ξ is equal to 1.

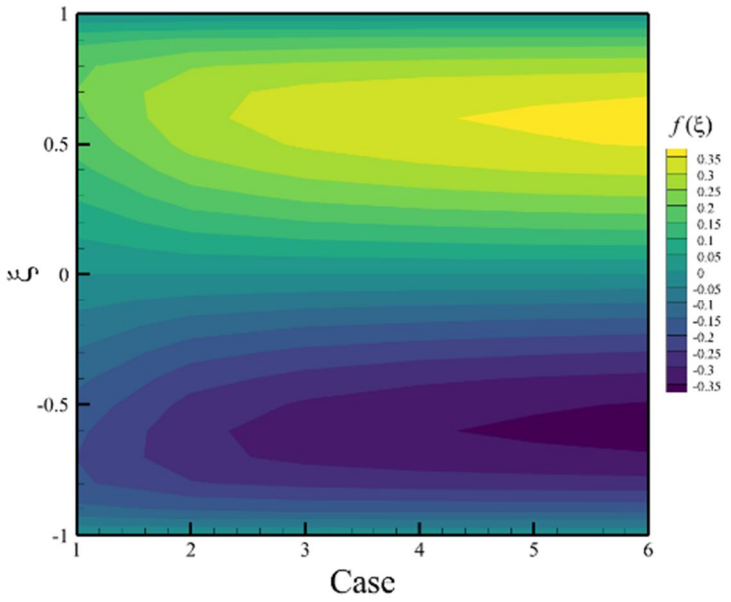

Figure 9. Two-dimensional contour of axial velocity in different cases of micropolar parameters.

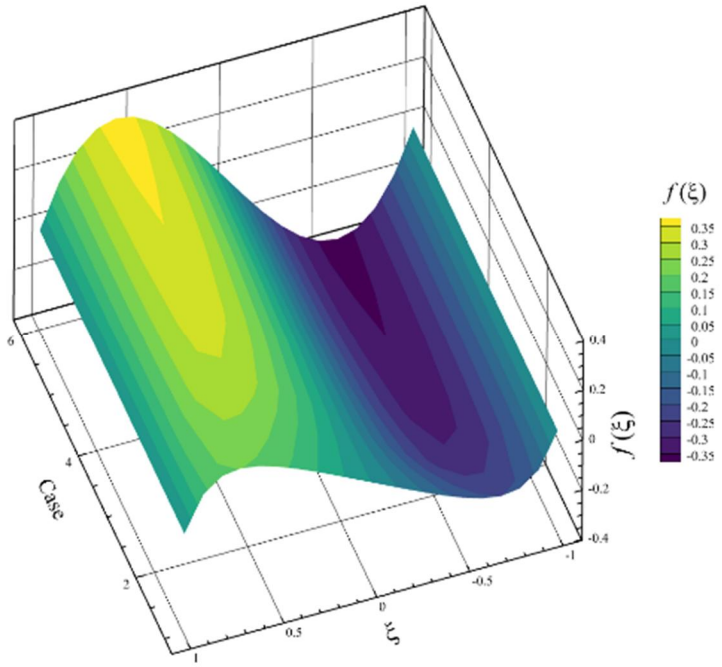

Figure 10. Three-dimensional contour of axial velocity in different cases of micropolar parameters.

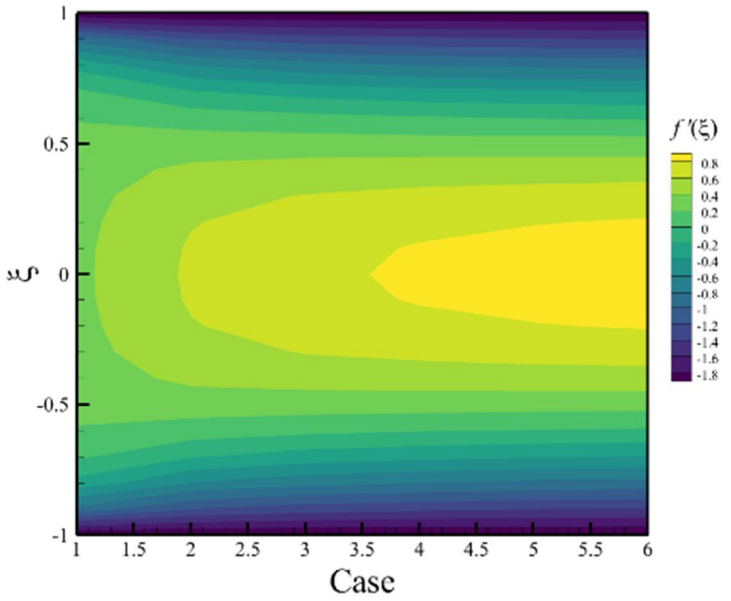

Figure 11. Two-dimensional contour of radial velocity in different cases of micropolar parameters.

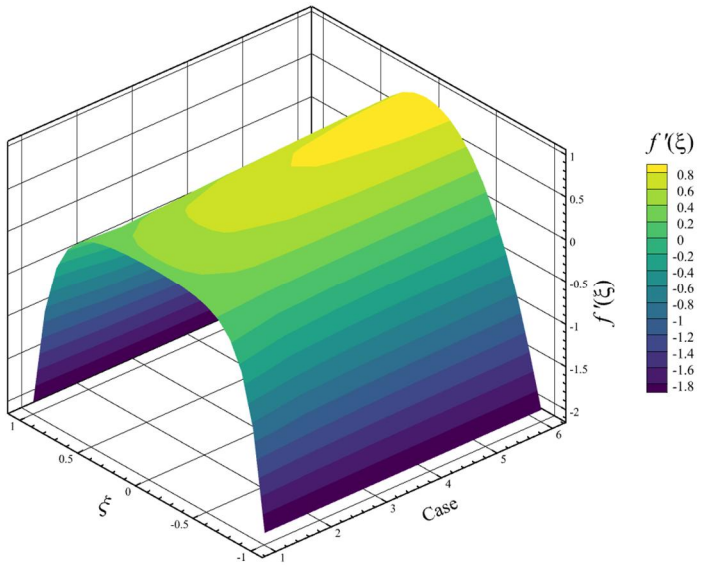

Figure 12. Three-dimensional contour of radial velocity in different cases of micropolar parameters.

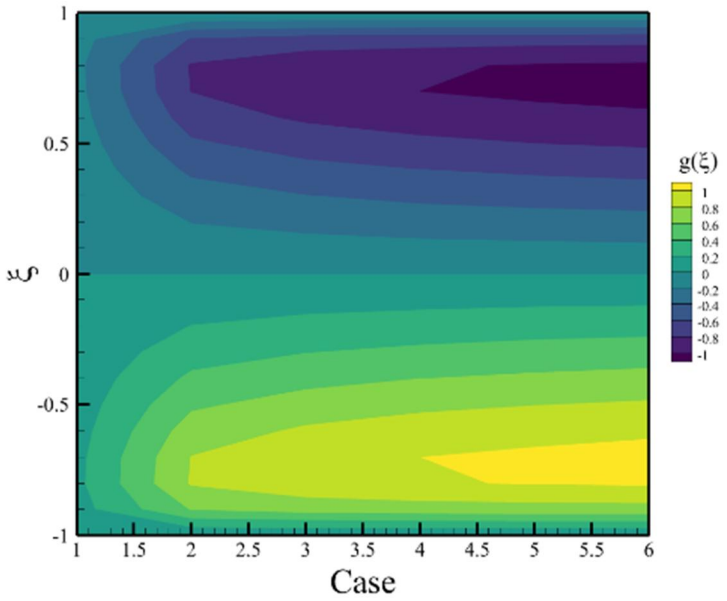

Figure 13. Two-dimensional contour of microrotation in different cases of micropolar parameters.

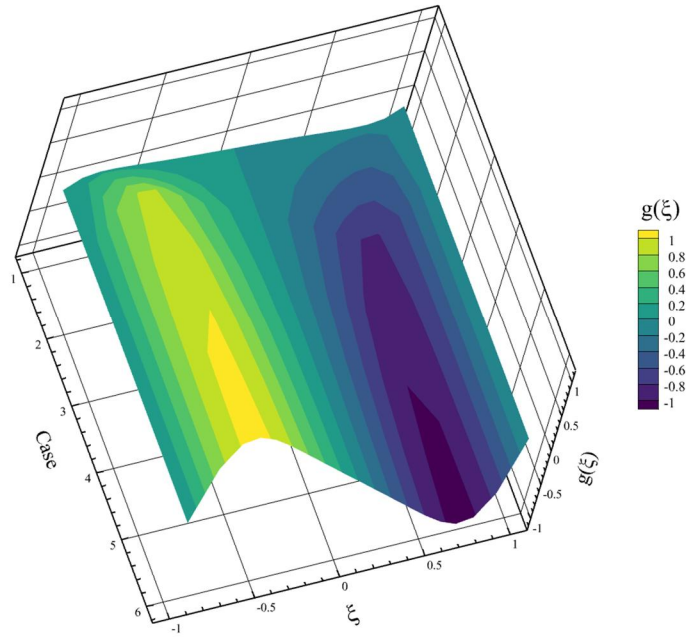

Figure 14. Three-dimensional contour of microrotation in different cases of micropolar parameters.

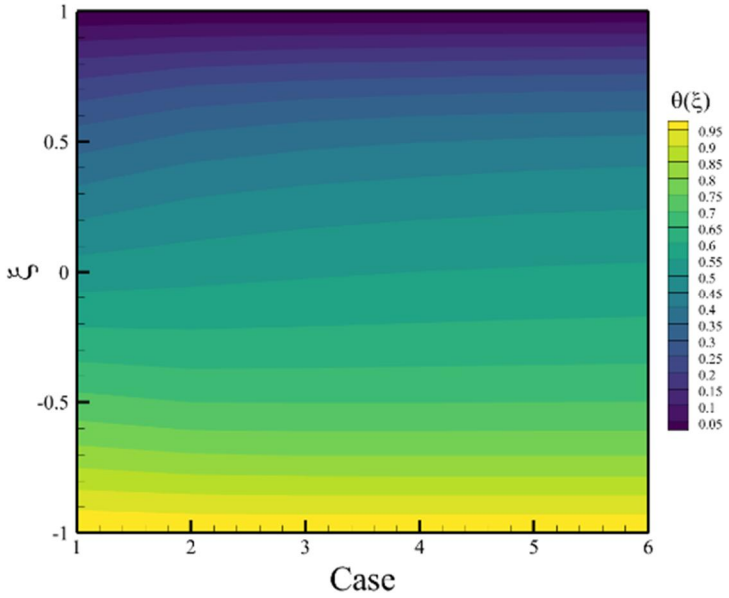

Figure 15. Two-dimensional contour of temperature in different cases of micropolar parameters.

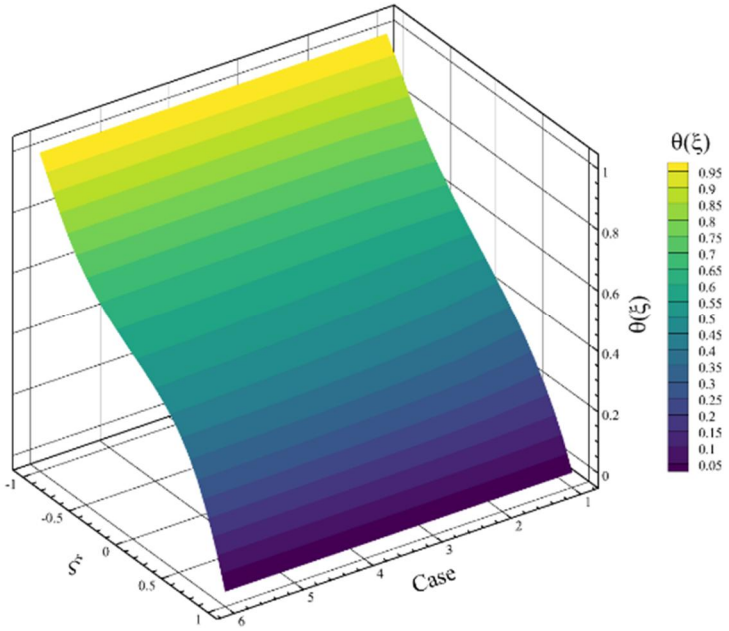

Figure 16. Three-dimensional contour of temperature in different cases of micropolar parameters.

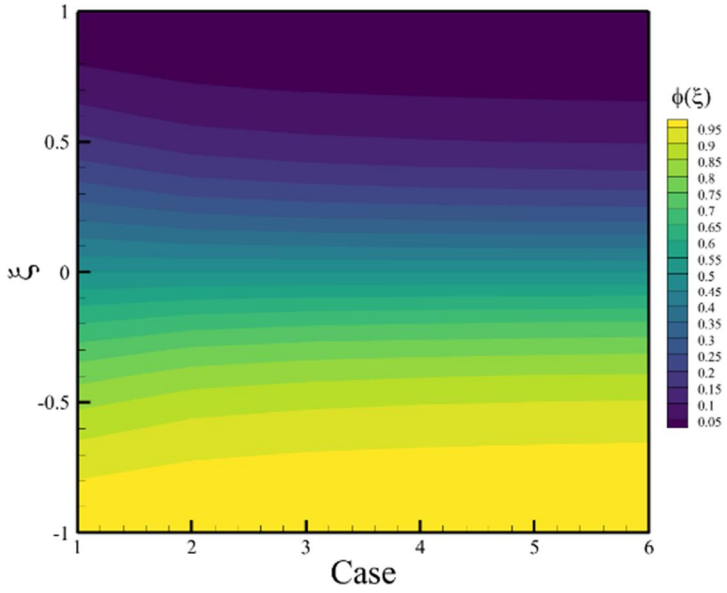

Figure 17. Two-dimensional contour of concentration in different cases of micropolar parameters.

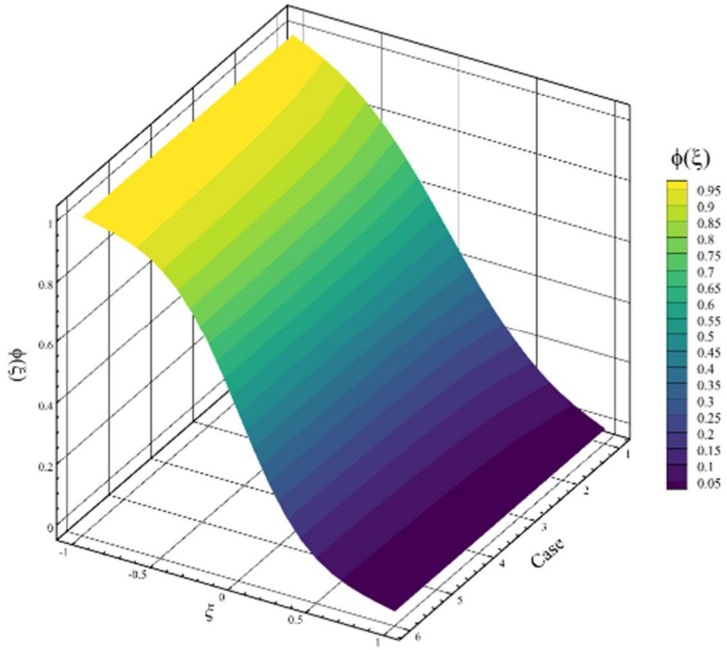

Figure 18. Three-dimensional contour of concentration in different cases of micropolar parameters.

Now, the results of the investigation of axial, radial, microrotation, temperature, and concentration contours for Equations (12)–(15), when the stretching Reynolds number was changed are discussed. When the stretching Reynolds number parameter was changed, the other parameters were constant and equal to the values of $M_{\mathrm{n}} = 1$, $S_{\mathrm{c}} = 0.5$, $E_{\mathrm{c}} = 0.2$, $N_{\mathrm{r}} = 1$, $P_{\mathrm{r}} = 0.7$, $\lambda_3 = 0.3$, $\lambda_2 = 0.2$, $\lambda_1 = 2$. The stretching Reynolds number parameter was investigated in 6 different cases. Changes in this parameter affected all five quantities of axial velocity, radial velocity, microrotation, temperature, and concentration, and the two-dimensional and three-dimensional

contours resulting from these changes are also shown in **Figures 19–28**. According to **Figures 19** and **20**, the maximum positive and negative values of the axial velocity occurred when the value of the stretching Reynolds number was zero, 0.408437042705, and −0.408437042704, respectively. The maximum positive axial velocity occurs when the value of ξ is equal to 0.551020408126658312, and the maximum negative value of axial velocity occurs when the value of ξ is equal to −0.551020408397712713. According to **Figures 19** and **20**, the lowest value of the axial velocity is zero for each value of the stretching Reynolds number and happens exactly at the three points of the upper disc ($\xi = 1$), the lower disc ($\xi = -1$), and between the two discs ($\xi = 0$). According to **Figures 21** and **22**, the maximum positive value of the radial velocity occurs when the stretching Reynolds number is zero and has a value of 1.08743936914 and occurs at a point where the value of ξ is equal to −0.0050251256627916636 4. The maximum negative value of the radial velocity occurs on both disks and for each stretching Reynolds number, with a value of −2. The minimum calculated value of the radial velocity in every six stretching Reynolds numbers is assumed to be zero. Still, it happens in different places, which means that the location of the minimum radial velocity is different in every stretching Reynolds number. When the stretching Reynolds number is zero, the minimum radial velocity occurs at $\xi = \pm 0.567681247229664065$. When the stretching Reynolds number is assumed to be 10, the minimum radial velocity occurs at $\xi = \pm 0.608076355132214585$. When the stretching Reynolds number is assumed to be 20, the minimum radial velocity occurs at $\xi = \pm 0.640511670826334534$. When the stretching Reynolds number is assumed to be 30, the minimum radial velocity occurs at $\xi = \pm 0.665380422273169736$. When the stretching Reynolds number is assumed to be 50, the minimum radial velocity occurs at $\xi = \pm 0.703310792645532423$. According to **Figures 23** and **24**, the maximum positive and negative values of microrotation in the case that the stretching Reynolds number is assumed to be zero and are equal to 1.18125112872 and −1.18125112871, respectively. The maximum positive value of microrotation occurs when the value of ξ is equal to −0.628140703544759815, and the maximum negative value of microrotation occurs when the value of ξ is equal to 0.62814070251133014. According to **Figures 23** and **24**, the minimum amount of microrotation is zero for all assumed stretching Reynolds numbers. It is exactly at three points of the upper disk ($\xi = 1$), the lower disk ($\xi = -1$), and between the two disks ($\xi = 0$) that is happens. According to **Figures 25–28**, the maximum temperature and concentration are equal to 1. All assumed stretching Reynolds numbers occur when the value of ξ is equal to −1. The minimum temperature and concentration are equal to −1, and for all the assumed stretching, Reynolds numbers occur when the value of ξ is equal to 1.

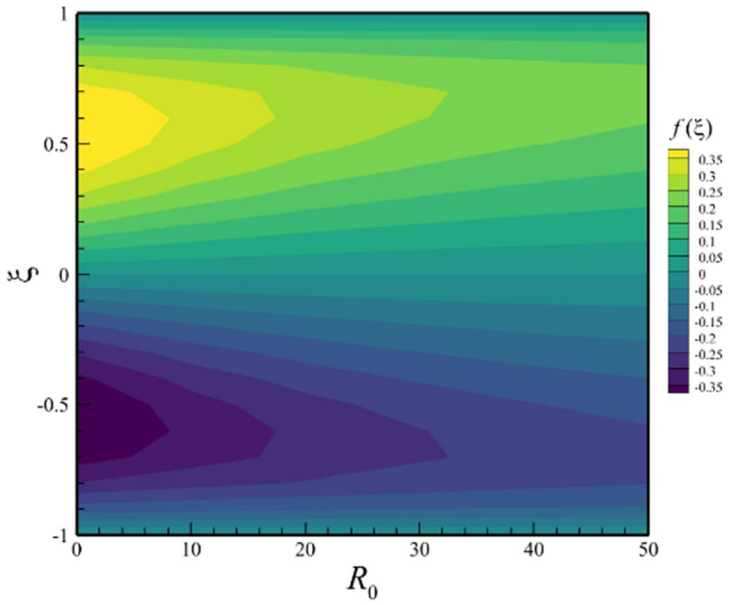

Figure 19. Two-dimensional contour of axial velocity at different values of the stretching Reynolds number.

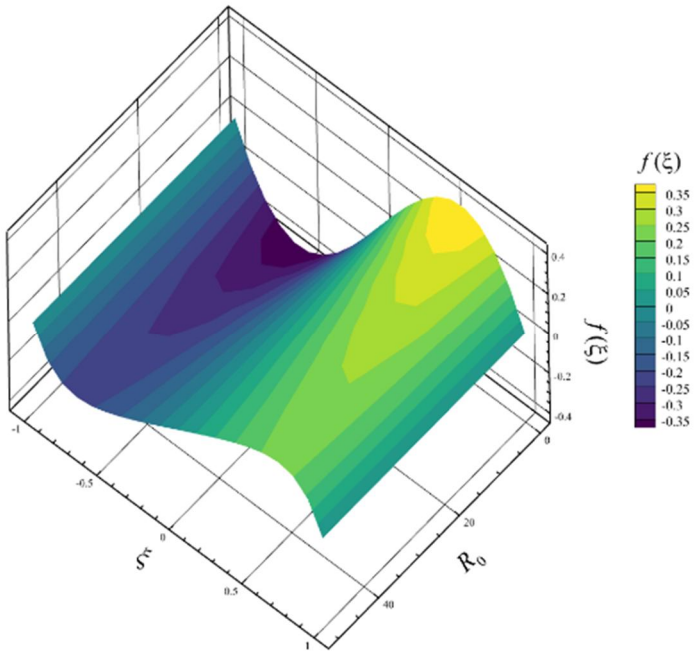

Figure 20. Three-dimensional contour of axial velocity at different values of the stretching Reynolds number.

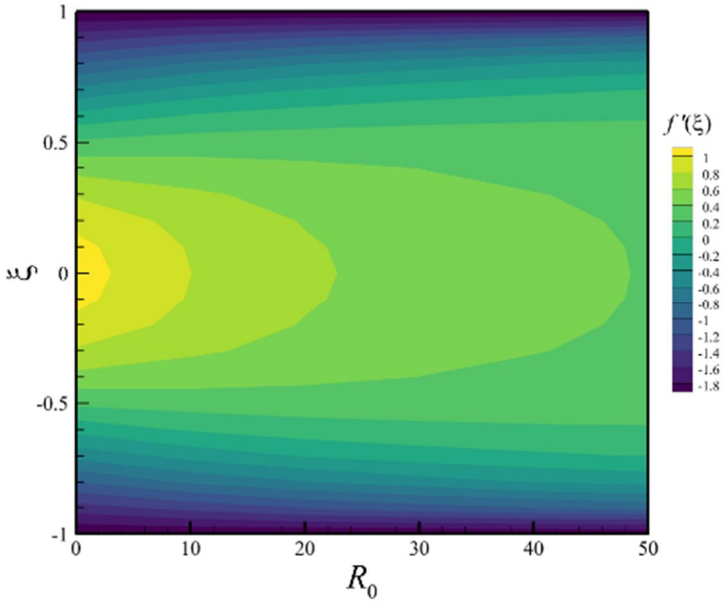

Figure 21. Two-dimensional contour of radial velocity at different values of the stretching Reynolds number.

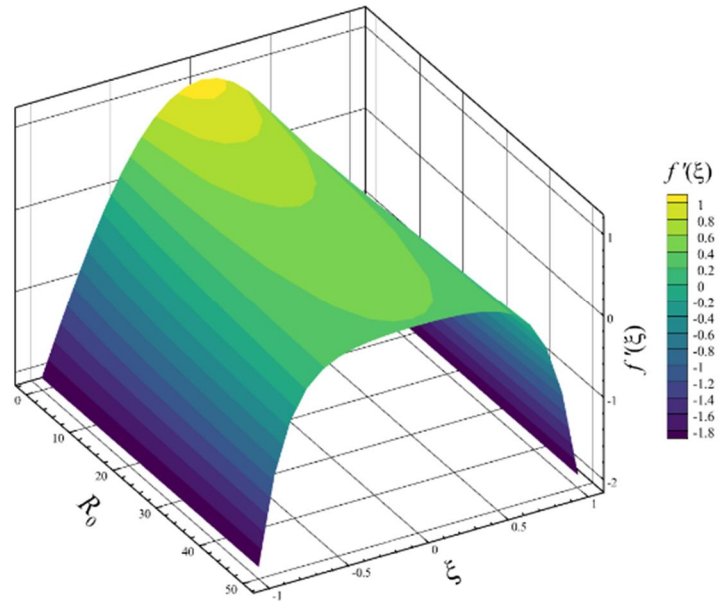

Figure 22. Three-dimensional contour of radial velocity at different values of the stretching Reynolds number.

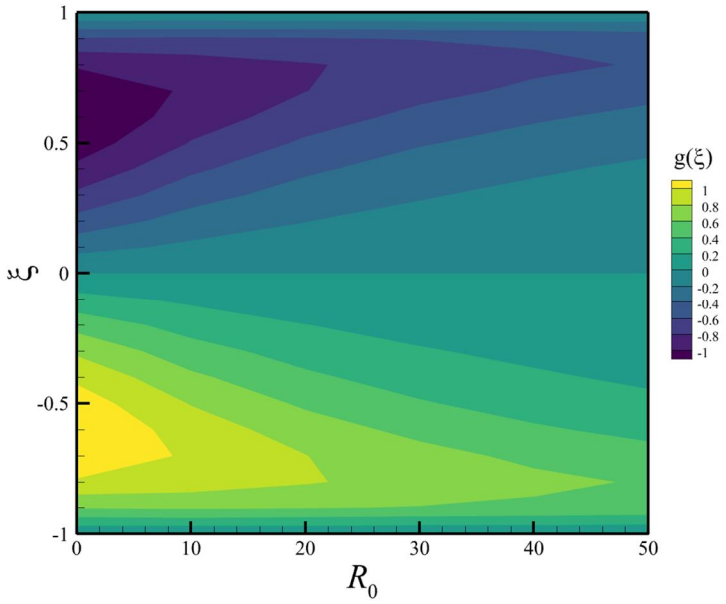

Figure 23. Two-dimensional contour of microrotation at different values of the stretching Reynolds number.

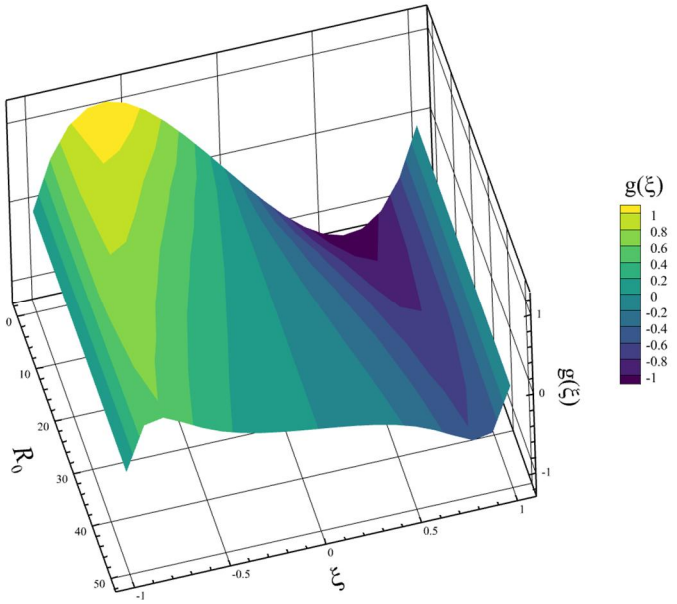

Figure 24. Three-dimensional contour of microrotation at different values of the stretching Reynolds number.

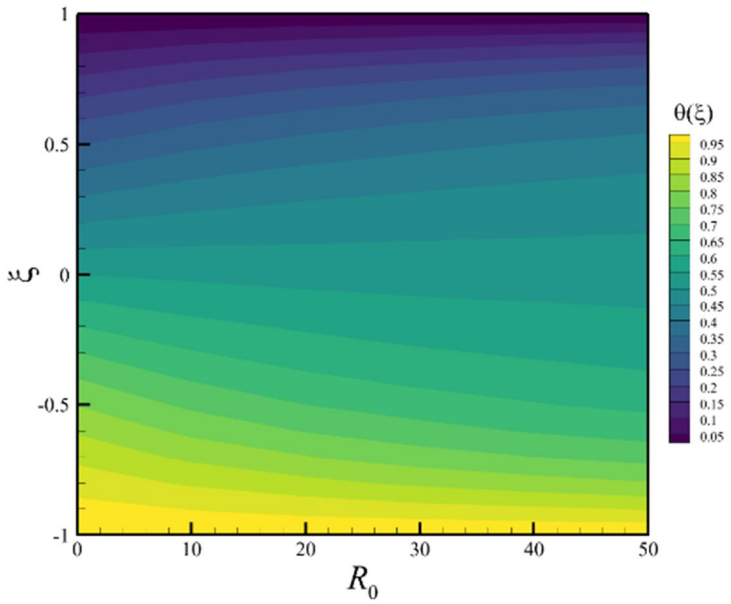

Figure 25. Two-dimensional contour of temperature at different values of the stretching Reynolds number.

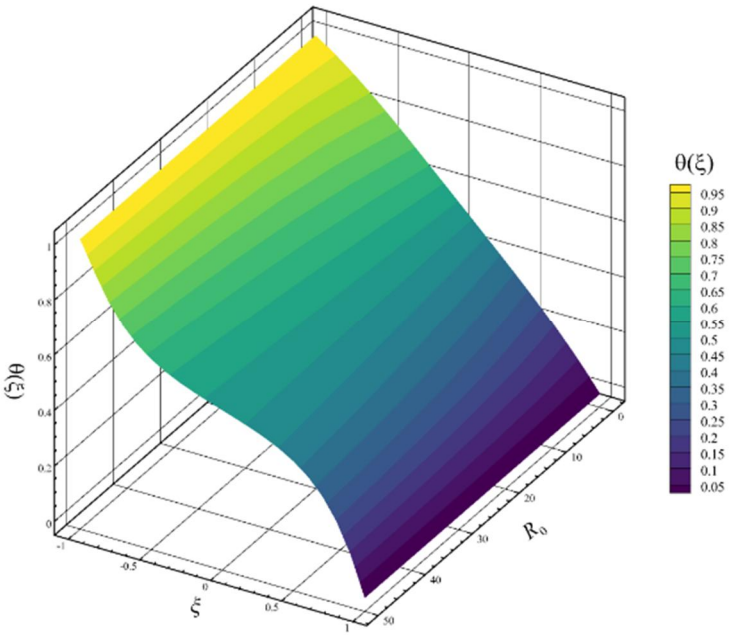

Figure 26. Three-dimensional contour of temperature at different values of the stretching Reynolds number.

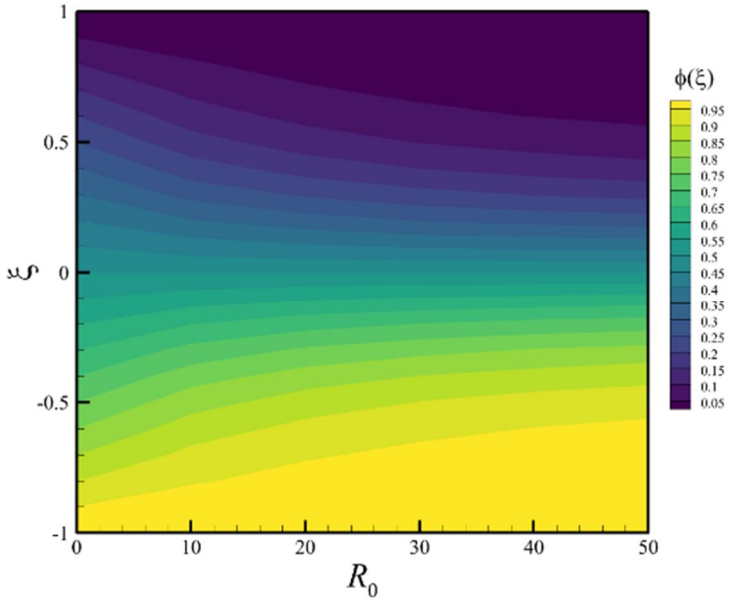

Figure 27. Two-dimensional contour of concentration at different values of the stretching Reynolds number.

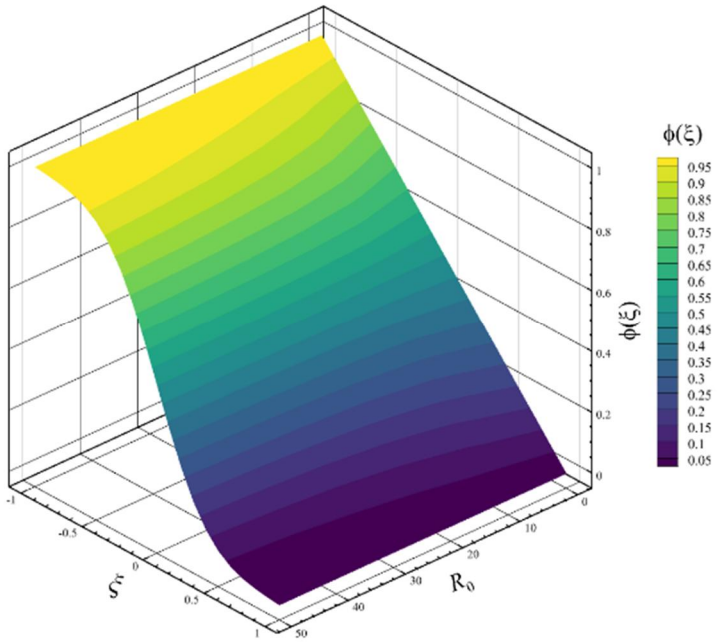

Figure 28. Three-dimensional contour of concentration at different values of stretching Reynolds number.

Now, the results of the investigation of axial, radial, microrotation, temperature, and concentration contours for Equations (12)–(15) when the magnetic parameter was changed are discussed. When the magnetic parameter was changed, the other parameters were constant and equal to the values of $S_c = 0.5$, $R_0 = 20$, $E_c = 0.3$, $N_r = 1$, $P_r = 2$, $\lambda_3 = 0.3$, $\lambda_2 = 0.2$, and $\lambda_1 = 2$. The magnetic parameter was investigated in 6 different cases, and the changes of this parameter affected all five quantities of axial velocity, radial velocity, microrotation, temperature, and concentration, and two-dimensional and three-dimensional contours resulting from these changes are also shown in **Figures 29–38**. According to **Figures 29** and **30**, the

maximum positive and negative values of the axial velocity occurred when the value of the magnetic parameter was zero and were equal to 0.340651700237 and −0.340651700186, respectively. The maximum positive axial velocity occurs when the value of ξ is equal to 0.608040200808000031, and the maximum negative value of the axial velocity occurs when the value of ξ is equal to −0.608040201544712167. According to **Figures 29** and **30**, the lowest value of the axial velocity is zero for each value of the magnetic parameter and exactly happens at the three points of the upper disc ($\xi = 1$), the lower disc ($\xi = -1$), and between the two discs ($\xi = 0$). According to **Figures 31** and **32**, the maximum positive value of the radial velocity occurs when the magnetic parameter is zero and has a value of 0.813292009152 and occurs in a place where the value of ξ is equal to −0.0050251269820265984 8. The maximum negative value of the radial velocity occurs on both disks and for each magnetic parameter and has a value of −2. The minimum value of radial velocity calculated in all six magnetic parameters is assumed to be zero, but it happens in different places; that is, the location of minimum radial velocity is different in each magnetic parameter. According to **Figures 31** and **32**, in the case where the value of the magnetic parameter is zero, the minimum radial velocity occurs at $\xi = \pm 0.607429531034752723$. When the magnetic parameter is assumed to equal 0.5, the minimum radial velocity occurs at $\xi = \pm 0.616804860051527681$. When the magnetic parameter is assumed to equal 1, the minimum radial velocity occurs at $\xi = \pm 0.640511670824125412$. When the magnetic parameter is assumed to be equal to 1.5, the minimum radial velocity occurs at $\xi = \pm 0.669338517525361443$. In the case where the value of the magnetic parameter is assumed to equal 2, the minimum radial velocity occurs at $\xi = \pm 0.698644720773267114$. When the magnetic parameter is assumed to equal 2.5, the minimum radial velocity occurs at $\xi = \pm 0.724515125952562067$. According to **Figures 33** and **34**, the maximum positive and negative values of microrotation in the case where the magnetic parameter is assumed to be zero are 0.920228094121 and −0.920228094294, respectively. The maximum positive value of microrotation occurs when $\xi = -0.72864321608434357$, and the maximum negative value of microrotation occurs when $\xi = 0.728643208751884042$. According to **Figures 33** and **34**, the minimum amount of microrotation is zero for all the assumed magnetic parameters. It is exactly at three points of the upper disk ($\xi = 1$) and the lower disk ($\xi = -1$) and occurs between two disks ($\xi = 0$). According to **Figures 35–38**, the maximum temperature and concentration equal 1. For all assumed magnetic parameters, they occur when $\xi = -1$ is. The minimum temperature and concentration are equal to −1, and all the assumed magnetic parameters occur when $\xi = 1$.

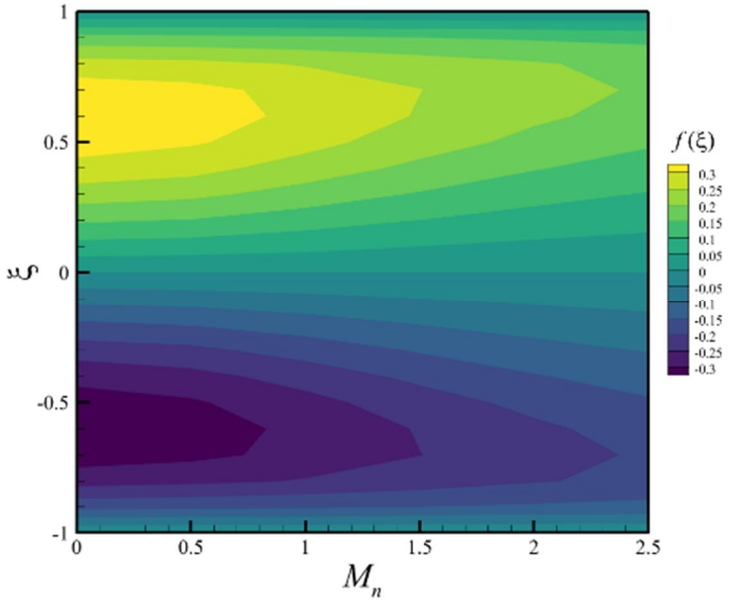

Figure 29. Two-dimensional contour of axial velocity in different values of the magnetic parameter.

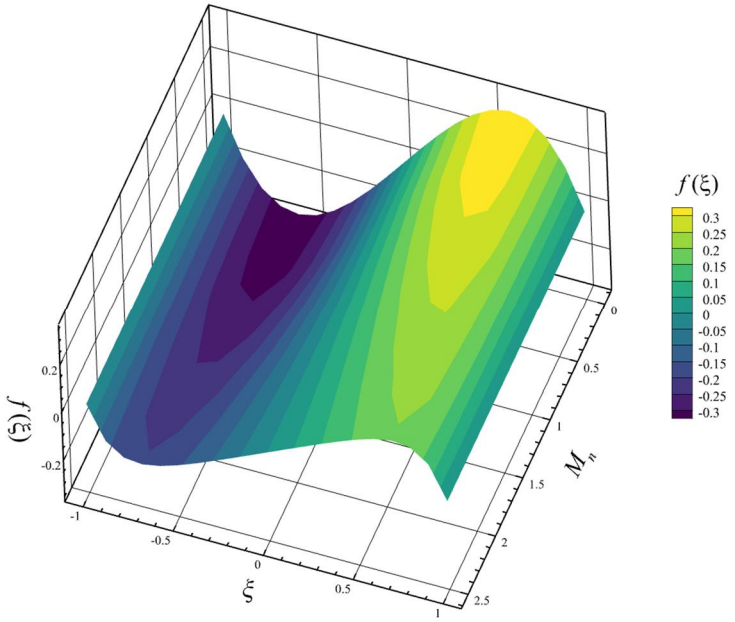

Figure 30. Three-dimensional contour of axial velocity in different values of the magnetic parameter.

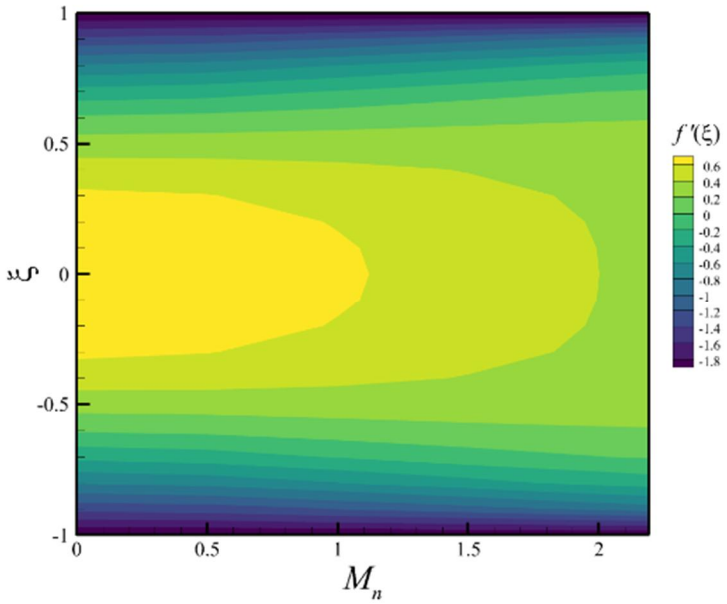

Figure 31. Two-dimensional contour of radial velocity in different values of the magnetic parameter.

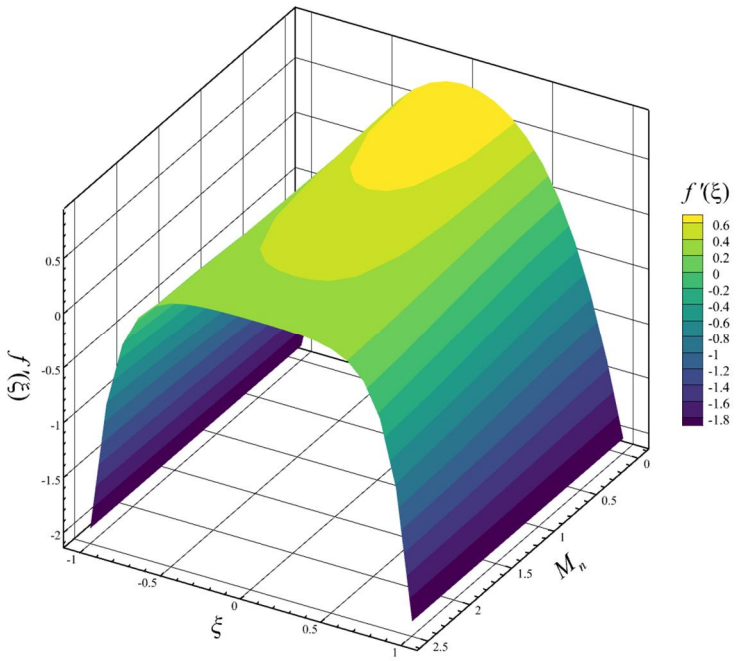

Figure 32. Three-dimensional contour of radial velocity in different values of the magnetic parameter.

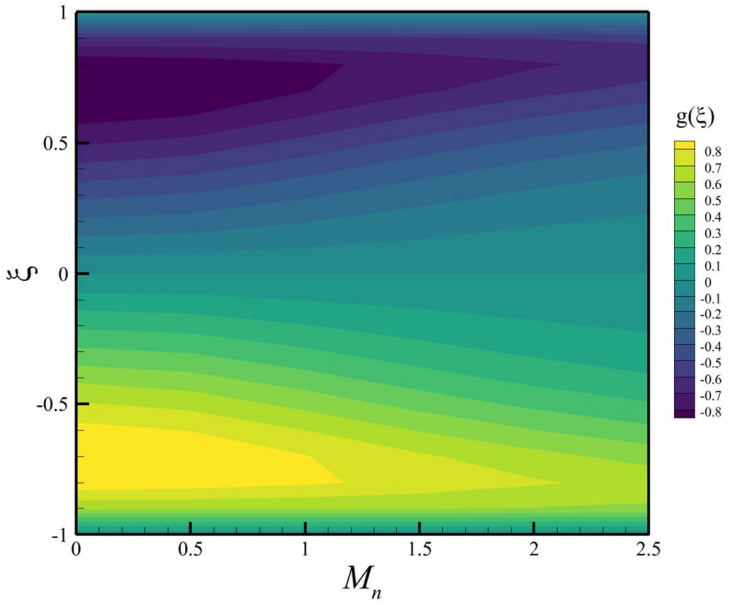

Figure 33. Two-dimensional contour of microrotation at different values of the magnetic parameter.

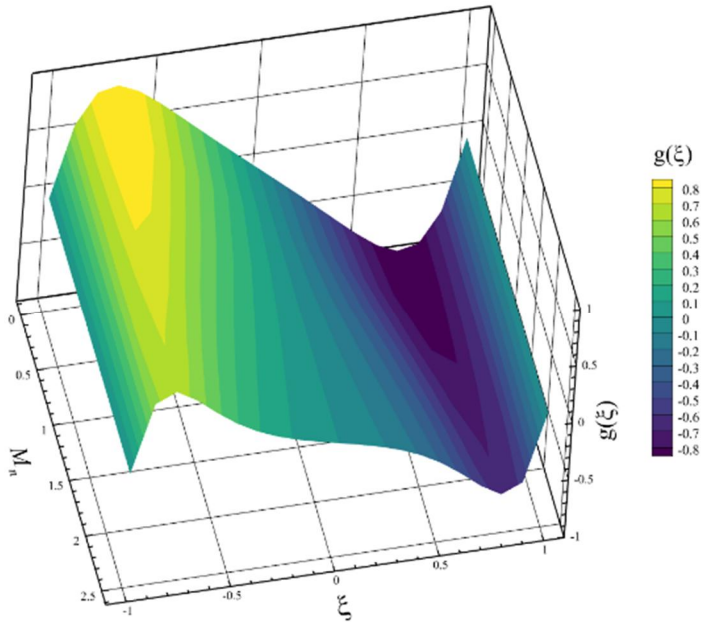

Figure 34. Three-dimensional contour of microrotation at different values of the magnetic parameter.

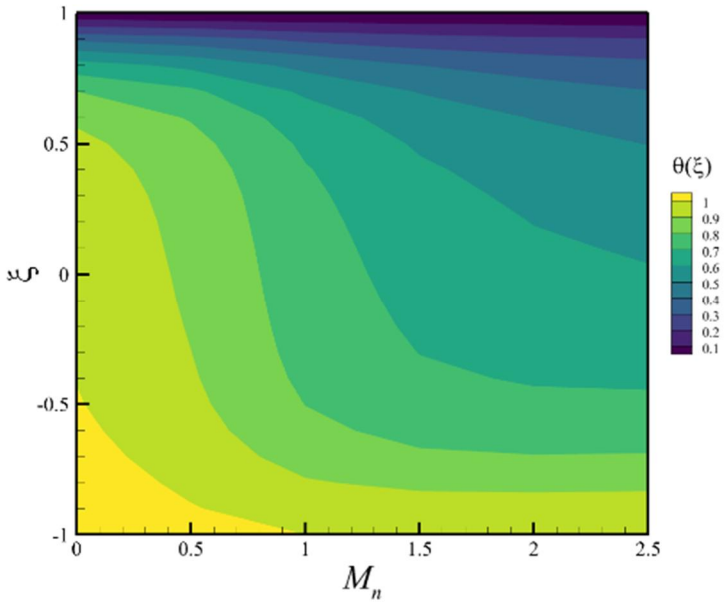

Figure 35. Two-dimensional contour of temperature at different values of the magnetic parameter.

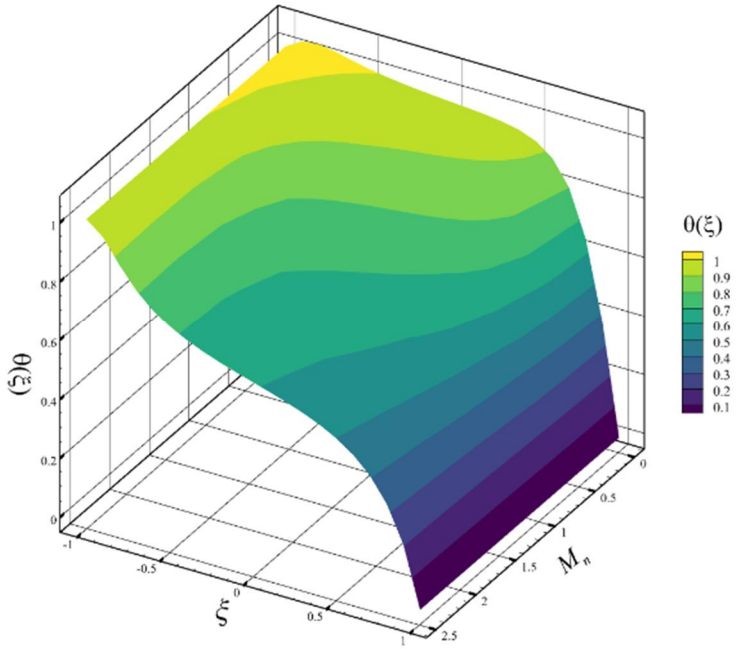

Figure 36. Three-dimensional contour of temperature in different values of the magnetic parameter.

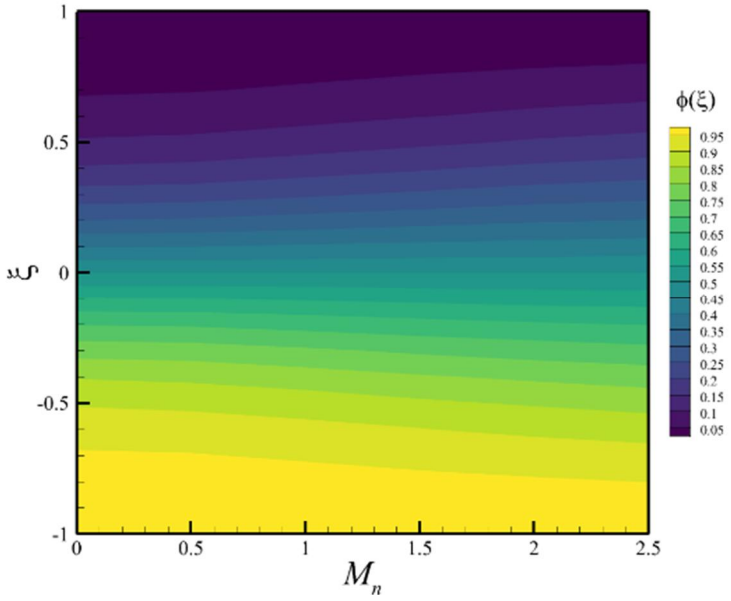

Figure 37. Two-dimensional contour of concentration in different values of the magnetic parameter.

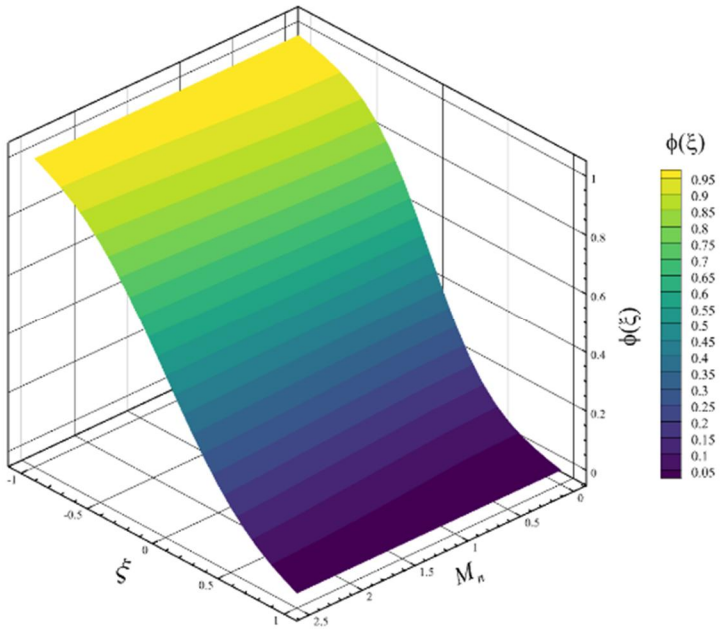

Figure 38. Three-dimensional contour of concentration in different values of the magnetic parameter.

Now, the results of the investigation of axial, radial, microrotation, temperature, and concentration contours for Equations (12)–(15) when the radiation parameter was changed are discussed. When the radiation parameter was changed, the other parameters were constant and equal to the values of $M_{\mathrm{n}} = 1$, $S_{\mathrm{c}} = 0.5$, $R_0 = 3$, $E_{\mathrm{c}} = 0.3$, $P_{\mathrm{r}} = 0.7$, $\lambda_3 = 0.3$, $\lambda_2 = 0.2$, $\lambda_1 = 2$. The radiation parameter was investigated in 6 different modes. The changes in this parameter only had a significant effect on temperature quantity. They had almost no effect on the four quantities of axial speed, radial velocity, microrotation, and concentration, and the resulting 2D and 3D temperature contours were shown in two **Figures 39** and **40**. The changes in the

radiation parameter did not affect the quantity of the axial velocity, and the maximum positive and negative values of the axial velocity occurred for all the radiation parameters and are equal to 0.383953826907 and −0.383953826907, respectively. The maximum positive axial velocity occurs when the value of ξ is equal to 0.577889446943717244, and the maximum negative value of the axial velocity occurs when the value of ξ is equal to −0.577889448510863213. The lowest value of the axial velocity is zero for all radiation parameters. It occurs exactly at three points of the upper disk ($\xi = 1$), the lower disk ($\xi = -1$), and between the two disks ($\xi = 0$). The radiation parameter changes did not affect the radial velocity quantity; the maximum positive and negative values of the radial velocity occurred for all the radiation parameters and are equal to 0.986765233308 and −2, respectively. The maximum positive radial velocity occurs when the value of ξ is equal to −0.00502512575911638962, and the maximum negative value of the radial velocity occurs when the value of ξ is equal to ±1. The lowest value of the radial velocity is zero for all radiation parameters and occurs when the value of ξ is equal to ±0.580466299484895809. The changes in radiation parameters did not affect the amount of microrotation, and the maximum positive and negative values of microrotation occurred for all radiation parameters and are equal to 1.11011447812 and −1.11011447812, respectively. The maximum positive microrotation occurs when the value of ξ is equal to −0.648241207908432315, and the maximum negative value of microrotation occurs when the value of ξ is equal to 0.648241203627465956. The lowest amount of microrotation is zero for all radiation parameters and occurs exactly at three points of the upper disk ($\xi = 1$), the lower disk ($\xi = -1$), and between the two disks ($\xi = 0$). The changes in the radiation parameter did not affect the amount of concentration. The maximum concentration is equal to 1, and all the assumed radiation parameters occur when the value of ξ is equal to −1. The minimum concentration is equal to zero. It happens for all the assumed radiation parameters when the value of ξ equals 1. According to **Figures 39** and **40**, changes in the radiation parameter only significantly affect the quantity of temperature, and for all radiation parameters, the maximum temperature is equal to 1. It is assumed for all radiation parameters that when the value of ξ is equal to −1, it happens, and the minimum temperature is equal to zero. It happens for all assumed radiation parameters when the value of ξ is equal to 1.

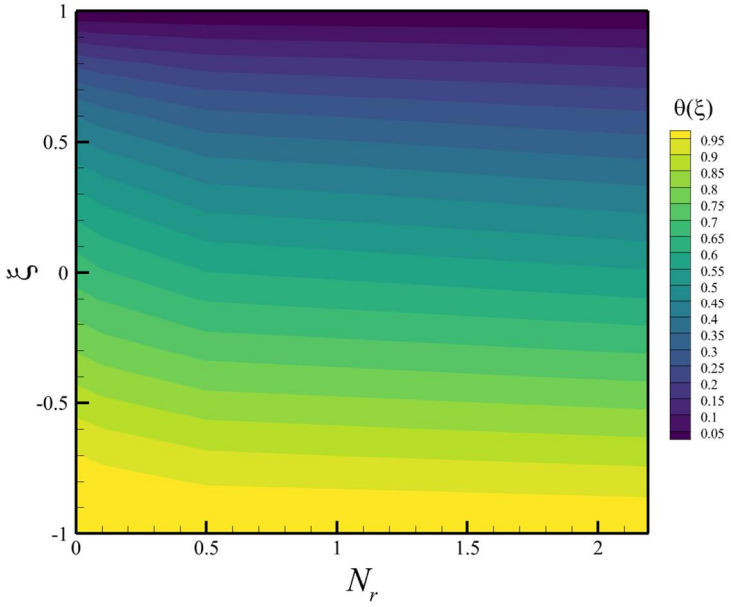

Figure 39. Two-dimensional contour of temperature in different values of radiation parameter.

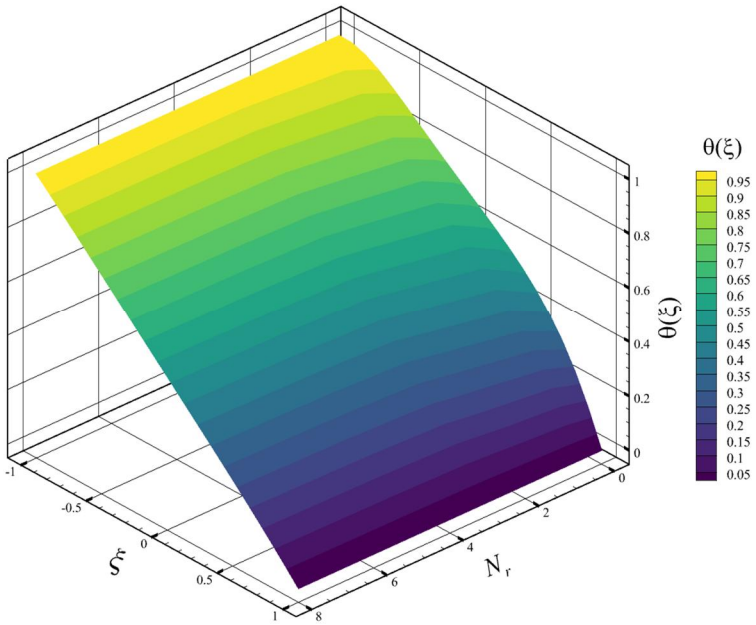

Figure 40. Three-dimensional contour of temperature in different values of radiation parameter.

Now, the results of the investigation of axial, radial, microrotation, temperature, and concentration contours for Equations (12)–(15) when the Prandtl number was changed are discussed. When the Prandtl number changed, other parameters were constant and equal to the values of $M_n = 1$, $S_c = 0.5$, $R_0 = 3$, $E_c = 0.2$, $N_r = 2$, $\lambda_3 = 0.3$, $\lambda_2 = 0.2$, $\lambda_1 = 2$. The Prandtl number was investigated in 6 different cases, and the changes of this parameter had a significant effect only on the quantity of temperature and the four quantities of axial velocity, radial velocity, microrotation, and concentration. It was almost unaffected, and the 2D and 3D contours obtained from these changes are also shown in **Figures 41** and **42**. The changes in the radiation

parameter did not affect the quantity of the axial velocity. The maximum positive and negative values of the axial velocity occurred for all assumed Prandtl numbers, which were 0.383953826907 and −0.383953826907, respectively. The maximum positive axial velocity occurs when the value of ξ is equal to 0.577889446943606555, and the maximum negative value of the axial velocity occurs when the value of ξ is equal to −0.577889448511109238. The lowest value of the axial velocity is calculated for all the Prandtl numbers assumed to be zero and occurs exactly at the three points of the upper disk ($\xi = 1$), the lower disk ($\xi = -1$), and between the two disks ($\xi = 0$). Changes in the Prandtl number did not affect the quantity of the radial velocity, and the maximum positive and negative values of the radial velocity for all assumed Prandtl numbers are equal to 0.986765233307 and −2, respectively. The maximum positive radial velocity occurs when the value of ξ is equal to −0.0050251257547436270 5, and the maximum negative values of the radial velocity occurs when the value of ξ is equal to ±1. The lowest value of the radial velocity, for all assumed Prandtl numbers, is zero and occurs when the value of ξ is equal to ±0.580466299484894921. Changes in the Prandtl number did not affect the quantity of microrotation, and the maximum positive and negative value of microrotation for all assumed Prandtl numbers are equal to 1.11011447812 and −1.11011447812, respectively. The maximum positive microrotation occurs when the value of ξ is equal to −0.648241207908067829, and the maximum negative value of microrotation occurs when the value of ξ is equal to 0.648241203628162621. The minimum amount of microrotation, for all the assumed Prandtl numbers, is zero and occurs exactly at three points: the upper disk ($\xi = 1$), the lower disk ($\xi = -1$), and between the two disks ($\xi = 0$). Changes in the Prandtl number did not affect the amount of concentration, and for all the Prandtl numbers, the maximum concentration was assumed to be 1. It occurred when the value of ξ was −1, and the minimum concentration was equal to zero, and for all the Prandtl numbers, it was assumed that happens when the value of ξ is equal to 1. According to **Figures 41** and **42**, changes in the Prandtl number have a significant effect only on the quantity of temperature, and when the assumed Prandtl number is equal to 22, the maximum temperature is equal to 5.29149373452, and it happened where the value of ξ is equal to −0.206030151411750184. The minimum value of temperature for all assumed Prandtl numbers occurred when the value of ξ was equal to 1 and was equal to zero.

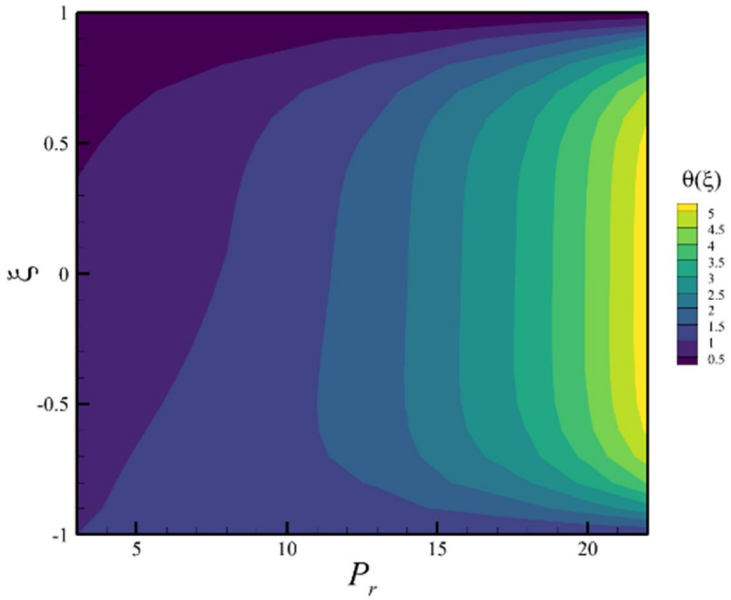

Figure 41. Two-dimensional contour of temperature at different values of the Prandtl number.

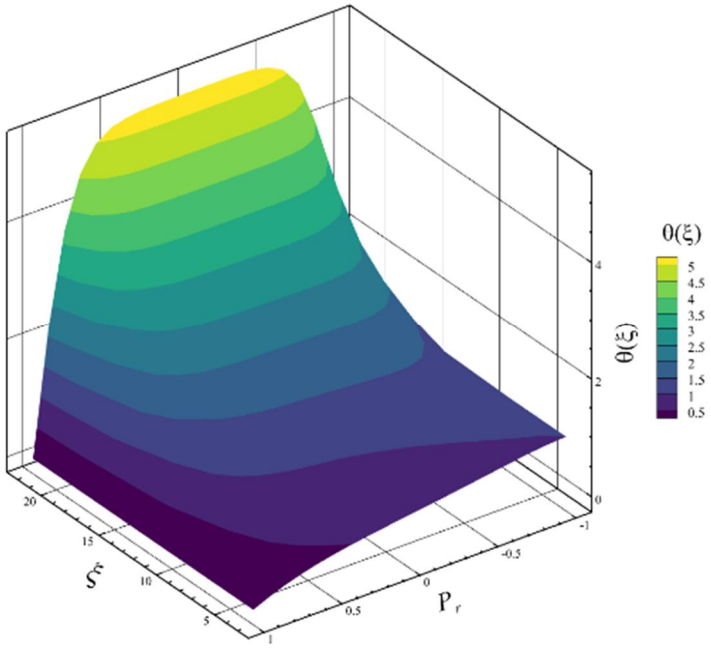

Figure 42. Three-dimensional contour of temperature at different values of the Prandtl number.

Now, the results of the investigation of axial, radial, microrotation, temperature, and concentration contours for Equations (12)–(15) when the Eckert number was changed are discussed. When the Eckert number changed, other parameters were constant and were equal to the values of $M_n = 1$, $S_c = 0.5$, $R_0 = 3$, $N_r = 1$, $P_r = 0.7$, $\lambda_3 = 0.3$, $\lambda_2 = 0.2$, $\lambda_1 = 2$. The Eckert number was investigated in 6 different cases, and the changes in this parameter had a significant effect on the quantity of temperature and the four quantities of axial velocity, radial velocity, microrotation, and concentration. It was almost unaffected, and the 2D and 3D contours obtained from these changes are also shown in **Figures 43** and **44**. The changes in Eckert

number did not affect the quantity of axial velocity. The maximum positive and negative axial velocity values occurred for all assumed Eckert numbers, equal to 0.383953826907 and −0.383953826907, respectively. The maximum positive axial velocity occurs when the value of ξ is equal to 0.577889446942673635, and the maximum negative value of the axial velocity occurs when the value of ξ is equal to −0.577889448511718862. The lowest value of the axial velocity is calculated for all Eckert numbers assumed to be zero, and exactly at the three points of the upper disk ($\xi = 1$), the lower disk ($\xi = -1$) and between the two disks ($\xi = 0$) occurs. The changes in Eckert number did not affect the quantity of radial velocity, and the maximum positive and negative value of radial velocity for all assumed Eckert numbers are equal to 0.986765233307 and −2, respectively. The maximum positive radial velocity occurs when the value of ξ is equal to −0.0050251257547436 2705, and the maximum negative value of the radial velocity occurs when the value of ξ is equal to ±1. The lowest value of the radial velocity, for all assumed Eckert numbers, is zero and occurs when the value of ξ is equal to ±0.580466299484894921. Changes in the Eckert number did not affect the amount of microrotation, and the maximum positive and negative values of the microrotation for all assumed Eckert numbers are equal to 1.11011447812 and −1.11011447812, respectively. The maximum positive microrotation occurs when the value of ξ is equal to −0.648241207908067829, and the maximum negative value of microrotation occurs when the value of ξ is equal to 0.648241203628162621. The minimum amount of microrotation, for all assumed Eckert numbers, is zero and occurs exactly at three points: the upper disk ($\xi = 1$), the lower disk ($\xi = -1$), and between two disks ($\xi = 0$). Changes in the Eckert number did not affect the amount of concentration, and the maximum concentration is equal to 1. All the assumed Eckert numbers occur when the value of ξ is equal to −1 and the minimum concentration is equal to zero, and for all the assumed Eckert numbers, they happen when the value of ξ is equal to 1. According to **Figures 43** and **44**, changes in the Eckert number have a significant effect only on the quantity of temperature, and when the assumed Eckert number is equal to 2, the maximum temperature is equal to 1.20155355593, and it happened where the value of ξ is equal to −0.648241313576453315. The minimum temperature value for all assumed Eckert numbers occurred when the value of ξ was equal to 1 and was equal to zero.

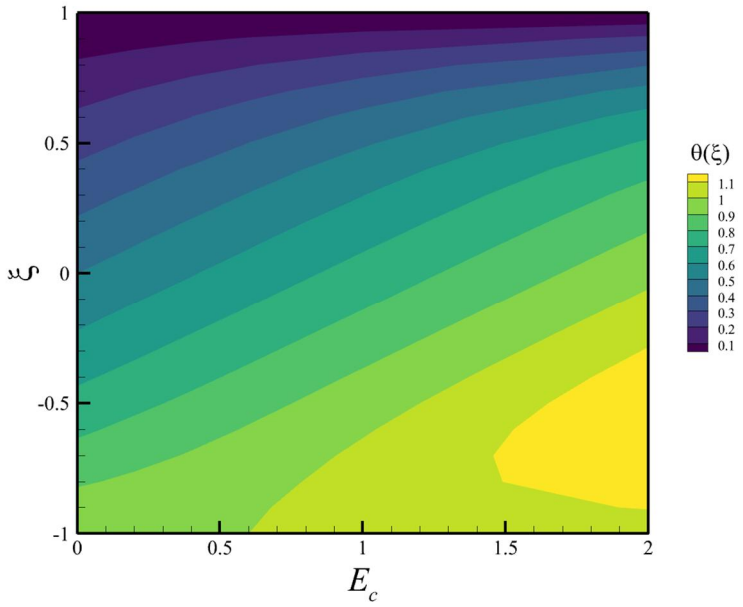

Figure 43. Two-dimensional contour of temperature at different values of the Eckert number.

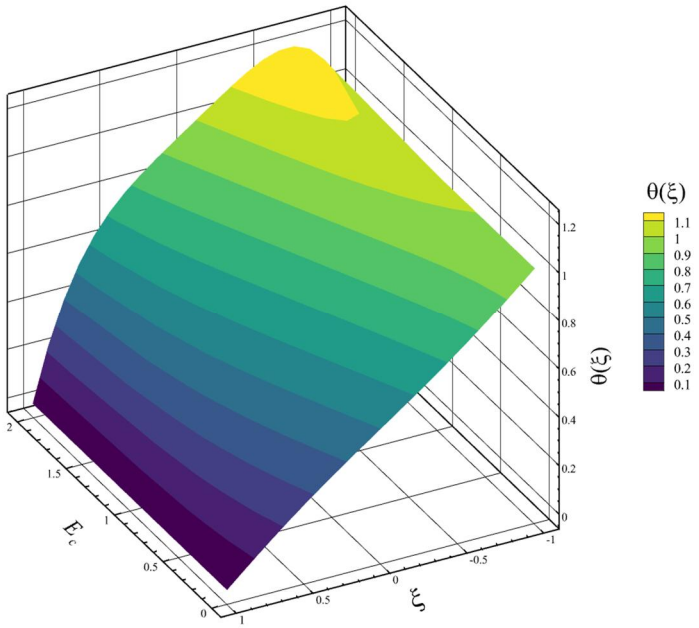

Figure 44. Three-dimensional contour of temperature at different values of the Eckert number.

Now, the results of the investigation of axial, radial, microrotation, temperature, and concentration contours for Equations (12)–(15) when the Schmidt number was changed are discussed. When the Schmidt number changed, the other parameters were constant and equal to the values of $M_n = 1$, $R_0 = 20$, $E_c = 0.2$, $N_r = 2$, $P_r = 3$, $\lambda_3 = 0.3$, $\lambda_2 = 0.2$, $\lambda_1 = 2$. The Schmidt number was investigated in 6 different cases, and the changes in this parameter had a significant effect on the quantity of concentration and the four quantities of axial velocity, radial velocity, microrotation, and temperature. It was almost unaffected, and the 2D and 3D contours obtained from these changes are also shown in **Figures 45** and **46**. Changes in the Schmidt number

did not have much effect on the quantity of the axial velocity, and the maximum positive and negative value of the axial velocity occurred for all assumed Schmidt numbers and are equal to 0.289645614908 and −0.289645614907, respectively. The maximum positive axial velocity occurs when the value of ξ is equal to 0.63819095373231749, and the maximum negative values of axial velocity occurs when the value of ξ is equal to −0.638190955068300037. The lowest value of the axial velocity is calculated for all Schmidt numbers assumed to be zero and occurs exactly at the three points of the upper disk ($\xi = 1$), the lower disk ($\xi = -1$), and between the two disks ($\xi = 0$). Changes in the Schmidt number did not affect the quantity of the radial velocity, and the maximum positive and negative values for all assumed Schmidt numbers are equal to 0.630827168825 and −2, respectively. The maximum positive radial velocity occurs when the value of ξ is equal to −0.00502512563586887499, and the maximum negative value of the radial velocity occurs when the value of ξ is equal to ±1. The lowest value of the radial velocity, for all assumed Schmidt numbers, is zero and occurs when the value of ξ is equal to ±0.640511670822128121. Changes in the Schmidt number did not affect the amount of microrotation, and the maximum positive and negative values of microrotation for all assumed Schmidt numbers are equal to 0.82620738577 and −0.826207385766, respectively. The maximum positive microrotation occurs when the value of ξ is equal to −0.748743718610704767, and the maximum negative value of microrotation occurs when the value of ξ is equal to 0.748743718014597603. The minimum amount of microrotation, for all assumed Schmidt numbers, is zero and occurs exactly at three points: the upper disk ($\xi = 1$), the lower disk ($\xi = -1$), and between the two disks ($\xi = 0$). Changes in the Schmidt number did not affect the quantity of temperature, and the maximum temperature is equal to 1 for all assumed Schmidt numbers. They occur when the value of ξ equals −1, and the minimum temperature is zero for all assumed Schmidt numbers. It happens when the value of ξ is equal to 1. According to **Figures 45** and **46**, changes in the Schmidt number only significantly affect the quantity of concentration. For all assumed Schmidt numbers, the maximum concentration is equal to 1, and for all assumed Schmidt numbers, it happens when the value of ξ is equal to −1. The minimum concentration is equal to zero. All assumed Schmidt numbers happen when the value of ξ equals 1.

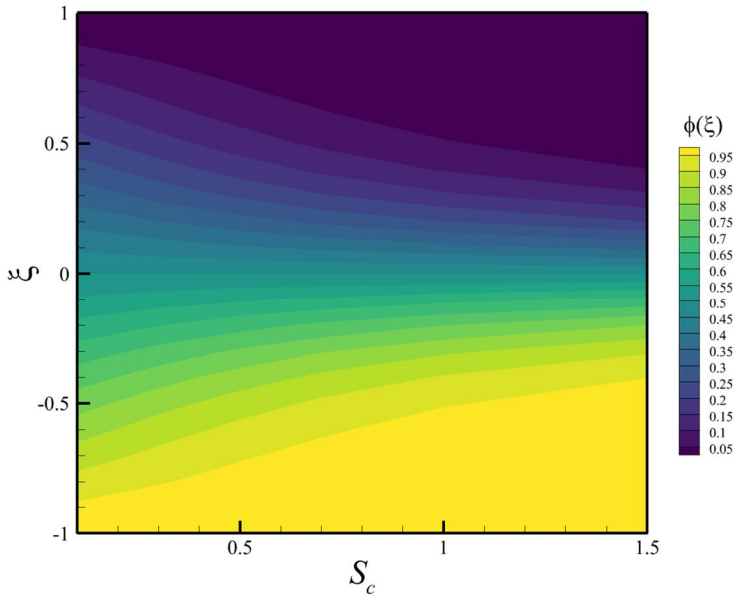

Figure 45. Two-dimensional contour of concentration at different values of the Schmidt number.

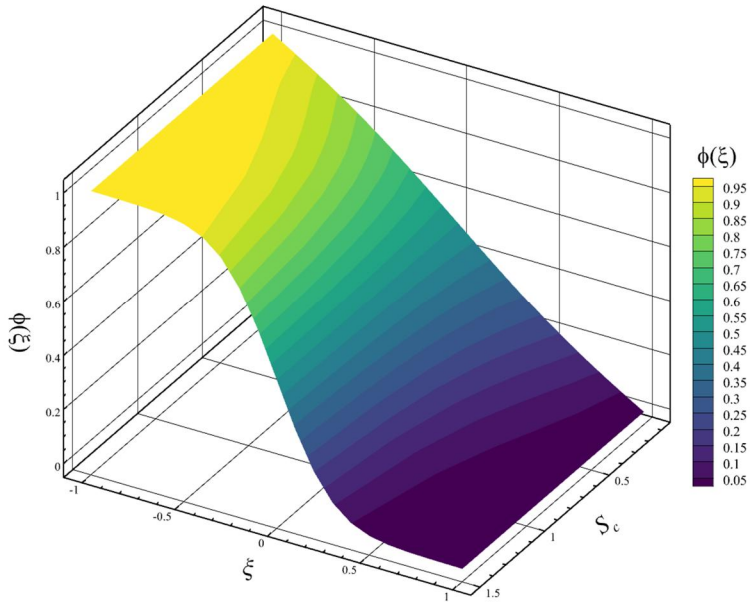

Figure 46. Three-dimensional contour of concentration at different values of the Schmidt number.

5. Conclusion

This study solved nonlinear equations governing heat and mass transfer in MHD micropolar fluid flow between stretching disks using two semi-analytical methods: the HAN method and modified AGM. These recently developed methods were applied innovatively, and their solutions were validated through three approaches: (1) substitution into governing equations with graphical verification; (2) comparison with existing analytical solutions; and (3) cross-validation between HAN and modified AGM results.

The problem addressed axisymmetric, incompressible, viscous MHD flow with

heat and mass transfer. Similarity transformations reduced the PDE system to ODEs involving four dimensionless quantities $f(\xi)$, $g(\xi)$, $\theta(\xi)$, and $\phi(\xi)$ and their derivatives with nine parameters (e.g., Reynolds number, magnetic parameter, Prandtl number). Key findings include:

- Stretching Reynolds, magnetic, and micropolar parameters significantly influenced axial/radial velocity, microrotation, temperature, and concentration.
- Prandtl number ($3 \leq P_r \leq 22$) caused a 429% change in maximum temperature but did not affect other quantities.
- Eckert number ($E_c = 1 \rightarrow 2$) led to a 16.5% increase in maximum temperature, with negligible impact elsewhere.
- Schmidt number ($0.1 \leq S_c \leq 1.5$) altered only concentration profile shape, not extrema.
- Radiation parameter ($0 \leq N_r \leq 8$) modified temperature graph shape without changing its maxima/minima.

The HAN method's ability to derive analytical expressions from numerical data and the modified AGM's independence from numerical solutions offer advantages over traditional techniques. Future work could extend this framework to analyze skin friction, Nusselt number, or microorganism density, broadening the physical insights.

Conflict of interest: The author declares no conflict of interest.

Nomenclature

Circular cylindrical coordinate system (m, rad, m)	r, θ, z	Components of the unit vector (-)	$\hat{\mathbf{e}}_1, \hat{\mathbf{e}}_2, \hat{\mathbf{e}}_3$
Velocity components (m/s)	u, w	Stefan-Boltzmann constant ($\mathrm{W/m^2.K^4}$)	σ
Time (s)	t	Average absorption coefficient ($\mathrm{cm^{-1}}$)	k_a
Distance from r- axis (m)	l	Reactive flow ($\mathrm{kg/s^2.m^3}$)	$\dot{m}'''$
Velocity vector field (m/s)	$\mathbf{V}$	Stretching parameter of the disks ($\mathrm{s^{-1}}$)	S
Pressure field (Pa)	p	Dimensionless temperature (-)	$\theta(\xi)$
Dynamic viscosity (kg/m. s)	μ	Dimensionless concentration (-)	$\phi(\xi)$
Vortex viscosity	κ	Dimensionless axial velocity (-)	$f(\xi)$
Micro-inertia per unit mass	j	Dimensionless radial velocity (-)	$f'(\xi)$
Microrotation vector field (m/s)	$\mathbf{N}$	Dimensionless micro-rotation velocity (-)	$g(\xi)$
Components of the microrotation (m/s)	N_1, N_2, N_3	Stretching Reynolds number (-)	R_0
Fluid density ($\mathrm{kg/m^3}$)	ρ	Magnetic parameter (-)	M_n
Density vector field ($\mathrm{kg/m^3}$)	$\mathbf{J}$	Vortex viscosity (-)	λ_1
Sum of induced and imposed magnetic field	$\mathbf{B}$	Micro-inertial density (-)	λ_2
Gyro-viscosity coefficients	$\alpha_1, \alpha_2, \alpha_3$	Spin gradient viscosity parameter (-)	λ_3
Gradient operator (-)	$\boldsymbol{\nabla}$	Prandtl number (-)	P_r
Curl operator (-)	$\boldsymbol{\nabla}\times$	Radiation parameter	N_r
Temperature scalar field (K)	T	Eckert number (-)	E_c
Electrical conductivity of the fluid (S/m)	σ_el	Schmidt number (-)	Sc
Temperature of the lower disk (K)	T_1	Radius of the disk (m)	r
Temperature of the upper disk (K)	T_2	local Reynolds number (-)	R_e
Concentration scalar field ($\mathrm{mol/m^3}$)	C	Nusselt number (-)	N_u

Concentration of the lower disk ($\mathrm{mol/m^3}$)	C_1	Skin friction coefficient (-)	C_f
Concentration of the upper disk ($\mathrm{mol/m^3}$)	C_2	Wall couple stress (-)	C_g
Similarity variable (-)	ξ	Viscous dissipation function ($\mathrm{W/s.kg^{-1} \cdot m^{-2}}$)	Φ
Specific heat capacity at constant pressure ($\mathrm{J/kg \cdot K}$)	c_p	Thermal conductivity coefficient ($\mathrm{W/m \cdot K}$)	k
Radiant heat flux ($\mathrm{J/s}$)	q_rh	Diffusion coefficient/mass diffusivity ($\mathrm{m^2/s}$)	D_e
Strength of the magnetic field ($\mathrm{A/m}$)	B_os		

References

1. Agarwal R. Heat and mass transfer in electrically conducting micropolar fluid flow between two stretchable disks. Materials Today: Proceedings. 2021; 46: 10227-10238. doi: 10.1016/j.matpr.2020.11.614
2. Jalili P, Ahmadi Azar A, Jalili B, et al. Heat transfer analysis in cylindrical polar system with magnetic field: A novel Hybrid Analytical and Numerical Technique. Case Studies in Thermal Engineering. 2022; 40: 102524. doi: 10.1016/j.csite.2022.102524
3. Eringen AC. Simple microfluids. International Journal of Engineering Science. 1964; 2(2): 205-217. doi: 10.1016/0020-7225(64)90005-9
4. Eringen AC. Theory of Micropolar Fluids. Indiana University Mathematics Journal. 1966; 16(1): 1-18. doi: 10.1512/iumj.1967.16.16001
5. Eringen AC. Microcontinuum Field Theories: I. Foundations and Solids. Springer New York; 2012.
6. Lukaszewicz G. Micropolar Fluids: Theory and Applications. Birkhäuser Boston; 2012.
7. Turkyilmazoglu M. Analytic approximate solutions of rotating disk boundary layer flow subject to a uniform suction or injection. International Journal of Mechanical Sciences. 2010; 52(12): 1735-1744. doi: 10.1016/j.ijmecsci.2010.09.007
8. Turkyilmazoglu M. Purely analytic solutions of magnetohydrodynamic swirling boundary layer flow over a porous rotating disk. Computers & Fluids. 2010; 39(5): 793-799. doi: 10.1016/j.compfluid.2009.12.007
9. Turkyilmazoglu M. Analytic approximate solutions of rotating disk boundary layer flow subject to a uniform vertical magnetic field. Acta Mechanica. 2010; 218(3-4): 237-245. doi: 10.1007/s00707-010-0416-4
10. Sahoo B, Van Gorder RA, Andersson HI. Steady revolving flow and heat transfer of a non-Newtonian Reiner–Rivlin fluid. International Communications in Heat and Mass Transfer. 2012; 39(3): 336-342. doi: 10.1016/j.icheatmasstransfer.2011.12.007
11. Srivastava N. MHD Flow of the Micropolar Fluid between Eccentrically Rotating Disks. International Scholarly Research Notices. 2014; 2014: 1-7. doi: 10.1155/2014/317075
12. Iqbal MF, Ali K, Ashraf M. Heat and mass transfer analysis in unsteady titanium dioxide nanofluid between two orthogonally moving porous coaxial disks: a numerical study. Canadian Journal of Physics. 2015; 93(3): 290-299. doi: 10.1139/cjp-2014-0243
13. Kocic M, Stamenkovic Z, Petrovic J, et al. Heat transfer in micropolar fluid flow under the influence of magnetic field. Thermal Science. 2016; 20(suppl. 5): 1391-1404. doi: 10.2298/tsci16s5391k
14. Turkyilmazoglu M. Flow and heat simultaneously induced by two stretchable rotating disks. Physics of Fluids. 2016; 28(4). doi: 10.1063/1.4945651
15. Akhter S, Ashraf M, Ali K. MHD flow and heat transfer analysis of micropolar fluid through a porous medium between two stretchable disks using quasi-linearization method. Iran. J. Chem. Chem. Eng. 2017; 36(4).
16. Doh DH, Muthtamilselvan M. Thermophoretic particle deposition on magnetohydrodynamic flow of micropolar fluid due to a rotating disk. International Journal of Mechanical Sciences. 2017; 130: 350-359. doi: 10.1016/j.ijmecsci.2017.06.029
17. Hayat T, Javed M, Imtiaz M, et al. Convective flow of Jeffrey nanofluid due to two stretchable rotating disks. Journal of Molecular Liquids. 2017; 240: 291-302. doi: 10.1016/j.molliq.2017.05.024
18. Das A, Sahoo B. Flow of a Reiner-Rivlin fluid between two infinite coaxial rotating disks. Mathematical Methods in the Applied Sciences. 2018; 41(14): 5602-5618. doi: 10.1002/mma.5103
19. Tabassum M, Mustafa M. A numerical treatment for partial slip flow and heat transfer of non-Newtonian Reiner-Rivlin fluid due to rotating disk. International Journal of Heat and Mass Transfer. 2018; 123: 979-987. doi: 10.1016/j.ijheatmasstransfer.2018.03.040

20. Yao B, Lian L. A new analysis of the rotationally symmetric flow in the presence of an infinite rotating disk. International Journal of Mechanical Sciences. 2018; 136: 106-111. doi: 10.1016/j.ijmecsci.2017.12.023
21. Sahoo B, Shevchuk IV. Heat transfer due to revolving flow of Reiner-Rivlin fluid over a stretchable surface. Thermal Science and Engineering Progress. 2019; 10: 327-336. doi: 10.1016/j.tsep.2019.03.004
22. Yao B, Lian L. Series solution of the rotationally symmetric flow in the presence of an infinite rotating disk with uniform suction. European Journal of Mechanics - B/Fluids. 2019; 74: 159-166. doi: 10.1016/j.euromechflu.2018.11.012
23. Zangooee MR, Hosseinzadeh Kh, Ganji DD. Hydrothermal analysis of MHD nanofluid (TiO2-GO) flow between two radiative stretchable rotating disks using AGM. Case Studies in Thermal Engineering. 2019; 14: 100460. doi: 10.1016/j.csite.2019.100460
24. Das A, Sarkar S Flow analysis of Reiner-Rivlin fluid between two stretchable rotating disks. In: Recent Trends in Wave Mechanics and Vibrations: Select Proceedings of WMVC 2018 Springer Singapore; 2020. pp. 61-70. doi: 10.1007/978-981-15-0287-3_5
25. Naqvi SMRS, Kim HM, Muhammad T, et al. Numerical study for slip flow of Reiner-Rivlin nanofluid due to a rotating disk. International Communications in Heat and Mass Transfer. 2020; 116: 104643. doi: 10.1016/j.icheatmasstransfer.2020.104643
26. Usman M, Mehmood A, Weigand B. Heat transfer from a non-isothermal rotating rough disk subjected to forced flow. International Communications in Heat and Mass Transfer. 2020; 110: 104395. doi: 10.1016/j.icheatmasstransfer.2019.104395
27. Faraz N, Khan Y. Analytical solution of electrically conducted rotating flow of a second grade fluid over a shrinking surface. Ain Shams Engineering Journal. 2011; 2(3-4): 221-226. doi: 10.1016/j.asej.2011.10.001
28. Zhang X, Li M. Analysis of a semi-implicit and structure-preserving finite element method for the incompressible MHD equations with magnetic-current formulation. Communications in Nonlinear Science and Numerical Simulation. 2024; 128: 107677. doi: 10.1016/j.cnsns.2023.107677
29. Jalaal M, Nejad MG, Jalili P, et al. Homotopy perturbation method for motion of a spherical solid particle in plane couette fluid flow. Computers & Mathematics with Applications. 2011; 61(8): 2267-2270. doi: 10.1016/j.camwa.2010.09.042
30. Abdelmoneim M, Eldabe NT, Abouzeid MY, et al. Modified Darcy's law and couple stress effects on electro-osmotic flow of non-Newtonian nanofluid with peristalsis. International Journal of Applied Electromagnetics and Mechanics. 2023; 72(3): 253-277. doi: 10.3233/jae-220287
31. Hamad MAA. Analytical solution of natural convection flow of a nanofluid over a linearly stretching sheet in the presence of magnetic field. International Communications in Heat and Mass Transfer. 2011; 38(4): 487-492. doi: 10.1016/j.icheatmasstransfer.2010.12.042
32. Bejan A. A synthesis of analytical results for natural convection heat transfer across rectangular enclosures. International Journal of Heat and Mass Transfer. 1980; 23(5): 723-726. doi: 10.1016/0017-9310(80)90017-4
33. Ndlovu PL, Moitsheki RJ. Analytical Solutions for Steady Heat Transfer in Longitudinal Fins with Temperature-Dependent Properties. Mathematical Problems in Engineering. 2013; 2013: 1-14. doi: 10.1155/2013/273052
34. Mabood F, Khan WA, Ismail AIMd. MHD flow over exponential radiating stretching sheet using homotopy analysis method. Journal of King Saud University - Engineering Sciences. 2017; 29(1): 68-74. doi: 10.1016/j.jksues.2014.06.001
35. Talarposhti RA, Jalili P, Rezazadeh H, et al. Optical soliton solutions to the (2+1)-dimensional Kundu–Mukherjee–Naskar equation. International Journal of Modern Physics B. 2020; 34(11): 2050102. doi: 10.1142/s0217979220501027
36. Jalili B, Jalili P, Sadighi S, et al. Effect of magnetic and boundary parameters on flow characteristics analysis of micropolar ferrofluid through the shrinking sheet with effective thermal conductivity. Chinese Journal of Physics. 2021; 71: 136-150. doi: 10.1016/j.cjph.2020.02.034
37. Mahabaleshwar US, Maranna T, Pérez LM, et al. An effect of magnetohydrodynamic and radiation on axisymmetric flow of non-Newtonian fluid past a porous shrinking/stretching surface. Journal of Magnetism and Magnetic Materials. 2023; 571: 170538. doi: 10.1016/j.jmmm.2023.170538
38. Khan Y. A series solution of the boundary value problem arising in the application of fluid mechanics. International Journal of Numerical Methods for Heat & Fluid Flow. 2018; 28(10): 2480-2490. doi: 10.1108/hff-11-2017-0474
39. Ahmad A, Ishaq A, Khan Y. Influence of FENE-P fluid on drag reduction and heat transfer past a magnetized surface. International Journal of Modern Physics B. 2022; 36(23). doi: 10.1142/s0217979222501454
40. Khan Y, Majeed AH, Rasheed MA, et al. Dual solutions for double diffusion and MHD flow analysis of micropolar

nanofluids with slip boundary condition. Frontiers in Physics. 2022; 10. doi: 10.3389/fphy.2022.956737

41. Khan Y. Magnetohydrodynamic flow of linear visco-elastic fluid model above a shrinking/stretching sheet: A series solution. Scientia Iranica. 2017. doi: 10.24200/sci.2017.4305
42. Anusha T, Mahabaleshwar US, Hatami M. Navier slip effect on the thermal-flow of Walters' liquid B flow due to porous stretching/shrinking with heat and mass transfer. Case Studies in Thermal Engineering. 2021; 28: 101691. doi: 10.1016/j.csite.2021.101691
43. Ghadikolaei SS, Hosseinzadeh KH, Hatami M, et al. Investigation for squeezing flow of ethylene glycol (C2H6O2) carbon nanotubes (CNTs) in rotating stretching channel with nonlinear thermal radiation. Journal of Molecular Liquids. 2018; 263: 10-21. doi: 10.1016/j.molliq.2018.04.141
44. Ghasemi SE, Hatami M, Sarokolaie AK, et al. Study on blood flow containing nanoparticles through porous arteries in presence of magnetic field using analytical methods. Physica E: Low-dimensional Systems and Nanostructures. 2015; 70: 146-156. doi: 10.1016/j.physe.2015.03.002
45. Fakour M, Vahabzadeh A, Ganji DD, et al. Analytical study of micropolar fluid flow and heat transfer in a channel with permeable walls. Journal of Molecular Liquids. 2015; 204: 198-204. doi: 10.1016/j.molliq.2015.01.040
46. Rashad A, Nafe M, Eisa D. 2D Radiative Casson-Carreau Hybrid Nanofluid Flow through a Circular Cylinder in a Darcy-Forchheimer Porous Medium. New Valley University Journal of Basic and Applied Sciences. 2023; 1(1): 1-19. doi: 10.21608/nujbas.2023.218751.1012
47. Rashad AM, Nafe MA, Eisa DA. Yield Stress Impact on Magnetohydrodynamic Jeffery Hybrid Nanofluid Flow Over a Moving Porous Surface: Buongiorno's Model. Journal of Nanofluids. 2023; 12(7): 1729-1738. doi: 10.1166/jon.2023.2057
48. Abdelhafez MA, Awad AA, Nafe MA, et al. Time-dependent viscous flow of higher-order reactive MHD Maxwell nanofluid with Joule heating in a porous regime. Waves in Random and Complex Media. 2021; 34(3): 1041-1061. doi: 10.1080/17455030.2021.1927237
49. Turkyilmazoglu M. Evidence of stretching/moving sheet-triggered nonlinear similarity flows: atomization and electrospinning with/without air resistance. International Journal of Numerical Methods for Heat & Fluid Flow. 2024; 34(9): 3598-3614. doi: 10.1108/hff-04-2024-0254
50. Turkyilmazoglu M. Two Models on the Unsteady Heat and Fluid Flow Induced by Stretching or Shrinking Sheets and Novel Time-Dependent Solutions. ASME Journal of Heat and Mass Transfer. 2024; 146(10). doi: 10.1115/1.4065674
51. Enamul, S. and Ontela, S., 2025. Entropy Analysis of Hall-Effect-Driven Ti− CoFe2O4/Engine Oil-Based Hybrid Nanofluid Flow Between Spinning Porous Disks with Thermal Convective Boundaries. JCIS Open, p.100134. https://doi.org/10.1016/j.jciso.2025.100134
52. Hussain, M., Shahid, S., Akbar, N.S. and Alaoui, M.K., 2025. Unsteady Flow and Heat Transfer Optimization of Viscous Fluid with Bioconvection over a Rotating Stretchable Disk and Gyrotactic Motile Microorganisms. Case Studies in Thermal Engineering, p.105796. https://doi.org/10.1016/j.csite.2025.105796
53. Lone, S.A., Bossly, R., Alduais, F.S., Al-Bossly, A., Khan, A. and Saeed, A., 2025. Thermal investigation of magnetized Casson hybrid nanofluid flow through two stretchable angular rotating disks with variable porosity and Cattaneo-Christov heat flux model: a numerical approach. Colloid and Polymer Science, 303(3), pp.529-546. https://doi.org/10.1007/s00396-024-05363-7
54. Mandal, S., Mukherjee, S., Shit, G.C. and Vajravelu, K., 2025. Entropy analysis of MHD flow in hybrid nanofluid over a rotating disk with variable viscosity and nonlinear thermal radiation. ZAMM‐Journal of Applied Mathematics and Mechanics/Zeitschrift für Angewandte Mathematik und Mechanik, 105(2), p.e202301027. https://doi.org/10.1002/zamm.202301027
55. Naveed Khan, M., Ahmad, S., Ahammad, N.A., Alqahtani, T. and Algarni, S., 2025. Numerical investigation of hybrid nanofluid with gyrotactic microorganism and multiple slip conditions through a porous rotating disk. Waves in Random and Complex Media, 35(2), pp.3789-3804. https://doi.org/10.1080/17455030.2022.2055205
56. Rauf, A., Ramesh, G.K., Fatima, S., Shehzad, S.A., Madhukesh, J.K. and Siddiq, M.K., 2025. Horizontal Magnetic Field Influence on Fluid Flow Across a Variable Thickness Rotating Disk With Stretching and Melting Phenomenon. Heat Transfer. https://doi.org/10.1002/htj.23285
57. Senbagaraja, P. and De, P., 2025. Sensitivity analysis on electro-osmotic flow of EMHD tangent hyperbolic nanofluid through porous rotating disk with variable thermal conductivity, Stefan blowing and thermal radiation. Multiscale and Multidisciplinary Modeling, Experiments and Design, 8(1), p.65. https://doi.org/10.1007/s41939-024-00648-4

58. Sultana, U., Mushtaq, M., Ahmad, I. and Muhammad, T., 2025. Porosity and heat transfer analysis of nanofluids due to rotating-stretching disk with Joule heating. Modern Physics Letters B, 39(01), p.2450404. https://doi.org/10.1142/S0217984924504049
59. Turkyilmazoglu, M. and Pop, I., 2025. Rheology of Bingham viscoplastic flow triggered by a rotating and radially stretching disk. International Journal of Numerical Methods for Heat & Fluid Flow. https://doi.org/10.1108/HFF-11-2024-0845
60. Usman, Kumar, R.V., Khan, W.A., AL‐lobani, E.M. and Massoud, E.E.S., 2025. Mathematical modeling and numerical simulations of convective heat transport in a stagnant flow of water‐based copper, aluminum oxide and MWCNTs nanofluid upon a stretching spinning disk. ZAMM‐Journal of Applied Mathematics and Mechanics/Zeitschrift für Angewandte Mathematik und Mechanik, 105(1), p.e202400476. https://doi.org/10.1002/zamm.202400476
61. Zada, J., Khan, A., Farooq, M., Alsubaie, A.S., Rezapour, S. and Inc, M., 2025. Computation of stretching disks fluid flow of hybrid nanofluid under the effect of variable magnetic field. ZAMM‐Journal of Applied Mathematics and Mechanics/Zeitschrift für Angewandte Mathematik und Mechanik, 105(1), p.e202400114. https://doi.org/10.1002/zamm.202400114
62. Azar, A.A., 2025. Semi-analytical solution for nonlinear Von Kármán swirling fluid flow via the hybrid analytical and numerical method. Mechanical Engineering Advances, 3(2), pp.2878-2878. https://doi.org/10.59400/mea2878
63. Jalili P, Azar AA, Jalili B, et al. The HAN method for a thermal analysis of forced non-Newtonian MHD Reiner-Rivlin viscoelastic fluid motion between two disks. Heliyon. 2023; 9(6): e17535. doi: 10.1016/jheliyon2023.e17535
64. Jalili B, Ahmadi Azar A, Esmaeili K, et al. A novel approach to micropolar fluid flow between a non-porous disk and a porous disk with slip. Chinese Journal of Physics. 2024; 87: 118-137. doi: 10.1016/j.cjph.2023.11.023
65. Ahmadi Azar A, Jalili B, Jalili P, et al. Investigating the effect of structural changes of two stretching disks on the dynamics of the MHD model. Scientific Reports. 2023; 13(1). doi: 10.1038/s41598-023-48988-4
66. Jalili P, Azar AA, Jalili B, et al. A Novel Analytical Investigation of a Swirling Fluid Flow and a Rotating Disk in the Presence of Uniform Suction. Arabian Journal for Science and Engineering. 2023; 49(8): 10453-10469. doi: 10.1007/s13369-023-08391-7
67. Jalili P, Azar AA, Jalili B, et al. Study of nonlinear radiative heat transfer with magnetic field for non-Newtonian Casson fluid flow in a porous medium. Results in Physics. 2023; 48: 106371. doi: 10.1016/j.rinp.2023.106371
68. Jalili B, Azar AA, Jalili P, et al. Analytical approach for micropolar fluid flow in a channel with porous walls. Alexandria Engineering Journal. 2023; 79: 196-226. doi: 10.1016/j.aej.2023.08.015
69. Jalili B, Ahmadi Azar A, Jalili P, et al. Investigation of the unsteady MHD fluid flow and heat transfer through the porous medium asymmetric wavy channel. Case Studies in Thermal Engineering. 2024; 61: 104859. doi: 10.1016/j.csite.2024.104859
70. Jalili P, Ahmadi Azar A, Jalili B, et al. A novel technique for solving unsteady three-dimensional brownian motion of a thin film nanofluid flow over a rotating surface. Scientific Reports. 2023; 13(1). doi: 10.1038/s41598-023-40410-3
71. Azar EA, Jalili B, Azar AA, et al. An exact analytical solution of the Emden–Chandrasekhar equation for self-gravitating isothermal gas spheres in the theory of stellar structures. Physics of the Dark Universe. 2023; 42: 101309. doi: 10.1016/j.dark.2023.101309
72. Jalili B, Azar AA, Liu D, et al. Analytical formulation of the steady-state planar Taylor–Couette flow constitutive equations with entropy considerations. Physics of Fluids. 2024; 36(11). doi: 10.1063/5.0239765
73. Khan KA, Vivas-Cortez M, Ishfaq K, et al. Exploring the numerical simulation of Maxwell nanofluid flow over a stretching sheet with the influence of chemical reactions and thermal radiation. Results in Physics. 2024; 60: 107635. doi: 10.1016/j.rinp.2024.107635
74. Basit MA, Imran M, Akgül A, et al. Mathematical analysis of heat and mass transfer efficiency of bioconvective Casson nanofluid flow through conical gap among the rotating surfaces under the influences of thermal radiation and activation energy. Results in Physics. 2024; 63: 107863. doi: 10.1016/j.rinp.2024.107863
75. Alzabut J, Nadeem S, Noor S, et al. Numerical analysis of Magnetohydrodynamic convection heat flow in an enclosure. Results in Physics. 2023; 51: 106618. doi: 10.1016/j.rinp.2023.106618
76. Gamachu D, Ibrahim W, Bijiga LK. Nonlinear convection unsteady flow of electro-magnetohydrodynamic Sutterby hybrid nanofluid in the stagnation zone of a spinning sphere. Results in Physics. 2023; 49: 106498. doi: 10.1016/j.rinp.2023.106498
77. Tshivhi KS, Tshehla MS. Heat source and radiation effects on MHD flow of Copper-Water nanofluid over exponential stretching surface with slip. Results in Physics. 2024; 58: 107463. doi: 10.1016/j.rinp.2024.107463

78. Leng Y, Li Y, Anwaar H, et al. Unraveling metachronal wave effects on heat and mass transfer in Non-Newtonian fluid. Case Studies in Thermal Engineering. 2024; 58: 104379. doi: 10.1016/j.csite.2024.104379
79. McChesney M. A Textbook of Magnetohydrodynamics. J. A. Shercliff. Pergamon Press, Oxford. 1965. 265 pp. Diagrams. 21s. The Journal of the Royal Aeronautical Society. 1966; 70(663): 453-453. doi: 10.1017/s0001924000058607
80. Devi SPAA, Devi RUU. On hydromagnetic flow due to a rotating disk with radiation effects. Nonlinear Analysis: Modelling and Control. 2011; 16(1): 17-29. doi: 10.15388/na.16.1.14112
81. Pattnaik PK, Panda S, Baithalu R, et al. Darcy-Forchheimer inertial drag on micropolar hybrid nanofluid flow through a channel: Akbari-Ganji method. Chaos, Solitons & Fractals. 2025; 194: 116197. doi: 10.1016/j.chaos.2025.116197
82. Mirgolbabaee H, Ledari ST, Ganji DD. Semi-analytical investigation on micropolar fluid flow and heat transfer in a permeable channel using AGM. Journal of the Association of Arab Universities for Basic and Applied Sciences. 2017; 24(1): 213-222. doi: 10.1016/j.jaubas.2017.01.002